GDAŃSK UNIVERSITY OF TECHNOLOGY

GDAŃSK UNIVERSITY OF TECHNOLOGY
FACULTY OF OCEAN ENGINEERING AND SHIP TECHNOLOGY

Polish Maritime Research

No. 4 (88) 2015
Vol. 22

CONTENS

ADDRESS OF PUBLISHER & EDITOR'S OFFICE:

GDAŃSK UNIVERSITY OF TECHNOLOGY

Faculty of Ocean Engineering & Ship Technology
G. Narutowicza 11/12
80-233 Gdańsk, POLAND

tel.: +48 58 347 13 66
fax: +48 58 341 13 66

EDITORIAL STAFF:

Jacek Rudnicki
| Editor in Chief
Przemysław Wierzchowski
| Associate Editor
Rafał Szłapczyński
| Associate Editor
Aleksander Kniat
| Editor for international relations
Kazimierz Kempa
| Technical Editor

Price:
single issue: 25 zł

Prices for abroad
single ussue:
- in Europe EURO 15
- overseas USD 20

WEB:
www.bg.pg.gda.pl/pmr/pmr.php

ISSN 1233-2585

3 **Aleksander Nowak**
THE PROPOSAL TO "SNAPSHOT" RAIM METHOD FOR GNSS VESSEL RECEIVERS WORKING IN POOR SPACE SEGMENT GEOMETRY

9 **Paweł Burdziakowski, Artur Janowski, Arthem Kholodkov, Krzysztof Matysik, Maciej Matysik, Marek Przyborski, Jakub Szulwic, Paweł Tysiąc, Aleksander Wojtowicz**
MARITIME LASER SCANNING AS THE SOURCE FOR SPATIAL DATA

15 **K. Drypczewski, M. Moszyński, J. Demkowicz, K. Bikonis, A. Stepnowski**
DESIGN OF THE DUAL CONSTELLATION GPS/GALILEO MOBILE DEVICE FOR IMPROVING NAVIGATION OF THE VISUALLY IMPAIRED IN AN URBAN AREA

21 **K. Drypczewski, A. Stepnowski, K. Bruniecki**
METHOD TO EXTEND OPERATIONABILITY OF WEB-GIS BASED MARINE SERVICES USING SSE PLATFORM

27 **Józef Lisowski**
SENSITIVITY OF THE GAME CONTROL OF SHIP IN COLLISION SITUATIONS

34 **Agnieszka Lazarowska**
SWARM INTELLIGENCE APPROACH TO SAFE SHIP CONTROL

41 **Marian Cichy, Jacek Kropiwnicki, Zbigniew Kneba**
A MODEL OF THERMAL ENERGY STORAGE ACCORDING TO THE CONVENTION OF BOND GRAPHS (BG) AND STATE EQUATIONS (SE)

48 **Lamas, M.I., Rodríguez, C.G., Telmo, J. Rodríguez**
NUMERICAL ANALYSIS OF EMISSIONS FROM MARINE ENGINES USING ALTERNATIVE FUELS

53 **Zygfryd Domachowski, Marek Dzida**
INLET AIR FOGGING OF MARINE GAS TURBINE IN POWER OUTPUT LOSS COMPENSATION

59 **Janusz Kozak, Jakub Kowalski**
THE INFLUENCE OF MANUFACTURING OVERSIZING ON POST-WELDING DISTORTIONS OF THE FILLET WELDED JOINT

64 **Adam Lipski**
THERMOGRAPHIC METHOD BASED ACCELERATED FATIGUE LIMIT CALCULATION FOR STEEL X5CRNI18-10 SUBJECTED TO ROTATING BENDING

70 **Qingwei Ye, Zhimin Feng, Debin Yuan**
NONLINEAR VIBRATION SIGNAL TRACKING OF LARGE OFFSHORE BRIDGE STAYED CABLE BASED ON PARTICLE FILTER

76 **Gang Luo, Jianxun Chen, Xiaojun Zhou**
EFFECTS OF VARIOUS FACTORS ON THE VIV-INDUCED FATIGUE DAMAGE IN THE CABLE OF SUBMERGED FLOATING TUNNEL

84 **Mariusz Żółtowski, Michał Liss, Bogdan Żółtowski, Josef Melcer**
TRUSS HARBOR CRANES MODAL DESIGN ELEMENTS RESEARCH

Editorial

POLISH MARITIME RESEARCH is a scientific journal of worldwide circulation. The journal appears as a quarterly four times a year. The first issue of it was published in September 1994. Its main aim is to present original, innovative scientific ideas and Research & Development achievements in the field of **:**

Engineering, Computing & Technology, Mechanical Engineering,

which could find applications in the broad domain of maritime economy. Hence there are published papers which concern methods of the designing, manufacturing and operating processes of such technical objects and devices as : ships, port equipment, ocean engineering units, underwater vehicles and equipment as well as harbour facilities, with accounting for marine environment protection.
The Editors of POLISH MARITIME RESEARCH make also efforts to present problems dealing with education of engineers and scientific and teaching personnel. As a rule, the basic papers are supplemented by information on conferences , important scientific events as well as cooperation in carrying out international scientific research projects.

Scientific Board

Chairman : Prof. JERZY GIRTLER - Gdańsk University of Technology, Poland
Vice-chairman : Prof. MIROSŁAW L. WYSZYŃSKI - University of Birmingham, United Kingdom

Dr POUL ANDERSEN
Technical University of Denmark
Denmark

Dr MEHMET ATLAR
University of Newcastle United Kingdom

Prof. GÖRAN BARK
Chalmers University of Technology
Sweden

Prof. SERGEY BARSUKOV
Army Institute of Odessa Ukraine

Prof. MUSTAFA BAYHAN
Süleyman Demirel University
Turkey

Prof. VINCENZO CRUPI
University of Messina, Italy

Prof. MAREK DZIDA
Gdańsk University of Technology
Poland

Prof. ODD M. FALTINSEN
Norwegian University of Science and Technology
Norway

Prof. PATRICK V. FARRELL
University of Wisconsin Madison, WI
USA

Prof. WOLFGANG FRICKE
Technical University Hamburg-Harburg Germany

Prof. HASSAN GHASSEMI
Amirkabir University of Technology
Iran

Prof. STANISŁAW GUCMA
Maritime University of Szczecin
Poland

Prof. ANTONI ISKRA
Poznań University of Technology
Poland

Prof. JAN KICIŃSKI
Institute of Fluid-Flow Machinery of PASci
Poland

Prof. ZBIGNIEW KORCZEWSKI
Gdańsk University of Technology
Poland

Prof. JANUSZ KOZAK
Gdańsk University of Technology
Poland

Prof. JAN KULCZYK
Wrocław University of Technology
Poland

Prof. NICOS LADOMMATOS
University College London United Kingdom

Prof. JÓZEF LISOWSKI
Gdynia Maritime University Poland

Prof. JERZY MATUSIAK
Helsinki University of Technology
Finland

Prof. EUGEN NEGRUS
University of Bucharest Romania

Prof. YASUHIKO OHTA
Nagoya Institute of Technology
Japan

Dr YOSHIO SATO
National Traffic Safety and Environment Laboratory
Japan

Prof. KLAUS SCHIER
University of Applied Sciences
Germany

Prof. FREDERICK STERN
University of Iowa, IA, USA

Prof. ILCEV DIMOV STOJCE
Durban University of Technology
South Africa

Prof. JÓZEF SZALA
Bydgoszcz University of Technology and Agriculture
Poland

Prof. WITALIJ SZCZAGIN
State Technical University of Kaliningrad, Russia

Prof. BORIS TIKHOMIROV
State Marine University of St. Petersburg, Russia

Prof. DRACOS VASSALOS
University of Glasgow and Strathclyde United Kingdom

POLISH MARITIME RESEARCH 4(88) 2015 Vol. 22; pp. 3-8
10.1515/pomr-2015-0063

THE PROPOSAL TO "SNAPSHOT" RAIM METHOD FOR GNSS VESSEL RECEIVERS WORKING IN POOR SPACE SEGMENT GEOMETRY

Aleksander Nowak , Ph. D.
Gdańsk Univeristy of Technology, Poland

ABSTRACT

Nowadays, we can observe an increase in research on the use of small unmanned autonomous vessel (SUAV) to patrol and guiding critical areas including harbours. The proposal to "snapshot" RAIM (Receiver Autonomous Integrity Monitoring) method for GNSS receivers mounted on SUAV operating in poor space segment geometry is presented in the paper. Existing "snapshot" RAIM methods and algorithms which are used in practical applications have been developed for airborne receivers, thus two main assumptions have been made. The first one is that the geometry of visible satellites is strong. It means that the exclusion of any satellite from the positioning solution don't cause significant deterioration of Dilution of Precision (DOP) coefficients. The second one is that only one outlier could appear in pseudorange measurements. In case of SUAV operating in harbour these two assumptions cannot be accepted. Because of their small dimensions, GNSS antenna is only a few decimetres above sea level and regular ships, buildings and harbour facilities block and reflect satellite signals. Thus, different approach to "snapshot" RAIM is necessary. The proposal to method based on analyses of allowable maximal separation of positioning sub-solutions with using some information from EGNOS messages is described in the paper. Theoretical assumptions and results of numerical experiments are presented.

Keywords: GNSS; RAIM; Navigation; Autonomous Vessels

INTRODUCTION

In 1995 the Full Operational Capability (FOC) of GPS and GLONASS was announced and it started the beginning of a new era in navigation. In spite of GLONASS lost his FOC after a few years, the field of satellite navigation applications continued to grow. In 2011 GLONASS regained its FOC and now together with GPS they are foundation of GNSS (Global Navigation Satellite System). The simplicity of obtaining position coordinates and integration with other devices and navigation systems has caused that nowadays GNSS is the main way of determining the location of objects in the various applications [1][2]. However, GNSS positioning in not free from the constrains. The two main ones are: limiting the number of observed satellites caused by terrain obstacles both natural and those which are result of human activities (e.g. buildings) and integrity, understood as the ability of the system to alert the users in a given amount of time that the fix errors exceeded the permissible limit. GNSS receivers have become the main source of information about the location of autonomous unmanned vehicles and in such applications high level of integrity is as much important as fixes accuracy [3].

Integrity was one of the main problem considered in phase of work on the system GPS, which has resulted in many research papers, but the main area of concern was air navigation and the focus was on the development of methods to assess the correctness of GPS fixes during the flight [4]. Two main solutions have been proposed and applied in practice: external methods (integrity monitoring by the use of external infrastructures) and internal (integrity monitoring directly by the receiver). The second ones are called RAIM (Receiver Autonomous Integrity Monitoring). Among them, a separate group are those that assess the correctness of the coordinates on the basis of a single measurement of pseudoranges for at least 5 satellites – they are called "snapshot" RAIM [5]. Both external and internal methods solve the problem of integrity in the open air in a satisfactory way. However, if the outlier in pseudorange measurement is not caused by improper functioning of the satellite but by obstacles which reflect satellite signals these methods cannot be used. External methods are not able to detect such errors because of fault detection process is carried out by the monitoring station and do not take into account the local conditions at the place where the user is (see Fig. 1). On the other hand, internal methods were designed for the air navigation and they are based on two main assumptions. The first one is that only one outlier can appear in pseudorange measurements. It was adopted on the basis of high reliability of the satellites, which causes that faulty work of two satellites at the same

time is unlikely. The second one is related to the method used to integrity monitoring. It is that the exclusion of any satellite from the positioning solution don't cause significant deterioration of Dilution of Precision (DOP) coefficients. As far as we talk about navigation in the open air there are no problems associated with these assumptions. But in case of SUAV (Small Unmanned Autonomous Vessel) operating in the harbour such approach cannot be accepted. Because of their small dimensions, GNSS antenna is only a few decimetres above sea level and regular ships, buildings and harbour facilities block and reflect satellite signals. On the one hand it causes poor space segment geometry (it means that exclusion of one satellite from the positioning solution causes significant deterioration of DOP) and on the other one more than one outlier can appear in pseudorange measurements (see Fig. 1). In this paper proposal of different approach is described.

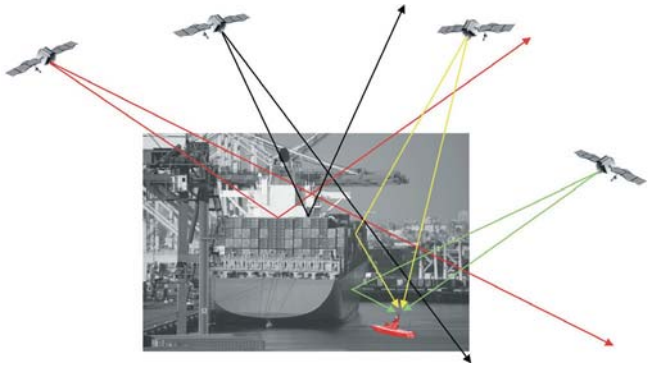

Fig. 1. Possible sources of outliers in pseudorange measurements in case of SUAV operating in the harbour

THE IDEA OF THE PROPOSED RAIM METHOD

The idea of the proposed RAIM method has been already described in [6]. It is deep modification of Maximum Solutions Separation (MSS) method proposed by R.G. Brown and McBurney in 1987 and described in [7]. The idea of the MSS method is based on the study of the maximum separation between positioning sub-solutions. The number of sub-solutions is equal the number of observed satellites, and they are formed by successive exclusion of one satellite from the positioning solution. If maximum separation of sub-solutions is greater than the acceptable one it means that there is outlier in pseudorange measurements. Described idea is shown in Fig. 2 and Fig. 3.

In Fig. 3 the idea of fault identification is also illustrated. Because of after exclusion of SV 1 from positioning solution, sub-solution (SVs: 2,3,4,5) was within acceptable limits it means that in measurement to SV 1 outlier appeared.

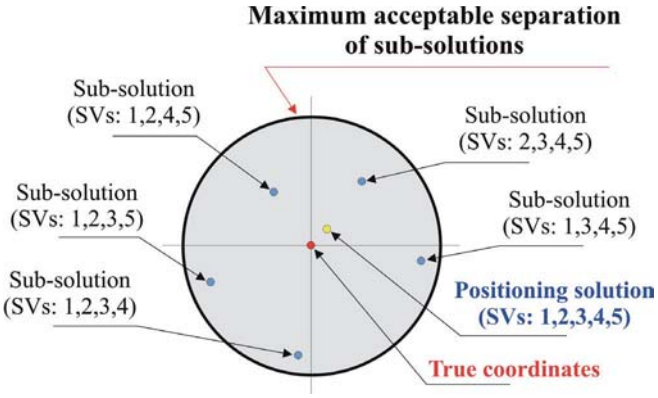

Fig. 2. Sub-solutions separation if there are no outliers in pseudorange measurements

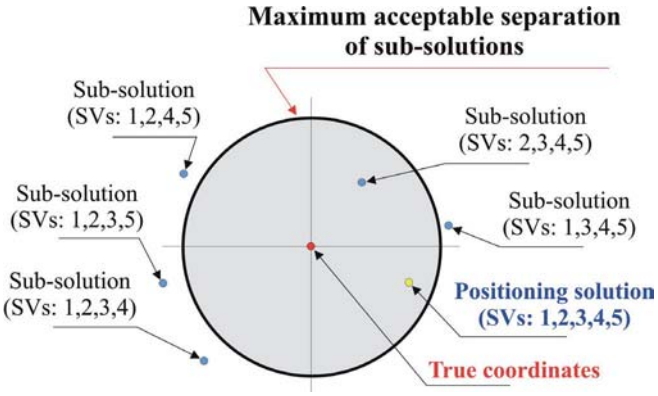

Fig 3. Sub-solutions separation if there is outlier in pseudorange measurement to SV 1

The MSS RAIM method has not found practical application due to the inability to precisely determine maximum acceptable separation of sub-solutions. In particular it was impossible in case of poor space segment geometry, because observed separation of sub-solutions could be the result of both: outlier in pseudorange measurements or significant deterioration of DOP as a result of the elimination one of the satellites from the positioning solution. This problem is described, inter alia, in [7,8]. The method proposed by author is an attempt to eliminate the above disadvantage. The research conduce on influence of pseudorange measurement errors and space segment geometry on GPS fixes distribution described, inter alia, in [9,10,11,12,14,.15,16] have shown that the extended analysis of the spatial distribution of the positioning sub-solutions can significantly improve the protection level of the existing RAIM "snapshot" methods.

The study shows that, despite the fact that at the poor space segment geometry separation of sub-solutions is similar in both cases: the outliers appeared in pseudorange measurements or they didn't appear, their spatial distribution is different. Thus, if we have the pattern of spatial distribution of sub-solutions it could be possible to determine whether there are outliers in pseudorange measurements or not, by comparing the actual distribution to the pattern. Similarity will mean that pseudorange measurements contain only random errors. The pattern of spatial distribution of

sub-solutions in case of outlies absence will be constructed in real time, on the basis of the corrections transmitted from the Satellite Based Augmentation System (SBAS) – in Europe from EGNOS.

The simplified algorithm of proposed fault detection method is as follows:

- estimating current random errors of pseudorange measurements on the basis of data received from the geostationary satellites of SBAS system,
- building the pattern of spatial distribution of sub-solutions,
- calculating of real spatial distribution of sub-solutions,
- comparing the pattern to real distribution. If both are similar it means that there are no outliers in pseudorange measurements. If not – outliers appeared.

THE SPATIAL DISTRIBUTION OF SUB-SOLUTIONS IN MSS METHOD

In practical applications we are interested in the spatial distribution of sub-solutions in relation to position calculated by the receiver, instead of to the true coordinates, because we do not know them. It is additional complication which caused that the MSS method has not been applied in practice. The research on spatial distribution of sub-solutions that were done using the software for simulating GNSS measurements, allowed to examine the issue more precisely. The results of numerical experiments were described between others in [9]. The conclusions of the study can be summarized as follows:

- if there are no outliers in pseudorange measurements, the distribution of sub-solutions in relation to positioning solution (coordinates computed on the base of observations done to all visible satellites) is a set of line segments intersecting in the middle of its length (number of line segments is equal to the number of visible satellites) – see Fig. 4.,
- if there are outliers in pseudorange measurements, the distribution of sub-solutions in relation to positioning solution is a set of line segments, which lengths are the same as in the absence of outliers but they do not intersect – see Fig. 5 and 6.

To illustrate the above, an example of the numerical simulation results is described below.

AN EXAMPLE OF THE NUMERICAL SIMULATION RESULTS

Using software simulator of GNSS measurements (described in [15]) geometrical layout of 5 GPS satellites was drawn. Azimuths and elevations of the satellites are presented in Table I. Then simulation of 86400 fixes was done, wherein it was assumed that errors of pseudorange measurements were modelled as independent random variables with N[0,1] distribution and standard deviation equal 6 m. In the first step of the simulation there were no outliers in measurements and in the second one the outlier equal 200 m and then 100 m appeared in pseudorange measurement to SV1. Obtained sub-solutions distribution related to the position computed on the base of all 5 observed satellites are presented in Fig. 4, 5 and 6.

Tab.1. Azimuths and elevations of the drawn satellites during simulation

SV	Azimuth [Ɣ]	Elevation [Ɣ]
1	328,1	53,7
2	309,3	05,8
3	011,2	34,7
4	052,5	82,3
5	240,6	44,2

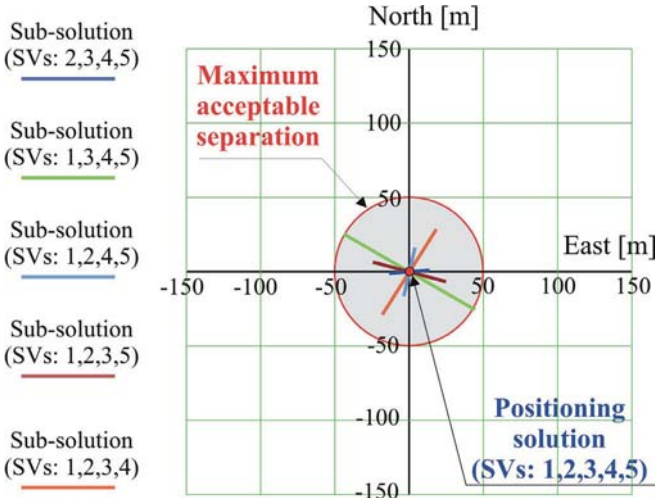

Fig. 4. Obtained sub-solutions distribution related to the positioning solution if there are no outliers in pseudorange measurements

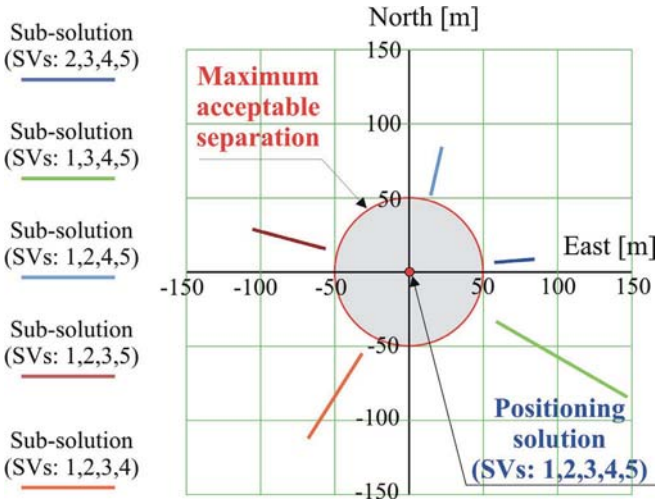

Fig. 5. Obtained sub-solutions distribution related to the positioning solution if outlier equal 200 m appeared in pseudorange measurement to SV1

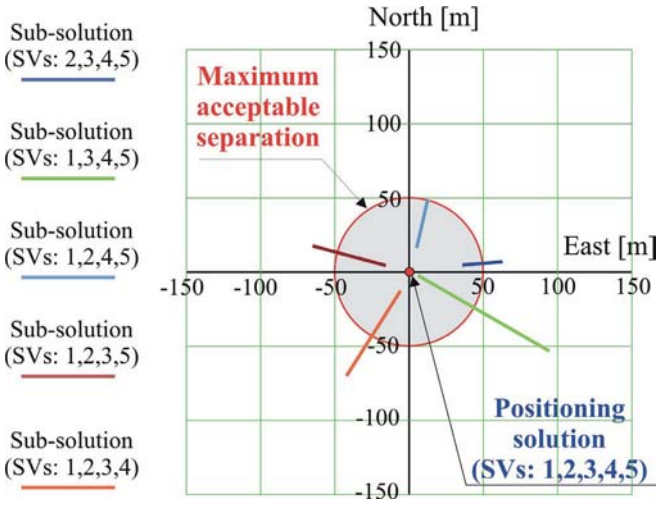

Fig. 6. Obtained sub-solutions distribution related to the positioning solution if outlier equal 100 m appeared in pseudorange measurements to SV1

The Fig. 4, 5 and 6 show, that determination of maximum acceptable separation of sub-solutions as a circle (or as a sphere in 3D) on the basis of an assumption concerning standard deviation of measurement random errors (σ_p) is not very efficient. It can be noticed in Fig. 4 that maximum acceptable separation resulting from the deployment of satellites and σ_p is equal 50 m. If outlier appears in pseudorange measurement to SV1 its value must be at least 180 m to get a 100% probability of detection. Otherwise the calculated separation of sub-solutions may be in the range of maximum acceptable separation (compare Fig. 5 and 6) which will result in outliers misdetection. On the other hand, if the value of maximum acceptable separation will be reduced, false alarms will appear, due to possibility of exceeding separation limit although there are no outliers in pseudorange measurements. It is typical situation in case of poor space segment geometry, described, inter alia, in [9,10,11,12] and main cause of very low protection level when number of visible satellites is lower than 7.

Thus, it seems to be clear that more sophisticated analyse is necessary. The presented proposal to modification of MSS method is based on estimation of current random errors of measurements on the basis of data received from the geostationary satellites of SBAS system. They allow to compute corrections to pseudorange measurements and in proposed RAIM method it is assumed that they are equal current random errors with the opposite sign. Of course it is not quite true, because of SBAS corrections don't eliminate the entire size of the random errors but it is expected that such approximation allows to improve the level of outliers detection. Of course as a source of information about current random errors of measurements DGPS system could be also used but DGPS receivers are bigger, heavier and more expensive than EGNOS ones (additional MSK module is necessary) so their application in SUAVs is not so convenient.

THE SPATIAL DISTRIBUTION OF SUB-SOLUTIONS IN MODIFIED MSS METHOD

Below an example of simulation results is described. Simulation concerned the same deployment of the satellites as described in previous section. This time drawn values of pseudorange measurements random errors were as follow: SV1: -3,2 m, SV2: 7,9 m, SV3: -5,4 m, SV4: -2,6 m, SV5: 6,1 m. Drawn values of measurements errors have given distribution of sub-solutions as shown in Fig. 7

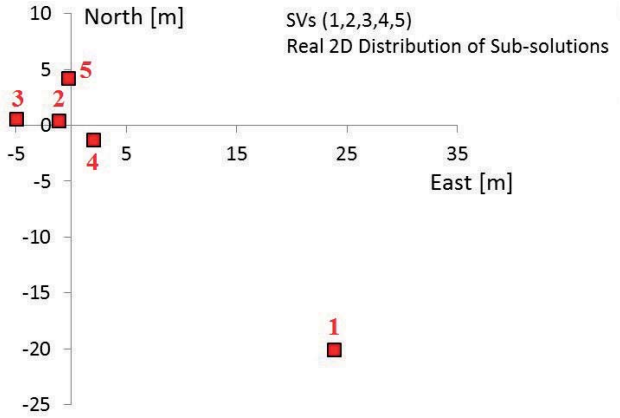

Fig. 7. Distribution of sub-solutions for drawn values of pseudorange measurements random errors. Red squares marked shift of sub-solutions related to the positioning solution. Numbers at squares indicate number of satellite excluded from the positioning solution

Because in reality random errors are unknown, in proposed method they are estimated on the base of SBAS message. It was assumed, that SBAS corrections eliminate about 85% of random measurements errors, therefore possible corrections were randomly generated. Then was assumed, that random measurements errors are equal to the corrections with the opposite sign and as a result the following estimators of random measurements errors were obtained: SV1: -2,9 m, SV2: 5,9 m, SV3: -4,5 m, SV4: -2,4 m, SV5: 5,3 m.

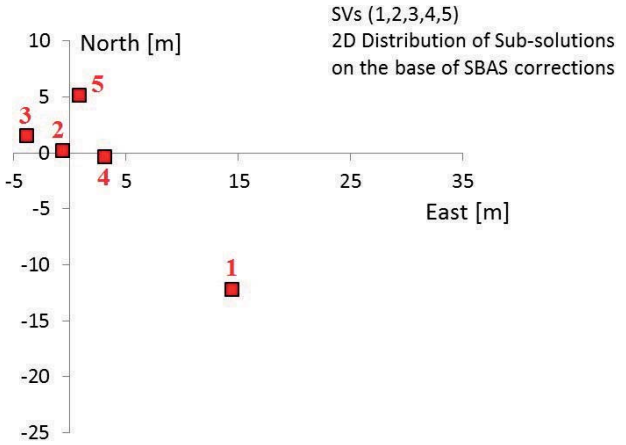

Fig. 8. Distribution of sub-solutions computed on the base of information from the SBAS message. Red squares marked shift of sub-solutions related to the positioning solution. Numbers at squares indicate number of satellite excluded from the positioning solution

Distribution of sub-solutions computed on the base of simulated information from SBAS message is presented in Fig. 8. Fig. from 9 to 13 shows distributions in case of outliers presence.

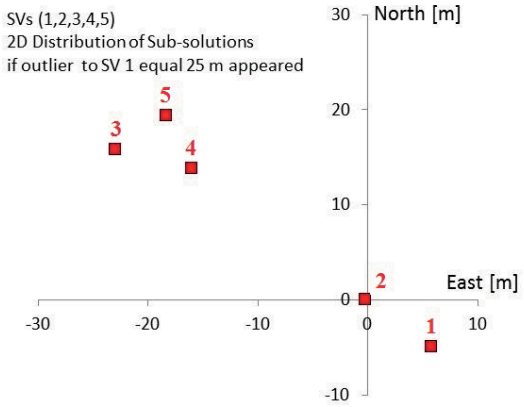

Fig. 9. Distribution of sub-solutions if outlier equal 25 m appeared in pseudorange measurement to SV1. Red squares marked shift of sub-solutions related to the positioning solution. Numbers at squares indicate number of satellite excluded from the positioning solution

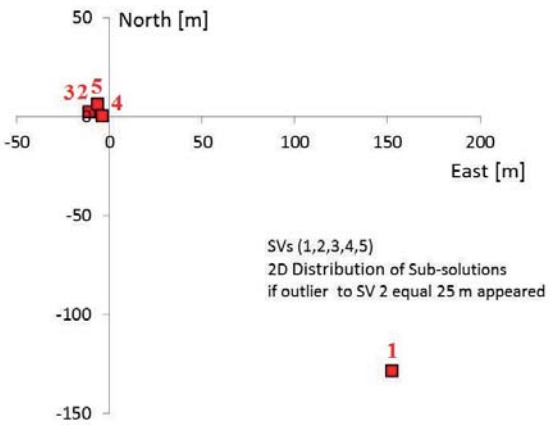

Fig. 10. Distribution of sub-solutions if outlier equal 25 m appeared in pseudorange measurement to SV2. Red squares marked shift of sub-solutions related to the positioning solution. Numbers at squares indicate number of satellite excluded

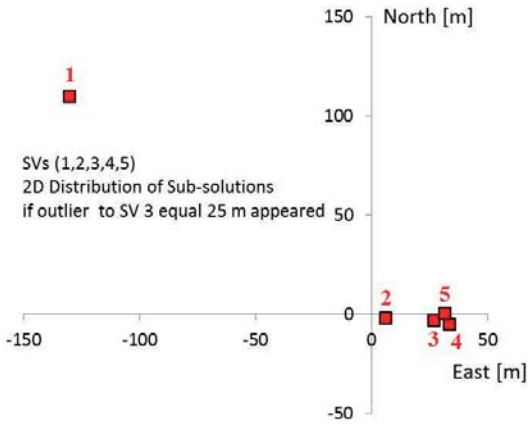

Fig. 11. Distribution of sub-solutions if outlier equal 25 m appeared in pseudorange measurement to SV3. Red squares marked shift of sub-solutions related to the positioning solution. Numbers at squares indicate number of satellite excluded from the positioning solution

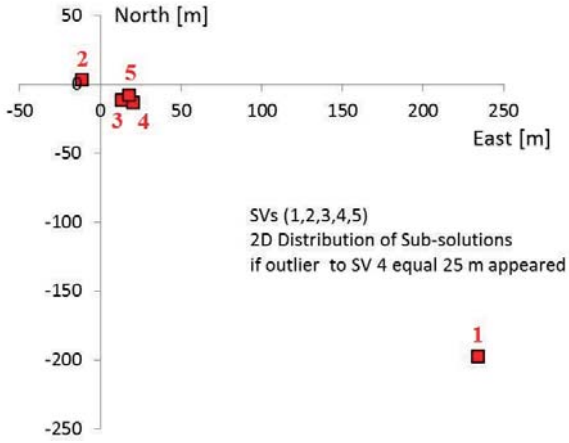

Fig. 12. Distribution of sub-solutions if outlier equal 25 m appeared in pseudorange measurement to SV4. Red squares marked shift of sub-solutions related to the positioning solution. Numbers at squares indicate number of satellite excluded from the positioning solution

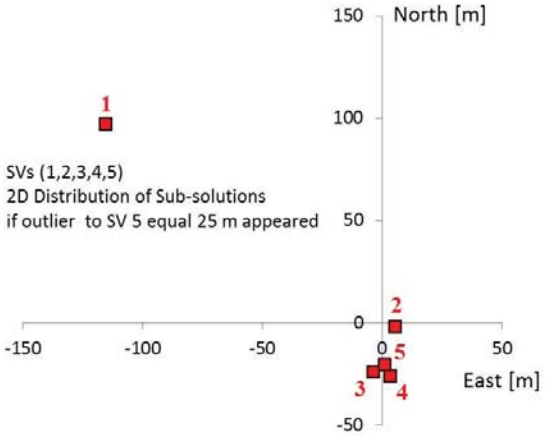

Fig. 13. Distribution of sub-solutions if outlier equal 25 m appeared in pseudorange measurement to SV5. Red squares marked shift of sub-solutions related to the positioning solution. Numbers at squares indicate number of satellite excluded from the positioning solution

It can be easily noticed, that if outlier appeared in measurements to SVs: 2, 3, 4, 5 classic MSS method is able to detect it, because separations of sub-solutions were bigger than maximum acceptable separation computed on the base of assumed standard deviation of random errors and layout of the satellites (in presented example 50 m). But in case of outlier in measurement to SV1, separation of sub-solutions is almost half less than acceptable one (is 27 m). It can be also observe if we compare Fig. 7 and 9. In such situation classic MSS method misses outlier. But if we compare spatial distribution of sub-solutions, they differ depending on outlier appeared or not (see Fig. 7, 8 and 9). Thus it seems, that extended analyse of distribution of sub-solutions can improve protection level of proposed RAIM method in comparison with the classic MSS one.

SUMMARY

The presented examples of the numerical experiment results seem to confirm hypothesis that with the pattern of spatial distribution of sub-solutions it is possible to improve protection level of classic "snapshot" RAIM method. The pattern can be built based on differential corrections received from SBAS system. Of course further research are necessary to confirm preliminary results. Thus, proposed algorithm will be implemented in GNSS measurements simulator and extensive tests will be done. They will be focused on determination of protection level with given probability of misdetection and false alarm. This will allow to reliably determine the effectiveness of the proposed solution compared to the current ones.

REFERENCE

1. A. Janowski, A. Jurkowska, D. Lewczuk, J. Szulwic, A. Zaradny, Assessment of cliff stability after the demolition of the engineering facilities, 14th SGEM GeoConference on Science and Technologies in Geology, Exploration and Mining, ISBN 978-619-7105-08-7 ISSN 1314-2704, 2 (2014) 115-124, DOI: 10.5593/SGEM2014/B12/S2.016

2. J. Dąbrowski, M. Kulawiak, M. Moszyński, K. Bruniecki, Ł. Kamiński, A. Chybicki, A. Stepnowski, Real-time web-based GIS for analysis, visualization and integration of marine environment data. Information Fusion and Geographic Information Systems, Lecture Notes in Geoinformation and Cartography, (2009) 277-288, DOI: 10.1007/978-3-642-00304-2_19

3. B.W. Parkinson, P. Axelrad: Autonomous Integrity Monitoring Using the Pseudorange Residuals, NAVIGATION 35/2 (1988) 255-274

4. C.L. Young: New Concept of Independent GPS Integrity Monitoring, NAVIGATION 35/4 (1988) 483-501

5. R.G. Brown: Receiver Autonomous Integrity Monitoring, Global Positioning System: Theory and Applications vol. II, Denver, 1996, pp.143-164

6. A. Nowak: Nowa metoda oceny dokładności wyznaczeń GNSS na potrzeby monitoringu pojazdów, LOGISTYKA 3 (2014) 4706-4717

7. R.G. Brown, P.W. McBurney: Self-Contained GPS Integrity Check Using Maximum Solution Separation as the Test Statistic, Proceedings of the International Technical Meeting of The Institute of Navigation (1987) 263-268

8. M.A. Sturza: Fault Detection and Isolation (FDI) Techniques for Guidance and Control Systems, AGARDOGRAPH 314 (1991), AGARD, NATO

9. A. Nowak: Influence of Pseudorange Measurement Errors and Space Segment Geometry on GPS Fixes Distribution, Advances in Computer Science-Network Centric Warfare, Gdynia, 2009, pp.148-154

10. A. Nowak: Protection Level of "Snapshot" RAIM Methods in Poor Geometry of Satellites, Advances in Computer Science-Network Centric Warfare, Gdynia, 2009, pp.156-162.

11. C. Specht, A. Nowak: Limitations of Satellite Positioning in Inland Shipping, Polish Journal of Environmental Studies 16, No 6B (2007) 83-86

12. A. Nowak, D. Szulc: Poziom Ochrony metod RAIM typu "snapshot" w warunkach niekorzystnej geometrii segmentu kosmicznego, LOGISTYKA 6 (2009)

13. A. Nowak: Problemy pozycjonowania satelitarnego w aglomeracjach miejskich, LOGISTYKA 3 (2011)

14. A. Nowak: Symulacje numeryczne wpływu przeszkód terenowych na dokładność wyznaczeń GNSS, LOGISTYKA 3 (2011)

15. A. Janowski, A. Nowak, M. Przyborski, J. Szulwic: Mobile indicators in GIS and GPS positioning accuracy in cities, Rough Sets and Intelligent Systems Paradigms, Lecture Notes in Computer Science 8537 (2014) 309-318

16. A. Nowak, C. Specht: Computer Simulator of GNSS Measurements, Annual of Navigation 12 (2008)

CONTACT WITH AUTHOR

Aleksander Nowak

Gdansk University of Technology
G. Narutowicza 11/12 St.
80-233 Gdansk
Poland

e-mail: aleksander.nowak@geodezja.pl
phone: +48 883 911 654

POLISH MARITIME RESEARCH 4(88) 2015 Vol. 22; pp. 9-14
10.1515/pomr-2015-0064

MARITIME LASER SCANNING AS THE SOURCE FOR SPATIAL DATA

Paweł Burdziakowski[1], Ph. D.
Artur Janowski[1], Ph. D.
Arthem Kholodkov[2], Ms. C.
Krzysztof Matysik[2], Bs. C.
Maciej Matysik[2], Bs C.
Marek Przyborski[1], Assoc. Prof.
Jakub Szulwic[1], Ph. D.
Paweł Tysiąc[1,2], Bs. C.
Aleksander Wojtowicz[1,2], Bs. C.
1) Gdansk University of Technology, Gdańsk, Poland
2) „APEKS" Ltd., Gdańsk, Poland

ABSTRACT

The rapid development of scanning technology, especially mobile scanning, gives the possibility to collect spatial data coming from maritime measurement platforms and autonomous manned or unmanned vehicles. Presented solution is derived from the mobile scanning. However we should keep in mind that the specificity of laser scanning at sea and processing collected data should be in the form acceptable in Geographical Information Systems, especially typical for the maritime needs. At the same time we should be aware that data coming from maritime mobile scanning constitutes a new approach to the describing of maritime environment and brings a new perspective that is completely different than air and terrestrial scanning.
Therefore, the authors, would like to present results of an experiment aimed at testing the possibilities of using mobile scanning at sea. Experiment was conducted in the harbour and the associated environment of neighbouring southern coast of the Baltic Sea.

Keywords: mobile laser scanning; maritime laser scanning; GIS for harbours; measurements of the sea coast; boat-based scanning

INTRODUCTION

Laser scanning (LiDAR – Light Detection and Ranging) is an effective tool to support the supply with geodetic data (geospatial) of GIS (Geographic Information Systems) in many applications. It is used for efficient, rapid and largely comprehensive high-quality data acquisition of the expected accuracy. In solutions related to the sea, the mobile laser scanning conducted from vessels gains in importance (Maritime Laser Scanning – MarLS). It belongs to a group of Mobile Laser Scanning (MLS), but the specificity of a ship movement and conditions of marine environment introduces a differences that should be taken into account in the planning and conducting of scanning from the sea.

In the context of the usefulness of data, it can be argued that MarLS can be a great addition to the electronic nautical charts used among of the of marine navigators and pilots (Electronic Nautical Charts – vessels; FMS – Navigation Display – aircrafts). These are systems in which the characteristics of availability and reliability must be above 99.5% (SoL systems – EGNOS Safety of Life). In the appropriately processed form, data from laser scanning, mobile (MLS), air (Airborne Laser Scanning – ALS) or maritime (MarLS) could be the basis for a supply with data of the highly augmented reality (Augmented Reality – AR) which makes it simpler for the people responsible for the control of their vessels to move under the conditions of degraded visibility, at night or under any other situations when the standard mark relating to the position of their vessels (floating/air) on an electronic chart might be insufficient.

In addition, in the light of contemporary existing threats (e.g. terrorism, maritime disasters), the issues of critical infrastructures objects safety have become a very important. Changes taking place in the world also affect the situation in developed countries so far considered as safe, and it unfortunately means that every object of critical coastal infrastructure or a maritime transport means could be a potential target of a terrorist attack. Hence, the issues related to the wide security, including the so-called perimeter security become very important. The use of technical means to protect objects is now becoming a common procedure. Ensuring the protection of huge companies – such as refineries, airports and harbours – requires the use of highly advanced solutions. In this matter, the technologies from the field of optoelectronic systems, IT systems, spatial information management systems (GIS) are applied. The GIS can be considered as a platform

for the integration of different sources of information within single system ensuring the visualization of danger sources as well as the broad planning and simulation of all kinds of activities related to ensuring a high level of security of the protected objects. The basis for the effectiveness of such a system is reliable information about the space. An example of the method of obtaining such information may be a project of scanning the seacoast along with the harbour infrastructure which is focused on the system approach to the safety of such objects. Wide opportunities currently offered by spatial information management systems make it possible to construct GIS platform which provides the basis for the development of the multimodal system - a tool and support for people responsible for the efficiency of anti-crisis activity in case of such circumstances.

Within the frames of the experiment, the test imaging of Władysławowo harbour with a part of sea coast (including cliffs) on the southern coast of the Baltic Sea was performed. In order to assess the suitability of MarLS data, the analyses related solely to this technology were presented without replenishing the data with ALS and geodetic measurements carried out on the land.

EXPERIMENT REALIZATION METHOD

To acquire spatial data, a scanning set based on Riegl GmbH VMZ-400 mobile scanning system was used. The system consisted of VZ-400 scanner (primarily developed for the purpose of stationary scanning) and multiple frequency and multi-system GNSS Global Navigation Satellite System) receiver connected with IMU (Inertial Measurement Unit), which is responsible for the accurate determination of the parameters of platform movement. Laser scanner (e.g VMZ-400) is a device quite often tested in a mobile solutions [1,2,4,8,12,15,17], as well as for the purpose of scanning from surface of the water [9,15,22,25], but scanning the open sea is still an innovative and problematic solution. VZ-400/VMZ-400 scanner is capable of operating in any inclination which makes it useful under difficult or untypical conditions such as sea conditions. Depending on the selected scanning mode – Long Range (LR) and High Speed (HS) – the scanning range is up to 600m (registration up to 42 thousands points per second) or 350 m (up to 122 thousands points per second) for optimal atmospheric conditions and physical properties of the scanned surfaces.

Supporting platform for the scanning was system K/H Tucana ship (hydrographic boat). This ship has overall length of 21.87 m, width of 5.70 m, draught of 1.75 m and the maximum displacement of 80 GT (Gross Tonnage). A large longitudinal and lateral stability of K/H Tucana was essential for the correct scanning especially in terms of scan density. As an experiment, the portion of the Baltic coast at the section from the fishing harbour in Władysławowo to the cliffs in the western part of Jastrzębia Góra was subjected to imaging. Thus allowed to obtain the imaging in form of the scanned port infrastructure (Fig. 1), plane sandy beaches (Fig. 2) and the steep sea coasts (Fig. 3).

The workstation of the scanning system is located on the left side of the upper deck. The platform was fixed rigidly to the available, fixed points of the deck (Fig. 3). The method of installation and the characteristic construction of the upper deck forced a constant slope around the transverse and longitudinal axis of the vessel [3,19,20,23,24]. The values of pitch (rotation around the side-to-side axis), roll (rotation around the front-to-back axis) also were changing during the scan because of the rolling of the ship, which - summed up with a constant slope – is presented in figures 4 and 5.

After initializing the parameters of IMU/GNSS system and scan, the registration of data obtained from scanning on mobile PC (with increased resistance to weather conditions) were started. This computer was one part of the user segment, responsible for the control of the hybrid scanner operation. Despite the good geometry of the GNSS space segment, the yaw angle measurement errors occurred (around the Z axis perpendicular to the plane of vessel deck) due to its instability. This stability can be achieved only through the so-called dynamic alignment. In mobile scanning, it consists in alternating acceleration and deceleration and sudden changes in movement direction of the scanning unit before and during the registration in MLS technology. While it is easily achievable in terms of road traffic, whereas in case of moving of the scanning system in the water (MarLS) this method can not be used satisfactorily.

Scanning was started within the port area, so the difficulty was to develop a high speed of the ship and to perform calibration manoeuvres before scanning. Despite the large number of available GNSS satellites, yaw angle measurement errors occurred (rotation around the vertical axis). Low speed of the unit became an advantage in terms of the density of the recorded points. To obtain unit movement data, the system of LV POS and RiAcquire program, supplied by Riegl GmbH, were used. In mobile scanning with the use of VZ-400 scanner, the information about the vehicle movement is used - its activity is recognized thanks to DMI device (Distance Measurement Indicator). When scanning from the sea, it is not possible, which makes it impossible to detect the motion what is in turns important in case of slow port manoeuvring with unstable IMU parameters. Thus, the maritime laser scanning may be characterized by an additional impact of this parameter's uncertainty errors. However, the development of IMU/GNSS positioning technology may have a significant effect on the elimination of this phenomenon [11].

Fig. 1. The area of the fishing port – manoeuvring among the wharves and other vessels.

Fig. 2. Scanning the sea beaches of a small slope of the terrain

Fig. 3. Scanning cliffs and steep sea coasts

When planning maritime works using MarLS, it is necessary to take into account the hydrometeorological conditions. For MarLS, it is particularly important to take into account the transparency of air?, air temperature, wind and sea conditions. During the preparation to the experiment data from http://model.ocean.univ.gda.pl/ and http://www.meteo.pl/ has been used [13].

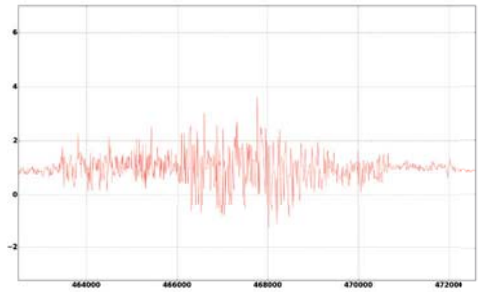

Fig. 4. Change of the roll value during measurements (X-axis - time expressed in seconds, Y-axis - the slope expressed in degrees)

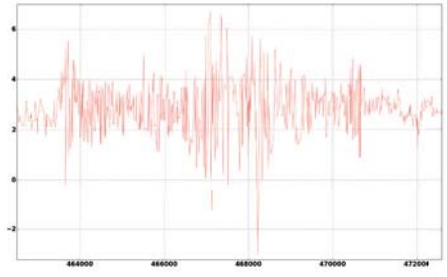

Fig. 5. Change of the pitch parameter value during measurements (X-axis – time expressed in seconds, Y-axis – the slope expressed in degrees)

SCANNING RESULTS

Data study is the standard procedure consisting of the scanner movement trajectory alignment (Fig. 6) and appending next scan records to it. As a result of the alignment only with GNSS reference stations network (ASG-EUPOS: formal geodetic control network in Poland) the expected positioning accuracy is a sub-meter value. In case of using reference points and planes measured with geodetic instruments and GNSS receivers based on the geodetic control network and after attaching them to the measurement, the results of measurements with error of 0.1-0.2 m for trajectory positioning are achievable. In comparison to the land-based measurements [11] – especially in urban areas and covered by high vegetation – the open horizon is a facilitation in case of performing measurement from the sea, so we are able to obtain very good factors for GNSS measurements and a large number of satellites used for positioning.

Adjustment:

Processing Mode:	Mobile Laser Scanning
Adjustment executed in:	00:01:51
Trajectory adjusted on:	4.46 %

Trajectoy: sbet_Mission 1_ok (1)

Statistics of Position Corrections

	abs mean [m]	rms [m]	max [m]
Along-Track:	0.0268	0.0534	0.4024
Cross-Track:	0.0207	0.0534	0.4749
Height:	0.0109	0.0174	0.0876
Total Positional Deviation:	0.0424	0.0775	0.4864

Statistics of Orientation Corrections

	abs mean [deg]	rms [deg]	max [deg]
Roll Angle:	0.00334	0.01604	0.16692
Pitch Angle:	0.00439	0.01187	0.07907
Yaw Angle:	0.14855	0.35749	2.79574
Total Angular Deviation:	0.14910	0.35804	2.80090

Fig. 6. Alignment and calculation of scanner motion trajectory.

In the data coming from the alignment of scanning system, there are interesting corrections of the positions (Fig. 7) and orientation (Fig. 8). Large position corrections are highly visible – up to 0.49 m – for the position at the beginning and at the end of the scan, when vessel was located in harbour. At the correction of orientation, it was possible to observe bigger angular corrections - up to 2.80 degree – within the port (but only for the yaw parameter).

This is the consequence of the need to reach by the ship correct speed and shape of the trajectory necessary for initializing the gyro. The device, after initialization, is working properly, providing appropriate adjustments in positioning and orientation at a speed greater than the required minimum. At low speed of the ship gyroscope stops providing satisfactory adjustments for a certain precision measurements (you can see it on the ends of the charts Fig. 7 and 8; in ranges: from the beginning to 462990 seconds and from 472100 seconds to the end – in the harbour and from 462990 to 472100 seconds – open sea).

The development of trajectory has allowed to locate it in the harbour in .kml format which is possible to be imported to GIS for the common mapping systems (Fig. 9).

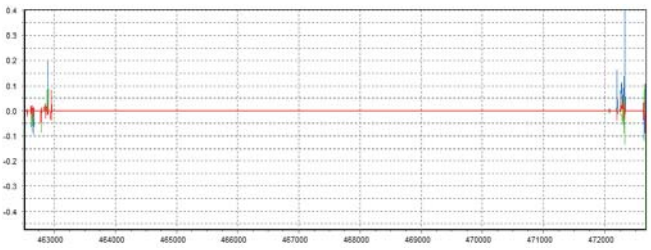

Fig. 7. Correction of scanning system position (X-axis – time expressed in seconds, Y-axis – adjustments to the position in meters – blue colour, cross track – green colour and height – red colour)

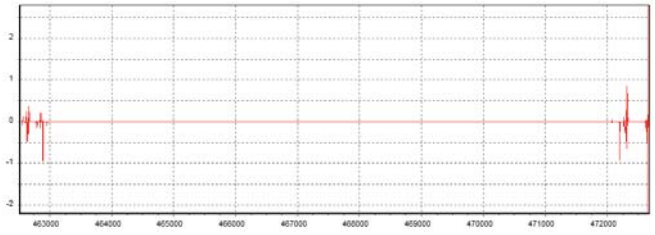

Fig. 8. Correction of scanning system orientation (X-axis – time expressed in seconds, Y-axis – adjustments to the slope expressed in degrees, roll – blue colour, pitch – green colour and yaw – red colour)

The development of trajectory has allowed to locate it in the harbour in .kml format which is possible to be imported to GIS for the common mapping systems (Fig. 9).

Using the analysis related to the points cloud characteristics it became possible to make an assessment of the scan accuracy for the harbour area (Fig. 9) and to determine the density of the points cloud for the scanned coast (Fig. 13). The "deviation" accuracy parameter has the particular importance for the quality of scan (Fig. 10) - the higher the value, the higher the measurement uncertainty for the given point on the scan. It is possible to notice the regularity, according to which this parameter is increased in areas where the laser beam falls at a slight angle ("slips"), refracts and reflects taking into account the changes in the density of the centre (e.g. in a shallow water). Whereas in the figure 13 it is possible to observe the variable density of the scan at seashore which is specific for MarLS. Variable-density areas are arranged in lanes perpendicular to the motion of the vessel. This imperfection results from the poor compensation of ship speed, resulting from the wave.

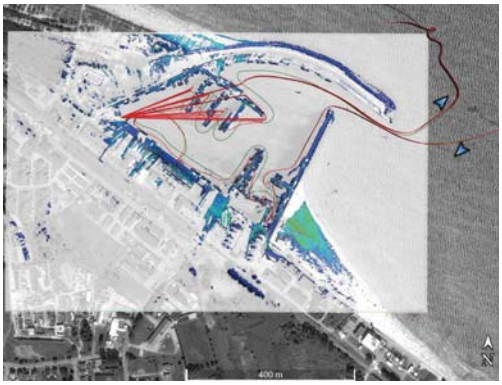

Fig. 9. Trajectory of the scanner movement imposed on Google Earth™ for the port: raw red colour and aligned – green, with the designation of exit and entrance to the port

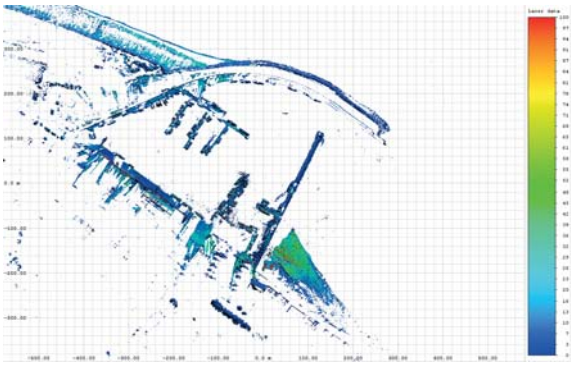

Fig. 10. MarLS data visualization for Władysławowo port with the determination of the accuracy parameter – deviation (Laser data – the level of losing the confidence to the quality and accuracy of the data)

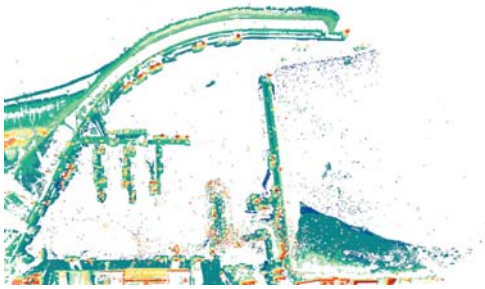

Fig. 11. MarLS data visualization for Władysławowo harbour taking into account the parameter of height above sea level

The use of geodetic spatial references system enabled to provide the characteristics of the height above sea level for the registered data (Fig. 11). As a result of carrying out the experiment, it was possible to obtain the spatial data (with reference to the geodetic spatial reference system), from which it is possible to carry out spatial analyses related to the seashore and port infrastructure (Fig. 12).

Fig. 12. MarLS visualization for vessels in harbour and port infrastructure (Laser data – number of points per square meter)

Fig.13. MarLS visualization for the coast fragment with the cloud density parameter of approximately 30 points per m2 for the green colour to approximately 100 points per m2 for the red colour

DISCUSSION AND CONCLUSIONS

The results of the performed experiment show that MarLS might be very useful to supplement the maps of approaches to harbours and coasts with satisfactory accuracy (about 0.10 m). The results and the obtained models can be a source for supplying marine charts systems (also within the frames of sailing directions) with the information based on visualizations and 3D presentations. Experiments carried out in recent years by various authors suggest that the use of a 3D maps improves the quality of navigation [5,6,18,21,22], and may also help to improve the safety of vessels and to protect water regions against danger [7,10,16,17]. Ease of obtaining spatial data and technological capabilities of scanning allow to assess the presented solution as the technology that in the short time will become the standard method of obtaining information about the coast of seawaters and inland waters. The combination of data from maritime scanning and terrestrial scanning with photogrammetry (especially for the items requiring high-precision of imaging – e.g. aid in navigations) and with the ALS air scanning (especially for horizontal surfaces and slopes with the small inclination angle) will allow for the construction of a satisfactory 3D model for the supply of geographic information systems and for the complementation of nautical maps and electronic navigation systems on vessels. It seems to be forward-looking to implement LiDAR data [1,12] along with realized analyses and algorithms into MarLS as well as sea to implement sea cliffs geometry studies based on TLS [7,10].

Specific problems are related to the difficulty to compensate the variable slope of the scanning unit and variable ship speed associated with the waviness. The characteristics of this factor refer mainly to wave parameters: its period, length and height. The parameter should be purposefully skipped, because the measurement make sense on a certain sea state, specified with some margin. When taking into account only the height of waves, the range from 0.5 to 1.25 should be the maximum range, which corresponds to the sea state of 3.

Keeping in mind the quality of the measurement, its density, uniform distribution of points (so similar criteria as for air scanning), it is necessary to refer to these parameters which make it difficult the calm and uniform vessel movement on the water (the lower and longer wave the rolling of the hull, transferred onto the rigidly installed platform of the scanner is smaller). The occurrence of a short hull tugging wave should be connected with the fact, that within the scope of development there will be lanes. At the point of temporary slowdown of the translational motion, the density is higher and when the motion of the wave accelerates the vessel, the density of points is much smaller.

REFERENCE

1. Blaszczak-Bak W., Janowski A., Kaminski W., Rapinski J.: Application of the Msplit method for filtering airborne laser scanning data-sets to estimate digital terrain models. International Journal of Remote Sensing, 36(9), (2015) 2421-2437, DOI:10.1080/01431161.2015.1041617

2. Borrmanna D., Nüchtera A., Đakulović M., Maurović I., Petrović I., Osmanković D., Velagić J.: A mobile robot based system for fully automated thermal 3D mapping. Advanced Engineering Informatics, 28(4) (2014) 425-440, DOI:10.1016/j.aei.2014.06.002

3. Byoung-Guk Min, Hee-ja Jeong, Tae-Jin Ha, Joon-Seub Cha, Nam-Ho Kim: Implementation of navigation system available for marine leisure ship. International Journal of Control and Automation, 7(3) (2014) 29-36, DOI: 10.14257/ijca.2014.7.3.04

4. Chen C., Liu H., Liu Y., Zhuo X.: High accuracy calibration for vehicle-based laser scanning and urban panoramic imaging and surveying system. MIPPR 2013: Multispectral Image Acquisition, Processing, and Analysis, SPIE 8917 (2013) 89170Y, DOI: 10.1117/12.2031466

5. Chybicki A., Kulawiak M., Lubniewski Z., Dabrowski J., Luba M., Moszynski M., Stepnowski A.: GIS for remote sensing, analysis and visualisation of marine pollution and other marine ecosystem components. Proceedings of the 2008 1st International Conference on Information Technology, ISBN: 978-1-4244-2244-9 (2008) 223-226

6. Dong-Taur S., Lo D.C., Cheng-Wu C., Yi-Chang H.: The integration of nautical charts to reconstruct 3D harbor area models and apply assisted navigation. Natural Hazards, 66(2) (2013) 1135-1151, DOI: 10.1007/s11069-012-0516-7

7. Dudzinska-Nowak J., Wezyk P.: Volumetric changes of a soft cliff coast 2008-2012 based on DTM from airborne laser scanning (Wolin Island, southern Baltic Sea). Journal of Coastal Research, 70 (2014) 59-64

8. Elseberg J., Borrmann D., Nüchter A.: Algorithmic solutions for computing precise maximum likelihood 3D point clouds from mobile laser scanning platforms. Remote Sensing, 5(11) (2013) 5871-5906, DOI: 10.3390/rs5115871

9. Hohenthal J., Alho P., Hyyppä J., Hyyppä H.: Laser scanning applications in fluvial studies. Progress in Physical Geography. 35(6) (2011) 782-809, DOI: 10.1177/0309133311414605

10. Janowski A., Jurkowska A., Lewczuk D., Szulwic J., Zaradny A.: Assessment of cliff stability after the demolition of the engineering facilities. 14th SGEM GeoConference on Science and Technologies in Geology, Exploration and Mining. ISBN 978-619-7105-08-7 ISSN 1314-2704, 2 (2014) 115-124, DOI: 10.5593/SGEM2014/B12/S2.016

11. Janowski A., Nowak A., Przyborski M., Szulwic J.: Mobile indicators in GIS and GPS positioning accuracy in cities. Rough Sets and Intelligent Systems Paradigms, RSEISP 2014 Book Series: Lecture Notes in Computer Science (LNCS) 8537 (2014) 309-318, DOI: 10.1007/978-3-319-08729-0_31

12. Janowski A., Rapinski J.: M-split estimation in laser scanning data modeling. Journal of the Indian Society of Remote Sensing, 41(1) (2013) 15-19, , DOI: 10.1007/s12524-012-0213-8

13. Jedrasik J., Szymelfenig M.: Ecohydrodynamic model of the Baltic Sea. Part 2. Validation of the model, Oceanologia, 47(4) (2005) 543-566

14. Jia-Liang S., Duo-Hu H., Quan H., Tie-Ying L., Chao Z.: Research of analysis and three dimensional display on international standard chart. Geomatics & Spatial Information Technology, ISSN 1672-5867 (2014)

15. Kholodkov A., Matysik K., Matysik M., Szulwic J., Tysiąc P., Wojtowicz A.: Morski skaning laserowy infrastruktury portowej na przykładzie portu we Władysławowie (in Polish). Logistyka. 6 (2014) 14317-14328

16. Kulawiak M., Chybicki A., Moszynski M.: Web-based GIS as a tool for supporting marine research. Marine Geodesy, 33(2-3) (2010) 135-153, Art. No. PII 923578807, DOI: 10.1080/01490419.2010.492280

17. Michoud C., Carrea D., Costa S., Derron M.H., Jaboyedoff M., Delacourt C., Maquaire O., Letortu P., Davidson R.: Landslide detection and monitoring capability of boat-based mobile laser scanning along Dieppe coastal cliffs, Normandy. Landslides, 12(2) (2014) 403-418, DOI: 10.1007/s10346-014-0542-5

18. Przyborski M.: Possible determinism and the real world data. Physica A – Statistical Mechanics and its Applications, 309(3-4) (2002) 297-303, Art. No. PII S0378-4371(02)00565-4, DOI: 10.1016/S0378-4371(02)00565-4

19. Schopp P., Klingbeil L., Peters C., Manoli Y.: Design, geometry evaluation, and calibration of a gyroscope-free inertial measurement unit. Sensors and Actuators A-Physical, 162(2) (2009) 379-387

20. Sørensen A.J.: Dynamic positioning control systems for ships and underwater vehicles. Encyclopedia of Systems and Control (2014) 1-10, DOI: 10.1007/978-1-4471-5102-9_122-1

21. Stateczny A., Bodus-Olkowska I.: Hierarchical hydrographic data fusion for precise port electronic navigational chart production. Telematics – Support for Transport TST, 471 (2014) 359-368, DOI: 10.1007/978-3-662-45317-9_38

22. Studnicka N., Zach G.: Mobile laser scanning in Venice: Grand Canal in scan and image data. GIM international, 25(4) (2011) 20-23

23. Townsend N.C., Shenoi R.A.: Control strategies for marine gyrostabilizers. IEEE Journal of Oceanic Engineering, 39(2) (2013) 243-255, DOI: 10.1109/JOE.2013.2254591

24. Witkowska A., Tomera M., Smierzchalski R.: A backstepping approach to ship course control. International Journal of Applied Mathematics and Computer Science 17(1) (2007) 73-85, DOI: 10.2478/v10006-007-0007-2

25. Wojtowicz A., Tysiac P., Szulwic J., Janowski A.: Airborne and mobile laser scanning in measurements of sea cliffs on the southern Baltic. 15th International Multidisciplinary Scientific GeoConference SGEM 2015, June 18-24, 2015, 1(2) (2015) 17-24, DOI: 10.5593/SGEM2015/B12/S2.003

CONTACT WITH AUTHOR

Jakub Szulwic
Paweł Burdziakowski
Artur Janowski
Marek Przyborski
Paweł Tysiąc
Aleksander Wojtowicz

Faculty of Civil and Environmental Engineering
Gdansk University of Technology
Narutowicza 11/12
80-233 Gdansk
Poland

Arthem Kholodkov
Krzysztof Matysik
Maciej Matysik
Paweł Tysiąc
Aleksander Wojtowicz

Engineering Services Company
„APEKS" Ltd.
Jaskowa Dolina 81
80-286 Gdańsk
Poland

POLISH MARITIME RESEARCH 4(88) 2015 Vol. 22; pp. 15-20
10.1515/pomr-2015-0065

DESIGN OF THE DUAL CONSTELLATION GPS/GALILEO MOBILE DEVICE FOR IMPROVING NAVIGATION OF THE VISUALLY IMPAIRED IN AN URBAN AREA

K. Drypczewski, Ms. C.
M. Moszyński, Assoc. Prof.
J. Demkowicz, Ph. D.
K. Bikonis, Ph. D.
A. Stepnowski, Prof.
Gdańsk Univeristy of Technology, Poland

ABSTRACT

The article discusses damages of essential tribological associations in crankshaft and piston systems of large power two-stroke engines used as main engines, which take place during transport tasks performed by those ships. Difficulties are named which make preventing those damages impossible, despite the fact that the technical state of engines of this type is identified with the aid of complex diagnostic systems making use of advanced computer technology. It is demonstrated that one of causes of the damages is the lack of research activities oriented on recognising random properties of the loads leading to those damages. A proposal is made for the loads acting at a given time t on tribological associations in crankshaft and piston systems of internal combustion engines used as main engines to be considered as random variables Q_t. At the same time the loads examined within a given time interval $t_r \leq t \leq t_z$ would be considered stochastic processes $\{Q(t): t \geq 0\}$. Essential properties of the loads of the abovementioned tribological associations are named and explained by formulating hypotheses which need empirical verification. Interval estimation is proposed for estimating the expected value $E(Q_t)$ of the load Q_t acting at time t. A relation is indicated between the mechanical load and the thermal load acting on tribological associations in the ship main engine crankshaft and piston system. A suggestion is formulated that a stochastic form of the relation between these types of load is to be searched for, rather than statistic relation, and a proposal is made to measure the intensity (strength) of the stochastic relation using the Czuprow's convergence coefficient.

Keywords: dual constellation receiver; GPS; Galileo; Voice Maps; navigation for the blind; visually impaired; personal navigation device; PND

INTRODUCTION

The main objective of presented research is a feasible improvement of the performance of existing mobile personal navigation devices (PND) for pedestrian navigation in urban areas, in particular for blind and visually impaired persons.

It is well known by users of PND and other GPS-based devices that positioning suffers from (local) significant decreases of accuracy in partially obscured environments like urbanized areas, where buildings (especially high buildings), trees or terrain block large portions of the sky [4].

In such areas, GPS receiver performance is usually deteriorated by the reduced number of currently available satellite signals, as well as by introducing their multipath. That is why the GPS positioning in dense urban areas is unreliable, with poor positioning accuracy, particularly in the cross-street direction if a street is surrounded by high buildings. This problem is crucial, especially in the context of solutions based on GPS receivers dedicated for users with special requirements. An example may be blind and/or visually impaired persons using the low cost PND to support their movement, when high precision positioning is required, especially in the context of emergency situations.

The above-mentioned problem of existing GPS receivers' performance deterioration in partially obscured environments in the context of GPS errors is illustrated in Figure 1.

As is seen in such urban areas, the geometry of the available GPS signals is strongly affected; as several satellites are hidden for the GPS receiver, as the „lines of sight" (LoS) going across the street are much more likely to cross buildings. It affects significantly the ellipsoidal error and, as mentioned above, makes the accuracy worse, especially in the across-the-street

direction, where tall buildings usually interfere with the direct "line-of-sight" from many satellites at that moment, casting GPS shadows. However, as it will be shown, the proposed combined use even of a not fully operational Galileo system, in addition to GPS, will considerably enhance the direct signal availability, which should result in substantial increases of positioning accuracy and reliability.

Therefore, the proposed approach for reaching formulated technical objectives consists of examining the feasibility of integrating existing mobile PND platforms with the next-generation combined open GPS-Galileo receiver module, which provides:

1) increased number of available (visible) satellites (two constellations),
2) general enhancement of direct satellite signal availability,
3) improved availability of satellite signals in high-rise cities,
4) better coverage at high latitudes.

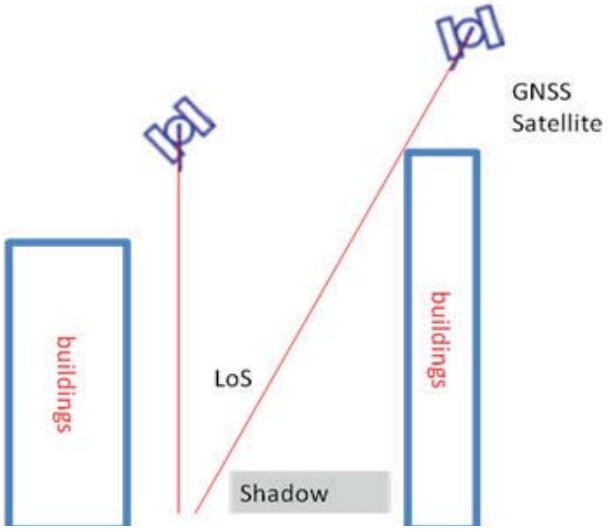

Fig. 1. a) Using direct/non-direct signal reception to determine position

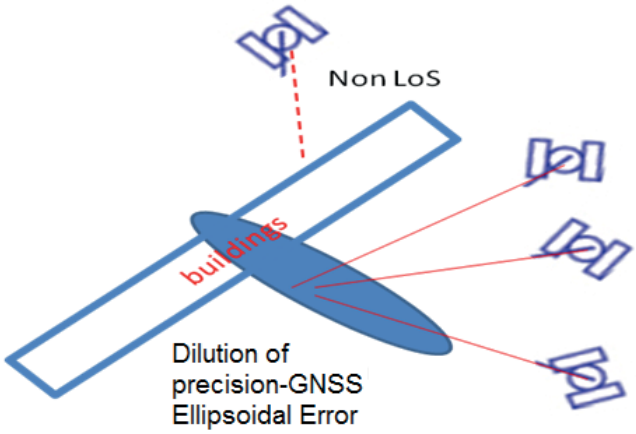

Fig.1 b) Dilution of precision (DoP) and GPS Ellipsoidal Error – aerial view

These should result in a substantial increase of positioning accuracy and reliability, even for a not fully operational Galileo system

Obviously, future deployment of a fully operational Galileo system, and future broadband signals used in GNSS systems will enhance it further.

In addition to the proposed adoption of the combined GPS/Galileo receiver module in the considered scheme, it is assumed to implement in the project two complementary optional innovations which should further improve positioning accuracy, namely: 1) application of map-matching algorithms, which should eliminate not-possible positioning (users locations) in dense urban areas, e.g. building roofs, 2) application of information source fusion using Bayesian particle filtering algorithms; this seems to be especially promising when 3D spatial data is available, (e.g. city blocks or building 3D models), and when the filter can be fed with such a priori information.

To summarize, it may be assumed that the fusion of the proposed approaches should provide additional improvements in most environments, not only in highly urbanized areas.

VOICE MAPS

During the last two years the authors were involved in the team which carried out, and successfully ended, the national project "Voice Maps" in the scheme of the Polish National R&D Center – NCBR – IniTech Project ZPB/37/67901/IT2/10, [jakaś pozycja literaturowa z VoiceMaps].

The main goal of that project was to develop a prototype system for the blind and visually impaired users in order to improve their comfort in everyday life by navigating them in the urban areas. The system includes a client application for Android mobile devices and a server [5, 6].

The application uses a multimodal user interface; combining mainly voice recognition, dedicated software keyboards, touch-driven menus and speech synthesis mechanisms. The client application calculates the optimal route for the users and then guides them to the selected target along the route. Users' geographical position and their azimuth are continuously monitored, and wrong or dangerous behaviour causes appropriate voice messages to be triggered along with information on passed objects, point of interests (POI) near obstacles and potential dangers, point of danger (POA)[12-14]. Geospatial data is acquired by the community and aggregated on the web portal, allowing preview and editing. The portal currently contains geospatial data of Elbląg city, and partial data for the city of Gdańsk [5, 6].

The "Voice Maps" project solved most of the currently basic problems of pedestrian navigation of the blind in urban terrain; i.e. appropriate digital mapping, navigation algorithms, and timeliness of topography data including the effective spatial data acquisition methods, the efficiency of pathfinding methods, and the appropriate design of the user interface employing voice recognition, speech synthesis mechanisms and touch screens of the modern mobile devices – see Figure 2.

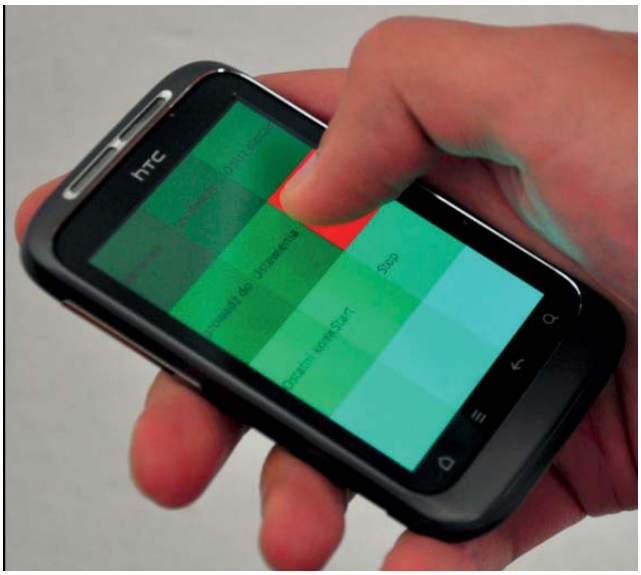

Fig.2. User interface: touch screen menu, map screen for testing, software gesture keyboard

The prototype version of "Voice Maps" system was positively evaluated by the blind consultants and has become the subject of 10 publications and a patent application [5,6].

However, these key problems were solved concurrently with the mobile system development, with one exception which constitutes the insufficient accuracy of positioning in the urbanized areas, which results in the unstable and unreliable performance of the system in difficult urban conditions. Therefore, the achievement of reliable performance of the system, assuring accurate positioning and subsequent navigation of pedestrians, as has become the objective of new research.

MULTICONSTELLATION COMBINED GPS/ GALILEO MOBILE DEVICE

As was stated in the previous paragraphs, feasibility study of Multiconstellation Combined GPS/Galileo Mobile System consists of two stages: feasibility study itself, and the second stage validating the feasibility of the developed PND system. Study commences with a presentation of the investigation carried out by the "EU-US Cooperation on Satellite Navigation Working Group C", which compares GPS, Galileo and GPS/ Galileo combined performance - simulated for three receivers – and which shows the advantages of the combined GPS/ Galileo system interoperability [2]. Simulations demonstrate and quantify the improvements that can be expected when using GPS and Galileo open services in combination, under different environmental conditions, as shown in Figure 3.

In all cases, the combined approach led to noteworthy performance improvements, as compared to single system performance. The most significant improvement is for urbanized, partially obscured, environments. The increased number of satellites available provides robust performance even when some signals are blocked, which is reflected in a significant increase of positioning accuracy and availability.

As is easily seen, the signals from elevation angles lower than 30 deg are usually discarded for the urban area. This case can be considered as a measure of satellite signal availability in hard urban environments, where direct lines of sight (LoS) below 30deg very often cannot be seen.

The same trends hold true in the 15 deg case, but the overall accuracy is lower here, e.g. 6.45 m (15 deg) versus 8.02 m (30 deg) for the SF BOC(1,1) dual constellation case.

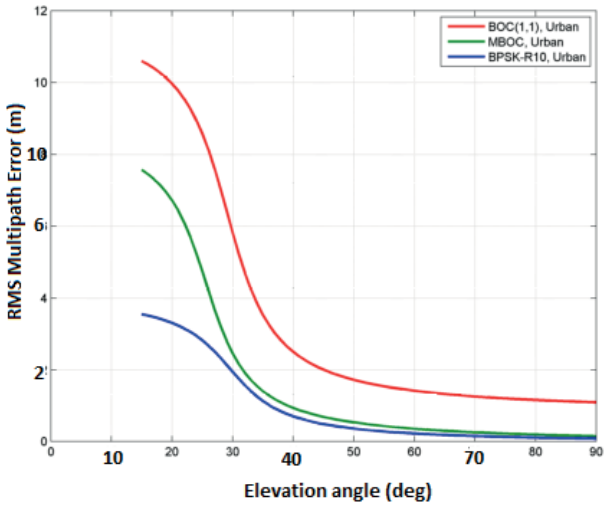

Fig. 3. RMS Multipath Error versus Elevation Angle for single and combined GNSS receivers

Figure 4 presents the user performance for future GPS-III, Galileo, and combined GPS-III/Galileo receivers in different study cases; including open, urban and half-occluded environments, as well as different ionosphere activity periods.

The figure demonstrates, again, a noteworthy availability improvement due to the combination of both constellations, showing a remarkable improvement in low-visibility areas, as well as deep-urban ones, where non-aviation users are often located when computing their position fix.

Both GPS and Galileo systems, thanks to their interoperable and compatible signal baselines, can be relatively easily integrated and processed, even by civilian-user low-cost equipment. As was shown, due to these reasons, the resulting combined use of the integrated solution offers remarkable benefits to a broad range of user communities.

In the second – development - stage of the approach, the design of the new system integrating existing mobile PND platforms with the next generation, a combined open GPS-Galileo receiver module is proposed. This supposes to validate the feasibility of the proposed solution, providing its improved performance (i.e. substantial increase of positioning accuracy and reliability).

The architecture of the system to be developed is presented in the functional block diagram in Figure 5.

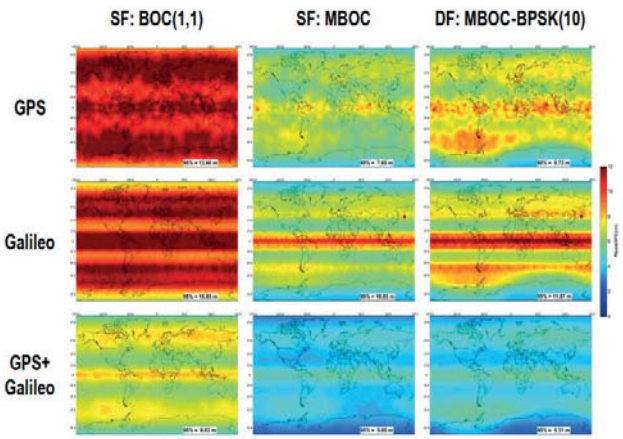

Fig. 4. Urban Global Study (30 deg) - Comparison of Mean Horizontal Position Error HPE(m) for Peak Solar Cycle

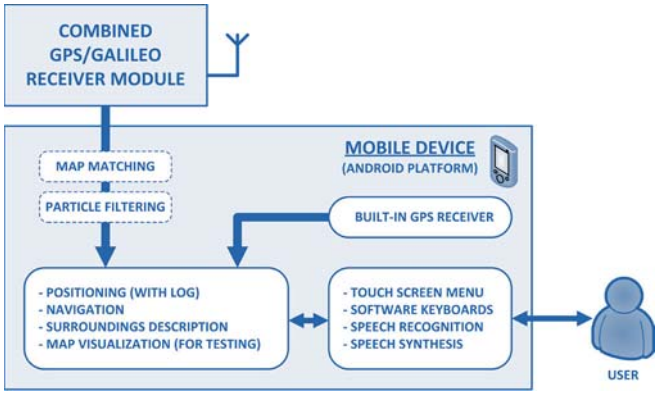

Fig. 5. System Architecture functional block diagram

In addition to the proposed integration of the combined GPS/Galileo receiver module with the existing mobile device smartphone platform – as presented in the scheme - it is assumed to implement in the proposed design two complementary optional software modules, which should further improve positioning accuracy.

The first one refers to implementing map-matching algorithms, which should improve the precision of positioning in urban areas and is described in the next paragraph.

The evaluation of more advanced techniques based on heuristics, fuzzy logic, and the matching of user movements' curves will be also investigated in the next research phase. Correlation and multi-path problems typically lead to high measurement noise and errors. Fuzzy logic and reasoning can additionally filter incorrect measurement from high-noise environments, such as GNSS signals.

Since the history of user movement is known, mathematical analysis of previous measurements can be applied. Polygonal chains of fixed numbers of last positions can be compared with topology of nearest graph vertices to produce more accurate positioning. Moreover, the area surrounded by its intersection with candidate segments can provide additional map-matching parameters.

Submitters are also planning to evaluate if heuristic methods, based on human behaviour and tracking previous movement history, can be included in the map-matching process.

The second one refers to implementing information source fusion using Bayesian particle filtering algorithms.

Particle Filtering is one of the existing methods of sensor information fusion, like Kalman filtering and Extend Kalman Filtering method. PF improves accuracy, especially in situations where there are many sources of information, and where there is a non-linear environment affecting the positioning system i.e. highly urbanized area.

Particle filters work by proposing a hypothesis of where the tracked person is located. Each particle has a position and a weight, and the weight is the confidence we have in that guess. The weight may be treated as the importance of the position calculation (e.g. for the afore-mentioned building roofs it should be reasonably low)

The movement of the particle is restricted by certain rules e.g. some barriers, no walking into walls, or we are walking at constant speed defined in the model, which means that most particles should be moved at that speed. If a particle is far from the reported position from a Galileo receiver, then the particle has its weight lowered, if the particle is close by the reported position it has its weight raised.

So, for highly urbanized areas, this kind of fusion technique seems to be suitable, and therefore seems to very promising. The fusion algorithm is planned to be implemented in the mobile device Android platform.

MAP- MATCHING

Methods described in previous paragraphs provide solutions to obtain more accurate measurements of the geographical position provided by satellite positioning systems. Even if the acquired position is more reliable, errors connected with time measurement, atmospheric effects and especially multipath issues may still occur. Navigational systems in applications for the blind must be extremely dependable and the need of an additional solution for maximizing positioning quality has emerged.

Map matching is a technique used to determine user geographical position based on location information and electronic maps. In general this problem is difficult because both location and digital geospatial data are typically not accurate [7, 8].

Since the representation of the geographical features is kept in the form of the graph, the graph theory definitions will be used. The edge or section in the graph represents linear objects, e.g. streets or sidewalks. The vertices in the graph represent crossroads, points of attention (POA), e.g. stairs, road signs or other obstacles and points of interest (POI), e.g. bus stations or hotels.

Map matching procedure begins with finding the edges in the area of received geographical location. Search should start from a fixed distance value and if an appropriate number of edges was not found, search should be repeated with higher distance value. Initial value estimation should be based on graph density. Found edges are being referred to as candidate polylines [1] or edges.

In the literature several map matching methods were proposed [1-3, 11]. The easiest one is based on finding the edge that is closest to the received position. For each of the candidate edges an orthogonal projection of current user position onto the edge is calculated. Distances, which are equal to the length of the segments between determined points and user location, are being compared and the edge with the smallest value is chosen. This solution may produce unpredictable errors as presented in Figure 6. Let us assume that user is moving along the A edge. When he is close to A and B segments' intersection his determined position is wrongfully placed on the B edge.

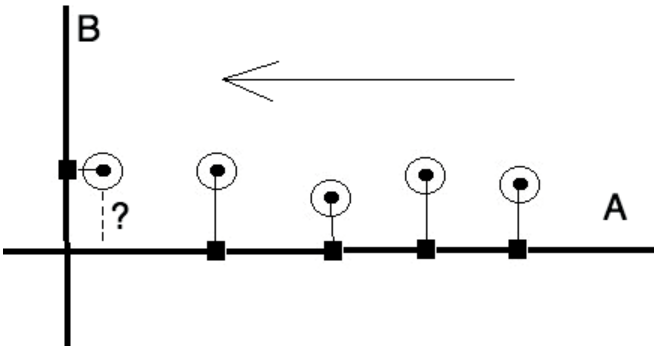

Fig..6. Incorrect map matching to the closest edge

It is clear that another set of parameters must be taken under consideration. Since the information about topological relations in graph and past travel path is available, there is a possibility to use them for error detection. Previously chosen edge can be compared with the new location data to obtain better accuracy. It can be assumed that a user may stay on the last found edge or can move to the next edge when there is a connection between them. Segments that do not have a topological relation with the previous edge should be removed from the candidate edges set. Figure 7 presents situation in which the user would be falsely placed on the B edge instead of A edge if only the closest segment method would be used.

If the time rate of a location data acquisition is high, then the distance travelled between calculated positions is sufficiently short. Therefore other map matching parameters can be established as the length of the path between previous edge and candidate segments. It can be assumed that the edge with the smallest path should be chosen. As shown in Figure 7, the path containing A, B and C edges is longer than the one containing only the A segment.

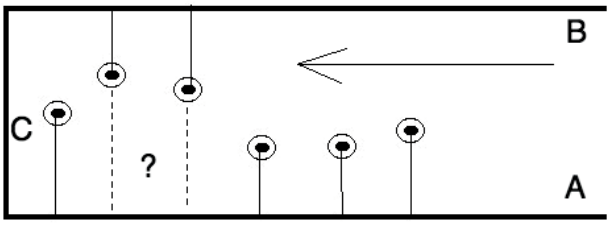

Fig. 7. Incorrect map matching to the edge without topological relation with previously selected edge

Location information contains azimuth of the movement, which can also become a parameter for map matching procedure. The angle of the candidate edge can be compared with the azimuth to estimate the approach degree. It can be assumed that the edge with the smallest angle difference is the one to be chosen during the map matching process. Figure 8 presents a situation in which previously described methods would produce incorrect results. Comparing the angle approach can provide data that will allow determining the correct solution.

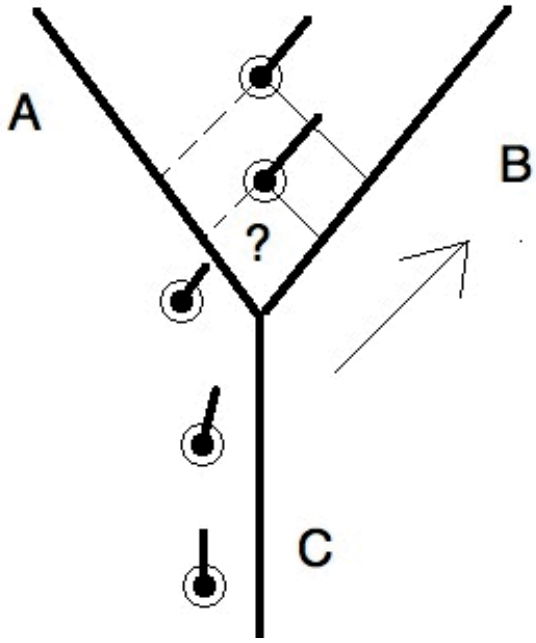

Fig. 8. Map matching using approach degree estimation

The map matching process uses all of the aforementioned methods. The presented algorithm calculates distance d between received location and the point of the orthogonal projections onto all of the elements of the candidate segments set. Thereafter, the path distance p as well as the approach degree a is estimated for all edges.

In the last step, results are normalized and the weight function is created. Formula is as follows:

$$L=\omega_d d+ \omega_p p+ \omega_a a \quad \textbf{(1)}$$

where:
ω_d - distance weight,
ω_p - path distance weight,
ω_a - approach degree weight,
Edge with the smallest L value is selected in the implemented map matching process.

SUMMARY

Contemporary high-end GNSS receivers assisted with referenced systems possess 0.01 meter vertical and horizontal accuracy in open areas, however in dense urbanized areas positioning process is still not reliable. The next-generation combined open GPS-Galileo receiver module, which provides an increased number of available satellites, will provide general enhancement of direct satellite signal availability, therefore improved availability of satellite signals in high-rise cities. These should result in a substantial increase of positioning accuracy and reliability, even for a not fully operational Galileo system.

The application of map-matching algorithms, which ought to eliminate not-possible positioning in dense urban areas and application of information source fusion using Bayesian particle filtering algorithms should provide additional improvements in most environments, not only in highly urbanized areas. This is still a far from fully operational receiver concept for the visually impaired, but it is yet another approach toward solving the forward problems which still emerge e.g. sensor integration, integrity etc..

ACKNOWLEDGEMENT

This research constitutes a sort of followup of the "Voice Maps" project, which was supported by Narodowe Centrum Badań i Rozwoju (National Center of Research and Development) within the "IniTech" program (project code: ZPB /37/679 01/IT2/10).

REFERENCE

1. L. Xi, Q. Liu, M. Li, Z. Li, Map Matching Algorithm and Its Application, Advances in Intelligent Systems Research, 2007.
2. N. Tradišauskas, D. Tiešytė, C.S. Jensen, A Study of Map Matching for GPS Positioned Mobile Objects, 7th WIM Meeting, 2004.
3. S. Taghipour, M.R. Meybodi, A. Taghipour, An Algorithm for Map Matching For Car Navigation System, Information and Communication Technologies: From Theory to Applications, 1-5, 2008.
4. K. Bikonis, J. Demkowicz, Data Integration from GPS and Inertial Navigation Systems for Pedestrians in Urban Area, International Journal on Marine Navigation and Safety of Sea Transportation, Vol. 7, No. 3, pp. 401-406, 2013.
5. Ł. Kamiński, A. Stepnowski, Ł. Markiewicz, Voice Maps - system supporting navigation of the blind, Hydroacoustics, Vol. 15, pp. 83-90, 2012.
6. A. Stepnowski, Ł. Kamiński, J. Demkowicz, Voice Maps - the system for navigation of blind in urban area, Proceedings of the 10th WSEAS international conference on Applied computer and applied computational science, 7-9.03.2011, Venezia, Italy, 2011.
7. L. Yang , Z. Ke, L. Tan , L. Jiabin, The Research On Real-Time Map-Matching Algorithm, Proceedings of the International Conference on Industrial Control and Electronics Engineering (ICICEE), Xi'an, China, 2012.
8. Y. Yuan, W. Guan, W. Qiu, Map Matching of Mobile Probes based on Handover Location Technology, Proceedings of the International Conference on Networking, Sensing and Control (ICNSC), Chicago, USA, 2010.
9. J. Meguro, T. Murata, J. Takiguchi, Y. Amano, T. Hashizume, GPS Multipath Mitigation for Urban Area Using Omnidirectional Infrared Camera, IEEE Transactions on Intelligent Transportation Systems, Vol. 10, Issue 1, pp. 22-30, 2009.
10. S. Bauer, M. Obst, G. Wanielik, 3D Environment Modeling for GPS Multipath Detection in Urban Areas, Proceedings of the 9th International Multi-Conference on Systems, Signals and Devices (SSD), Chemnitz, Germany, 2010.
11. Wiśniewski B., Drypczewski K., Markiewicz Ł., Kamiński Ł.:Methods of navigation in the mobile application supporting movement of the blind// In: HYDROACOUSTICS.-Vol. 16 (2013),s.243-252
12. Drypczewski K., Kamiński Ł., Markiewicz Ł., Wiśniewski B., Stepnowski A.:Remote Spatial Database Access in the Navigation System for the Blind// In: Marine Navigation and Safety of Sea Transportation: Navigational Problems.-, (2013),s.217-221
13. Markiewicz Ł., Drypczewski K., Wiśniewski B., Kamiński Ł.: Client-server Approach in the Navigation System for the Blind. TransNav, the International Journal on Marine Navigation and Safety of Sea Transportation, Vol. 7 No. 3 ISSN 2083-6473 (e-ISSN 2083-6481).
14. Markiewicz Ł., Drypczewski K., Wiśniewski B., Bieliński T.:Application development for Android, iOS and BlackBerry mobile platforms// In Proc. ICT YOUNG 2013/.Gdańsk:Faculty of Electronics, Telecommunications and Informatics, Gdańsk University of Technology,2013,s.51-56

CONTACT WITH AUTHOR

kszyk@eti.pg.gda.pl

POLISH MARITIME RESEARCH 4(88) 2015 Vol. 22; pp. 21-26
10.1515/pomr-2015-0066

METHOD TO EXTEND OPERATIONABILITY OF WEB-GIS BASED MARINE SERVICES USING SSE PLATFORM

K. Drypczewski, Ms. C.
A. Stepnowski, Prof
K. Bruniecki, Ph. D.
Gdańsk Univeristy of Technology, Poland

ABSTRACT

Earth Observation (EO) products are widely used by geospatial society. Over the last years a number of new applications of satellite imagery were proposed. This led to an increased interest in EO products, not only from researchers but also from companies and individuals. The authors constitute the essential part of the team that created the marine, web-GIS system - SafeCity GIS - for dissemination of data obtained from a 1.5 metre HRPT-MetOp satellite ground receiving station. To increase the operationability of the system the authors successfully attempted to broaden the offered functionality by integration with Service Support Environment (SSE). Due to this, EO products for the Pomeranian Region are served as web-services; amongst them there are True Color imagery, meteorological, algae monitoring and fire-detection services. The authors present the created solution for web service support for GIS system based on Service Support Environment and discuss its advantages and disadvantages.

Keywords: EO, GIS, SSE, HRPT MetoOp, SafeCity GIS

INTRODUCTION

Earth Observation (EO) products, e.g. satellite images are the data type widely used in modern Geographical Information Systems (GIS). Companies and research institutions utilizing this data must face issues connected not only with specific system purposes, but also with more general and typical GIS problems including geoprocessing, data storage, system efficiency etc., that are typically not cost-effective and are time consuming [2, 5, 12-16].

Moreover, the complexity of modern computer systems causes a need for additional parameters to be taken into consideration. Vast systems are difficult to administer, which leads to the common issue of redundancy in the functionality offered by the software. One of the possible solutions to this is to create systems using a Service Oriented Architecture (SOA) design pattern. This pattern assumes that separate parts of the software offer functionality to other applications in the form of web services. The World Wide Web Consortium defined a web service as: "a software system designed to support interoperable machine-to-machine interaction over a network. It has an interface described in a machine-processable format (specifically WSDL)" [9]. Simply speaking, functionality offered by a specific application is achieved by chaining several basic services to one complex service. Since a service can be easily used in multiple solutions, the problem of redundancy is resolved.

During research conducted by the Department of Geoinformatics, Gdansk University of Technology, all the above issues were encountered. The authors constitute the essential part of the team that have recently developed a specialized maritime web-GIS system - the so-called SafeCity GIS - for processing and archiving of satellite imagery obtained from an HRPT-MetOp satellite ground receiving station [8]. SafeCity GIS data products are disseminated in different ways, one of them is through specialized geospatial web services. The development process provided a plausible solution; one of its aspects is the selection of the best available platform for services management. The Service Support Environment (SSE) platform was created to overcome the aforementioned problems, evaluate standards for EO products exchange and allow companies/researchers to focus on application-specific issues. In this paper the authors present the created solution for web service support for GIS systems. As a case study SafeCity GIS is used [5].

HRPT-METOP SATELLITE GROUND RECEIVING STATION

Since 2009 the Gdansk University of Technology Geoinformatics Department has operated a 1.5 metre HRPT-MetOp satellite ground receiving station capable of receiving the High Resolution Picture Transmission (HRPT) from polar

orbiting satellites. This station, with the use of an antenna located on the roof of the building (Fig. 1a) of the Faculty of Electronics, Telecommunications and Informatics, and an internal part consisting of the receiver and acquisition-storage-control computer unit, allows the receipt of data about circumpolar orbits from EOS – Earth Observing Satellites.

Fig. 1a. 1.5 metre HRPT-MetOp antenna in radome

The ground station is capable of obtaining data from the Advanced Very High Resolution Radiometer (AVHRR) which is a major sensor onboard of NOAA-15 – NOAA-19, MetOp-A and MetOp-B meteorological satellites [8, 11].

Due to the localization of the ground station (N54° 22'15.60", E18°36'45.48") and the sensor geometry constraints, the geographical areas addressed with the service mostly cover Poland, the Southern Baltic (including the Gulf of Gdansk) and some adjacent regions. The typical footprint of a registered and received satellite scene is presented in Fig. 1.

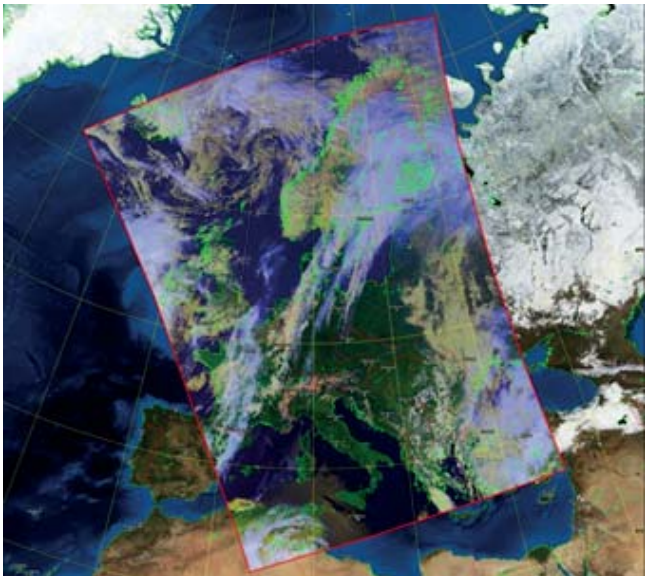

Fig. 1b. Typical footprint of the AVHRR scene received by the satellite ground station

HRPT-MetOp ground station receives the EO data on a regular basis during the satellite visibility [4]. Received information is preliminarily processed by the control panel's built-in software. Further analysis and usage of the data requires an advanced informatics solution. The SafeCity GIS [5] is a computer system associated with the station, is responsible for satellite data acquisition, archiving and dissemination. The EO satellite products are processed by the web GIS Data Adaptation Module, processing capabilities are implemented as separate routines in Data Analysis Module and may be also used with other sources of data [1].

SERVICE SUPPORT ENVIRONMENT (SSE)

Service Support Environment (SSE) is an openly distributed, service-oriented environment developed for the Ground Segment Department of the European Space Agency (ESA) Center for Earth Observation (also known as the European Space Research Institute – ESRIN) [7]. SSE aims to provide infrastructure for business-to-business and business-to-client interactions. Its environment is based on hosting and orchestrating the internet services. The main objective was to maximally simplify the processes of service creation and administration. The available SSE tools allow service identification, integration, merging (chaining several services to achieve one more complicated one) with possible usage of both a local and/or an outside provider's data. The creation and definition of services is also simplified by the platform. SSE offers the possibility to integrate various types of Earth Observation and geospatial web services, including product catalogues. The SSE environment supports service prototyping and demonstration processes, allowing the design of automatically executed workflows. This avoids manual replication of the same task, with a valuable decrease in the overall development effort. In this way, SSE streamlines both the time to get the EO data and that needed to deliver the service to the end-user. Users that create, deploy and deliver services based on both local and SSE data and algorithms are called service providers [10].

SSE Portal is a frontend to an SSE platform which aims to provide a standard interface for basic environment functionalities. The main motivation for this portal's creation was to bring an easy-to-use tool to integrate automatic and manual services in an SSE framework. From the point of view of the standard user, available services can be utilized without knowledge of SOAP or XML technologies. From the Service Provider point of view, user-friendly web based graphical interfaces allow service monitoring, management and deployment. Parallel with the SSE Portal, SSE Test Portal exists with the same set of functionalities available. This web page is purposed directly for Service Providers, allowing them to test deployed services before making them available for all users [1, 10].

SSE Portal allows the deployed services to use the WebMap Viewer. This is a tool (i.e., web graphical component) responsible for displaying the world map (alternatively the map of the key area) in most of the services. Service can be created directly through SSE Test Portal, and after the

testing phase can be moved to SSE Portal. The second option is a TOOLBOX that is an SSE tool for managing web services. This environment, installed locally at the Service Provider side, allows the changing of any legacy web services to SOA (Service Oriented Architecture) services. Workflow of the services in the SSE engine can be described using the standard workflow definition language WSDL (Web Service Description Language). Service Provider can create a completely new workflow or use one of the standard workflows provided by the system [10].

It should be noticed that SSE is currently in transition to a new version, due to the work of the ESA Heterogeneous Mission Accessibility program.

TECHNICAL REALIZATION

SafeCity GIS encompasses adaptation and integration of data collected by the HRPT/MetOp satellite station. This data is periodically uploaded on the SafeCity GIS server by the satellite station. The server adapts newly received data for web-GIS. On each new portion of data some analysis algorithms can be run automatically. Another functionality converts and georeferences data written in an HDF format. This is a complex task, because it requires the changing of the geometry of an input image. These adaptation procedures can be supported, by correlative re-reference software. Two modes of the service deployment are implemented in SafeCity GIS. The first mode assumes that SafeCity GIS provides services through the SSE environment. In general, the services deployed in the SSE range from data dissemination to data processing types.

The technical mechanism responsible for the adaptation and processing of the EO data with SSE services is the associated GIS system, as given in the Fig. 2.

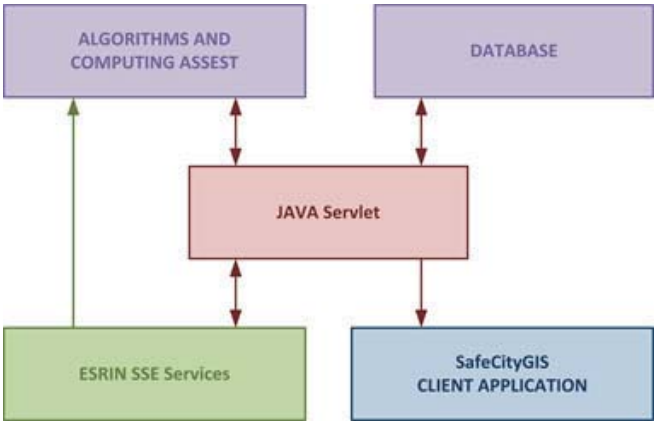

Fig. 2. SSE data processing mechanisms in SafeCity GIS

This mechanism provides a connection between the SSE and GIS layers of the system. It adapts the SSE services to the SafeCity GIS. JAVA Servlet is a transmission layer which provides a connection between the SSE Services data and SafeCity GIS client application. The Servlet communicates with an additional sub-module which helps to compute the required operations. Additionally, JAVA Servlet has a connection to the database in order to correctly process the information gathered by asynchronous SSE services. Results and other data gathered from SSE services may be represented as a spatial-temporal varying layer inside the SafeCity GIS client application (e.g. in the form of a WMS layer deployed on the GeoServer).

The AVHRR SSE service stub developed in GUT under the ESA SafeCity GIS project was already registered and configured on the SSE test Portal. The GUT_AVHRR service is used to make the data publicly available on the Internet.

The technical implementation is presented in Fig. 3. To configure the service properly, the XSLT file (which generates a user interface) and WSDL files of available operation are needed. WSDL files are generated by TOOLBOX Developer Environment. After configuring the service there is a need to configure the TOOLBOX applet on an application server. While the user is using service by SSE Portal, it communicates (using SOAP protocol) with a TOOLBOX server. TOOLBOX server runs XML scripts which are connected to the called service and its operation. XML scripts refer to another JAVA Applet or WebService which provides results for user queries. Then, results are sent back to SSE Portal, and transformed to proper view for the user described in an XSLT file.

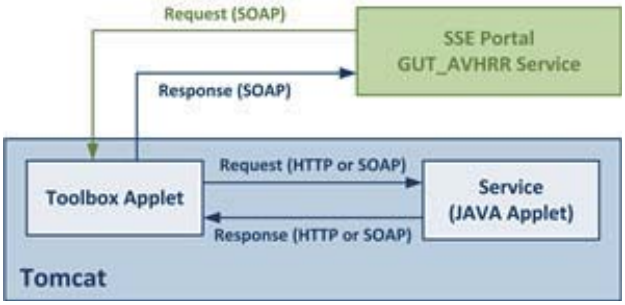

Fig. 3. GUT_AVHRR data dissemination service

DATA DISSEMINATION SERVICES

In this section the technical characterization of different types of services (which are dependent on the data from the satellite ground station) used in SafeCity GIS are described including the algorithms and other details of the services.

Basically, there are two different types of services in the SafeCity GIS which are dependent on the data from the HRPT Satellite Ground Station:

1) Native SafeCity GIS services,

2) Service Support Environment-based service.

In the native system services, the data from the satellite ground station is accessible directly via the SafeCity GIS client application. In this mode of operation, the satellite data is adopted as WMS services. The acquisition workflow in this mode assumes that newly obtained data is transferred to the GIS server (i.e. GeoServer) and deployed in the form of a WMS layer.

The native services provide the results for a SafeCity GIS Web client. These results are obtained by processing the

AVHRR data to get value-added graphical products. The results are available in the form of a Web Map Service (WMS) due to its easy integration with the SafeCity GIS Web clients.

Among the graphical value-added products there are available:

1)AVHRR & HRPT True Color imagery (Fig 4.),
2)Fire detection(Fig. 5),
3) algae monitoring (Fig. 6);

These services differ in their technical details. The first service presents the satellite imagery in the whole extent defined in the system. It combines three selected and radiometrically calibrated bands to form True Color image. The fire detection algorithm processes the whole image and detects fire spots that are further presented in a discrete manner on the map. The algae monitoring service, processes the satellite imagery of the sea in the coastal area and estimates the mean algae bloom probability in the chosen sub-regions of the coast. The first service doesn't distinguish between cloudless and cloudy areas whereas the algae monitoring and fire detection eliminates the cloudy areas from the analysis in the preliminary phase of the process.

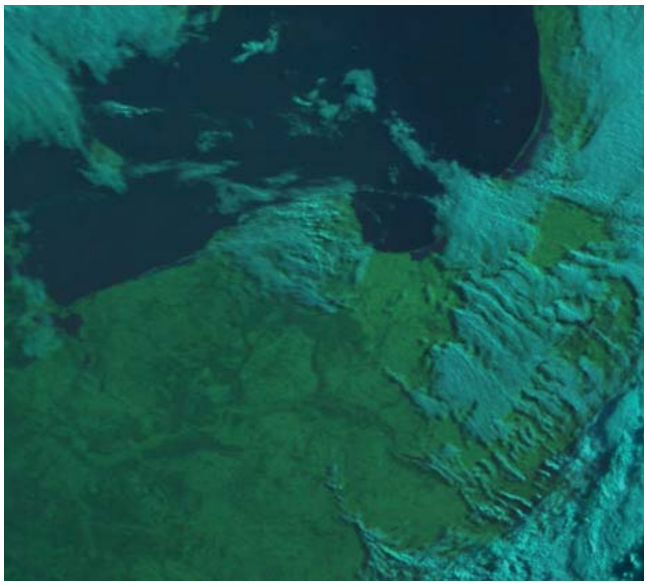

Fig. 4. AVHRR & HRPT True Color imagery sample (September 5, 2014, 2:06PM)

Fig 5. Fire Detection service example, fire icons represent hot spots, which mark areas that have a high probability of fire

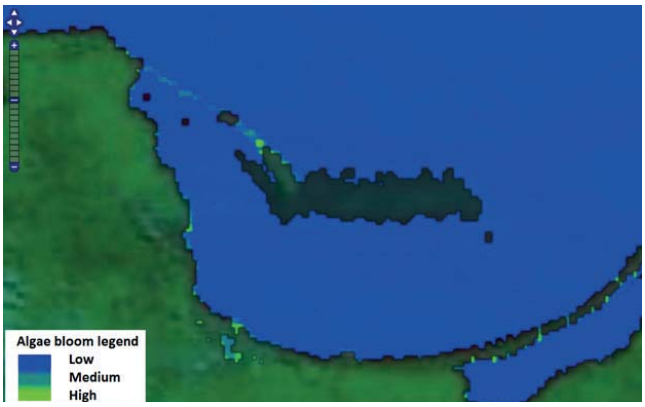

Fig 5. Fire Detection service example, fire icons represent hot spots, which mark areas that have a high probability of fire

The second type of services, devoted to the exploitation of the 1.5m HRPT/MetOp Ground Station, and developed in the SafeCity GIS project are Service Support Environment-based services. In this example, the data for the Satellite Ground station (AVHRR data) is stored and registered in the SSE dissemination type service – GUT_AVHRR. The GUT_AVHRR SSE service stub was already registered and configured on the SSE Test Portal. The GUT_AVHRR service is used to make the data publicly available on the Internet.

The Service deployed in the SSE Portal provides both raw and calibrated data from the AVHRR sensor onboard the meteorological satellites (NOAA-15 – NOAA-19, MetOp-A and MetOp-B). The acquired data is geometrically and radiometrically calibrated and provided in the form of GeoTiff and possibly HDF file formats. The service provides newly obtained data (not historical) from May 2013. Great effort is put in to provide the data as fast as possible after the observation. For the SSE Portal users the service immediately exposes the WebMapViewer (also known as Area of Interest Tool or AOI) component as a Graphical User Interface (GUI). For this purpose the configuration of the WebMapViewer component is done within the SSE Portal as seen in Fig. 7. The prepared configuration is used in the Graphical User Interface of the deployed service (i.e., seen by a user of the SSE Portal).

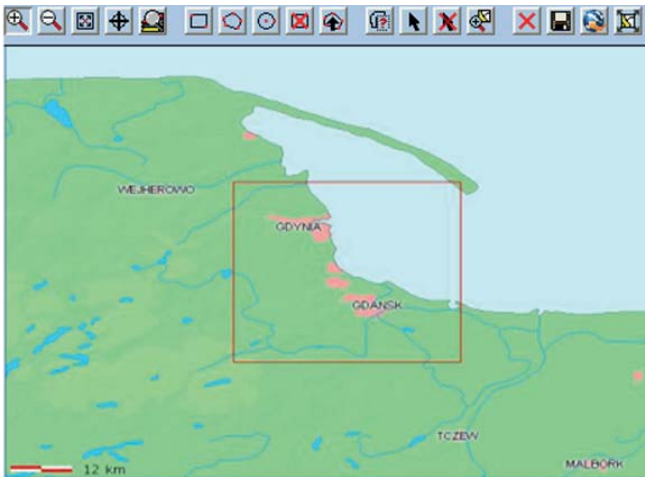

Figure 7. Configuration of the WebMapViewer component during the service deployment on the SSE Portal

The data dissemination service being implemented and deployed in the SSE is the Advanced Very High Resolution Radiometer (AVHRR) data catalogue. The catalogue will allow the user to download earth observation (EO) satellite data received with the 1.5m HRPT/MetOp satellite ground station. In the AVHRR data catalogue service the data is provided to the user for any pre-requested location in the area of Poland and the Southern Baltic.

The AVHRR data catalogue service may be used as a source of the input data to any models and simulations developed in the case of a specific need. Since the AVHRR data catalogue service provides the data in a nearly real-time manner, these specific models and simulations may also assume such a requirement. The AVHRR data catalogue allows one to download statically served satellite data. This data is available via FTP.

The services provide the complete set of data from the AVHRR sensor (raw measurements, calibrated measurements and additional information i.e., solar zenith angle, satellite inclination, nadir to pixel angle). Analogical to the native services, Fire detection (based on hot spots) and AVHRR True Color imagery services are available.

Detection of fires implementation is based on the hot spot detection procedure [3, 6] The hot spots are detected in the AVHRR data based on the computed brightness temperature (BT) values. The brightness temperatures are derived from three near-infrared channels. The idea for the fire detection by identification of hot spots, is that fires result in large discrepancies in the brightness temperatures i.e. the areas of fire have a higher BT than the surrounding regions. The brightness temperature is derived from a single channel as a calibrated value. The computation of brightness temperature uses the calibration coefficient disseminated with the AVHRR data. Current work aims to improve the algorithm of the hot spots detection. New methods of classification are being tested, including tests performed on new data sets (real fires) for the territory of Poland received by the satellite ground station.

Detected hot spots are marked on the AVHRR True Color imagery with suggestive markers stitched on to the detected hot spot location. Alternatively, hot spots are accessible as a separate data source (without the imagery). The second data type would be convenient for thematic composition with different layers of spatial data.

In the AVHRR True Color composition the bands 1,4,5, are used. They are separately assigned to colour components in the Red, Green, Blue model (RGB). Due to the spectral characteristic of AVHRR bands, the assignment is as follows: 1-red, 4- green, 5-blue. The Radiometric resolution of a single AVHRR band has 10 bits whereas the colour component has only an 8 bit resolution. Therefore, the next step is histogram equalization. The minimal and maximal values of each band are evaluated, and the spectral range is equally distributed to the 8-bit scores colour component values [5].

Algae monitoring service provides information about the possibility of algae presence Fig. 6 presents the coast of Gdańsk with an algae-monitoring layer. Red color shows areas with a high possibility of algae presence, green Grey – a low possibility, while grey is reserved for areas in which the meteorological situation did not allow the evaluation of the possibility.

Additional services are planned to be deployed. Amongst them are: explosion effect, chemical pollution and flooding simulations. The explosion and chemical pollution simulations will allow the user to simulate which areas will be affected by the threat. The result would include spatial features in the form of polygons with additional information concerning the affected regions. Flood simulation will be used to determine the size of the area awash. This simulation model will use a Digital Terrain Model (DTM) and data related to the soil, and ground properties. Service results include information on the flooded area. Explosion and chemical pollution simulations will produce vector data, which can be served as a shape file or in GML form dynamically via FTP. On the other hand, the results from the flood simulation model – as being more complex – will be presented in raster form. The output will contain information concerning the water level altitudes for the gridded area.

CONCLUSIONS

During the development of data dissemination services for EO data obtained by the HRPT-MetOp ground satellite station and accompanying GIS system, various issues connected with the development of web services were faced and resolved.

Service Support Environment is an easy-to-use tool which can be included in vast GIS environments with minimal effort. Tools provided with the platform incorporate widely used technologies and programming languages, which accelerates the process of merging the SSE and native platforms.

Dissemination of data through web services is made easy with SSE. Due to open distribution of this environment, services are easily accessible and available for geospatial society. Since the SSE is accessible through the ESA's web-pages, and is connected with their other services, the number of data receivers is expected to increase. Shared data and functionality can be used by other systems, which affects the lower cost of this developed solution.

Due to integration with SSE, the operationability of the system substantially increased, especially in the context of data dissemination capabilities. Aforementioned advantages of the SSE platform were taken into consideration, leading to the conclusion that choosing the ESA's SSE for services management is a plausible option.

The spatial data awareness tends to be more and more important in the maritime applications. As an example, the maritime administration (MA). Nowadays in Poland, there are approximately 20 different spatial data sets which are in competences of MA. Most of them are related to the sea, and some of them are related to the land. Examples of sea-related, are hazardous areas for boating and fishing (with the deadlines for the recognition of a dangerous zone), established flow routes, sea routes or the axes of submarine cables and pipelines. Those related to the ground are designated by boundaries of the coastal belt (technical belt and protective belt). Coastal belt is an area of land adjacent to the sea shore. The coastal belt includes the technical belt - which is an area of mutual direct impact of sea and land and requires very high environmental protection, and the protective belt which

covers an area in which human activities have a direct impact on the technical belt.

The synergy from the combination of the "native" spatial data of MA and other sources of spatial data, may be considered as substantial. For example, using real-time satellite observation in the hazardous areas for boating and fishing, or technical best, may help to improve safety and improve decision time in crucial situations. In such a context, usage of the open standards for spatial data dissemination which were applied in the presented system makes the services (and in general our approach) compliant and ready to serve as complementary in maritime applications, including supporting processes in maritime administration.

ACKNOWLEDGEMENT

This work was sponsored by the European Space Agency under the PECS Project, ESTEC/Contract No. 4000105693/12/NL/KML

REFERENCES

1. Final report on the ESA PECS Project implementation, ESTEC/Contract No. 4000105693/12/NL/KML, Development, testing, demonstration and dissemination of innovative Web-based Geographical Information System for threat monitoring, prediction, and risk analysis for the municipal area - Safe City GIS, 2014

2. High Performance Computing in Remote Sensing, Plaza, A. J.; Chang, Ch. Publisher: Chapman & Hall/CRC Computer & Information Science Series, ISBN: 978-1584886624

3. Lee T. M., Tag P. M.: Improved detection of hotspots using the AVHRR 3.7 μm channel, Bulletin of The American Metrological Society 1990, 71, pp. 1722–1730

4. Markiewicz Ł., Chybicki A., Drypczewski K., Bruniecki K., Dąbrowski J.: Operational Enhancement of Numerical Weather Prediction with Data from Real-time Satellite Images In: Marine Navigation and Safety of Sea Transportation: Navigational Problems.-,2013,s.217-221

5. Moszyński M., Kulawiak M., Chybicki A., Łubniewski Z., Bruniecki K., Bieliński T., Stepnowski A.: Innovative Web-based Geographic Information System for Municipal Areas and Coastal Zone Security and Threat Monitoring Using EO Satellite Data, Marine Geodesy, Vol. 38 No. 3, 2015, pp. 203-224

6. Pu R., Gong P., Li Z.: Scarborough, J. A dynamic algorithm for wildfire mapping with NOAA/AVHRR data, International Journal of Wildland Fire 2004, 13(3), 275-285

7. Service Support Environment Experiment Excellence. URL http://services.eoportal.org/massRef/documentation/SSE-Brochure.pdf (accessed on: 20 02 2015)

8. Technical specifications and details of the Dartcom Windows™ HRPT/CHRPT/MetOp data reception and processing ground station. URL ftp://ftp.dartcom.co.uk/pub/COMS-1/HRPT-CHRPT-AHRPT%201.5m%203rd%20Generation%20V12.pdf (accessed 17 01 2014)

9. Web Services Glossary. URL http://www.w3.org/TR/2004/NOTE-ws-gloss-20040211/#webservice (accessed on: 28 02 2015)

10. Workshop materials of the 2013 SSE Service Providers Training ESA – ESRIN, Frascati, Italy, 18-19 April 2013, Research Service Support (RSS) team, unpublished report

11. Wu A., Xiong X., Angal A.: Derive a MODIS-Based Calibration for the AVHRR Reflective Solar Channels of the NOAA KLM Operational Satellites. Geoscience and Remote Sensing, IEEE Transactions on , vol.51, no.3, 2013, pp.1405-1413,

12. Zhua A. X., Hudson B., Burt J., Lubich K., Simonsond D.: Soil Mapping Using GIS, Expert Knowledge, and Fuzzy Logic. Soil Science Soc. of Am. Jour 2001, Vol. 65 No. 5, pp. 1463-1472

13. Dąbrowski, J., Kulawiak, M., Moszyński, M., Bruniecki, K., Kamiński, Ł., Chybicki, A., & Stepnowski, A. (2009). Real-time web-based GIS for analysis, visualization and integration of marine environment data. In Information Fusion and Geographic Information Systems (pp. 277-288). Springer Berlin Heidelberg.

14. Kulawiak, M., Chybicki, A., & Moszynski, M. (2010). Web-based GIS as a tool for supporting marine research. Marine Geodesy, 33(2-3), 135-153.

15. 15. Moszynski, M., Chybicki, A., Kulawiak, M., & Lubniewski, Z. (2013). A novel method for archiving multibeam sonar data with emphasis on efficient record size reduction and storage. Polish Maritime Research, 20(1), 77-86.

16. Janowski, A., Jurkowska, A., Lewczuk, D., Szulwic, J., & Zaradny, A. (2014). Assessment of cliff stability after the demolition of the engineering facilities. InConference Proceedings of SGEM: Multidisciplinary Scientific Conferences. Albena, Bulgaria.

CONTACT WITH AUTHOR

K. Drypczewski
kszyk@eti.pg.gda.pl

A. Stepnowski
astep@eti.pg.gda.pl

K. Bruniecki
krzysztof.bruniecki@eti.pg.gda.pl

POLISH MARITIME RESEARCH 4(88) 2015 Vol. 22; pp. 27-33
10.1515/pomr-2015-0067

SENSITIVITY OF THE GAME CONTROL OF SHIP IN COLLISION SITUATIONS

Józef Lisowski, Prof.
Gdynia Maritime University, Poland

ABSTRACT

The paper introduces the application of the theory of deterministic sensitivity control systems for sensitivity analysis taking place in game control systems of moving objects, such as ships. The sensitivity of parametric model of game ship control process and game control in collision situations - sensitivity to changes in its parameters have been presented. First-order and k-th order sensitivity functions of parametric model of the process and game control are described. The structure of the game ship control system in collision situations and the mathematical model of game control process in the form of state equations are given. Characteristics of sensitivity functions of the model and game ship control process on the base of computer simulation in Matlab/Simulink software have been presented. At the end are given proposals regarding the use of sensitivity analysis to practical synthesis of computer-aided system navigator in potential collision situations.

Keywords: marine transport; safety of navigation, game control, sensitivity analysis; computer simulation

INTRODUCTION

One of the most important problems arising in design of a control system consists in predicting its probable properties. The main method of such prediction is the use of physical and mathematical models. A sufficiently complete mathematical model of a system must reflect its basic properties, including possible dependence on parameters ; it will be called parametric model of the system. A determining set of parameters is called complete if it uniquely determines all state variables of the model under investigation [1,7,8,13].

By sensitivity of control systems one usually means dependence of their properties on variation of parameters. Sensitivity theory became an independent scientific branch of cybernetics and control theory in the sixties. In major part this was connected with quick development of self-tuning systems that were constructed for effective operation under parametric disturbances [10,12,26].

Lately, sensitivity theory methods were widely used for solving various theoretical and applied problems dealing with analysis and synthesis, identification, adjustment, monitoring, testing, tolerance distribution [16,18,19,29,30].

At the same , distinction is made between the sensitivity of the model control process for changing its parameters and process optimal control sensitivity to changes in its parameters and disturbance influence [23,25,27].

The previous papers dealing with sensitivity of deterministic systems did not concern game systems [22,31].

At sea, land and air transport processes both own object and many encountered objects are involved. Control of such processes, due to the high proportion of human subjectivity in the decision-making manoeuvre, often takes the character of game control [2,3,17,20].

SENSITIVITY FUNCTIONS OF CONTROL SYSTEMS

The ship game control process as a MIMO process is described by: state equation (1), constraints of state and control (2) and quality control index (3).

$$\dot{\boldsymbol{x}}(t) = \mathbf{f}[\mathbf{x}(\mathrm{t}), \mathbf{u}(\mathrm{t}), \mathrm{t}] \tag{1}$$

$$\boldsymbol{g}[\boldsymbol{x}(t), \boldsymbol{u}(t), t] \leq 0 \tag{2}$$

$$\boldsymbol{I} = \int_{t_o}^{t_K} \boldsymbol{f_o}[\boldsymbol{x}(t), \boldsymbol{u}(t), t]dt \tag{3}$$

where:
x(t) – state variable,
u(t) – control variable,
t – time.

The simplest method of sensitivity analysis consists in numerical investigation of system parametric model over the whole range of variation of the determining set of parameters [31].

The main investigation method in sensitivity theory consists in using so called sensitivity functions.

Let $a_1, ..., a_m$ be a set of parameters constituting a complete set a.

Moreover, let function of state variables $F[x_i(t, a)]$ $(i=1, ..., n)$ and quality index control I be single valued functions of control variable u_k [25].

The following partial derivatives:

$$s_a^{pm} = \frac{\partial F[x(t,\ a)]}{\partial a} \tag{4}$$

$$s_x^{oc} = \frac{\partial I[x(u)]}{\partial x} \tag{5}$$

are called first-order sensitivity functions of the parametric process model s_a^{pm} and sensitivity functions of optimal control of the process s_x^{oc}. In automatic control literature first-order sensitivity functions are often called simply "sensitivity functions" [25].

Theoretically, we can also consider features of the sensitivity functions k-th order of parametric model $s_{k,a}^{pm}$ and sensitivity functions of optimal control $s_{k,x}^{oc}$ in the following form:

$$s_{k,a}^{pm} = \frac{\partial^k F[x(t,a)]}{\partial a_1^{k_1} ... \partial a_m^{k_m}}$$
$$k_1 + ... + k_m = k \tag{6}$$

$$s_{k,x}^{oc} = \frac{\partial^k I[x(u)]}{\partial x_1^{k_1} ... \partial x_n^{k_m}}$$
$$k_1 + ... + k_m = k \tag{7}$$

GAME SHIP CONTROL SYSTEM

The structure of the game control system of own ship in collisions situations at sea is presented in Fig. 1.

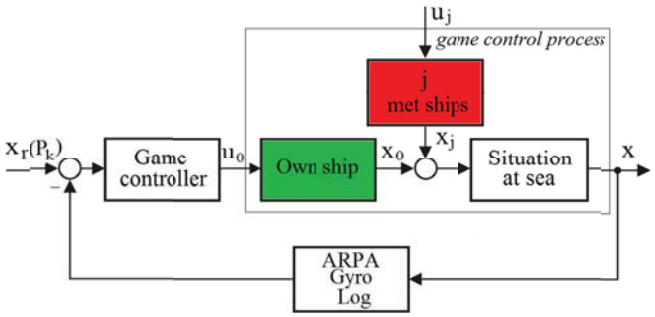

Fig. 1. The structure of game ship control system in collision situations: $\mathbf{x}_r(P_k)$ – reference trajectory of own ship to the closest point of return P_k, $\mathbf{u}_0$ – control of own ship, $\mathbf{u}_j$ – control of j-th met ship, $\mathbf{x}_0$ – state variables of own ship, $\mathbf{x}_j$ – state variables of j-th met ship, $\mathbf{x}$ – state variables of game control process

The current state of the control process is determined by the co-ordinates of the own ship's position and the positions of the encountered j ships (Fig. 2):

$$x_0 = (X_0, Y_0) \tag{8}$$

$$x_j = (X_j, Y_j)$$
$$j = 1, 2, ..., m \tag{9}$$

The system generates its control at the moment t_k on the basis of data received from the ARPA anti-collision system pertaining to the positions of the encountered ships:

$$x(t_k) = \begin{bmatrix} x_0(t_k) \\ x_j(t_k) \end{bmatrix} \quad j = 1,\ 2,..., m \qquad k = 1, 2,..., K \tag{10}$$

The constraints for the state co-ordinates:

$$\{\ x_0(t), x_{ji}(t)\ \} \in P \tag{11}$$

are navigational constraints, while control constraints:

$$u_0 \in U_0,\ u_j \in U_j \quad j = 1, 2,..., m \tag{12}$$

take into consideration: the ships' movement kinematics, recommendations of the COLREG Rules and the condition to maintain a safe passing distance Ds satisfying the relationship:

$$D_{\min}^j = \min D_j(t) \geq D_s \tag{13}$$

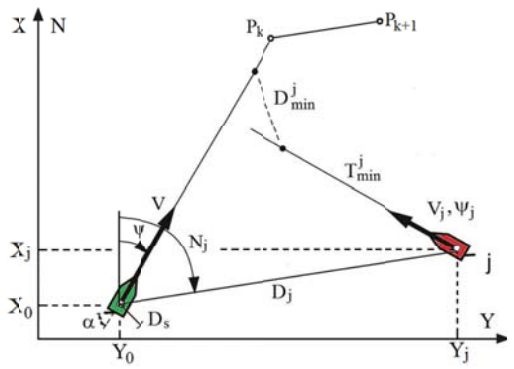

Fig. 2. Situation of relative motion of own ship and j-th met ship:V, ψ speed and course of own ship, a rudder angle of own ship, D_s – safe distance, N_j,D_j – bearing and distance to j-th ship, V_j,ψ_j- speed and course of j-th ship, $D^j_{\min}$, $T^j_{\min}$ - min. approach distance and time of the own ship to j-th ship

GAME SHIP CONTROL PROCESS MODEL

Taking into consideration the equations of the own ship hydromechanics and equations of the own ship relative movement to the j-th encountered ship, the state process equations take the following form:

$$\left.\begin{aligned}
\dot{x}_1 &= x_2 \\
\dot{x}_2 &= a_1 x_2 x_3 + a_2 x_3 |x_3| x_4 + a_3 x_3 |x_3| u_1 \\
\dot{x}_3 &= a_4 x_3 |x_3| \|x_4| x_4 + a_5 x_3 |x_3| x_4^2 + a_6 x_2 x_3 x_4 |x_4| + \\
&\quad + a_7 x_2 x_3 x_4 |x_4| + a_8 x_3 |x_3| + a_9 x_5 |x_5| x_6 + a_{10} x_3 |x_3| x_4 u_1 \\
\dot{x}_4 &= a_4 x_3 x_4 + a_5 x_3 x_4 |x_4| + a_6 x_2 x_4 + a_{11} x_2 + a_{10} x_3 u_1 \\
\dot{x}_5 &= a_{12} x_5 + a_{13} u_2 \\
\dot{x}_6 &= a_{14} x_6 + a_{15} u_3 \\
\dot{x}_{6+j} &= -x_3 + x_{7+j} x_2 + x_{9+j} \cos x_{8+j} \\
\dot{x}_{7+j} &= -x_2 x_{6+j} + x_{9+j} \sin x_{8+j} \\
\dot{x}_{8+j} &= a_{15+j} x_2 x_{9+j} u_{j1} \\
\dot{x}_{9+j} &= a_{16+j} x_{8+j} |x_{8+j}| + a_{17+j} u_{j2}
\end{aligned}\right\} \quad (14)$$

The state variables are represented by the following values:

$x_1 = \psi$ - course of the own ship,

$x_2 = \dot{\psi}$ - angular turning speed of the own ship,

$x_3 = V$ - speed of the own ship,

$x_4 = \beta$ - drift angle of the own ship,

$x_5 = n$ - rotational speed of the screw propeller of own ship,

$x_6 = H$ - pitch of the adjustable propeller of the own ship,

$x_{6+j} = X_j$ - x coordinate of the *j*-th ship position,

$x_{7+j} = Y_j$ - y coordinate of the *j*-th ship position,

$x_{8+j} = N_j$ - bearing of the *j*-th ship or Q_j – relative meeting angle,

$x_{9+j} = D_j$ - distance to *j*-th ship.

While the control values are represented by:

$u_1 = \alpha_r$ - reference rudder angle of the own ship,

$u_2 = n_r$ - reference rotational speed of the own ship's screw propeller,

$u_3 = H_r$ - reference pitch of the adjustable propeller of the own ship,

$u_{j1} = \psi_j$ - course of the *j*-th ship,

$u_{j2} = V_j$ - speed of the *j*-th ship [11].

SENSITIVITY FUNCTION OF GAME SHIP CONTROL PROCESS MODEL

As a function of state process variables $F[x(t,a)]$ is assumed the risk of collision r_j in the following form:

$$r_j(x) = \left\{ w_1 \left[\frac{D^j_{\min}(x)}{D_s} \right]^2 + w_2 \left[\frac{T^j_{\min}(x)}{T_s} \right] \right\}^{-\frac{1}{2}} \quad (15)$$

where:

w_1, w_2 – weight coefficients depending on the visibility at sea and dynamic length and breadth of the met *j*-th ship [4,5,6].

The sensitivity function according to (4) can be represented as:

$$s^{pm}_{a_i} = \frac{\partial F[x(t,\ a)]}{\partial a_i} = \frac{\partial r_j[x(t, a_i)]}{\partial a_i} = s^{a_i}_r \quad (16)$$

As a measure of safe control process model sensitivity to changes of process parameters it is taken a relative change of risk collision r_j caused due to deviation of the coefficient a_i in state equations by ∂a_i .

The coefficients of state equations of model process have been varied within $\pm 10\%$ from their rated value ai and each time the anti-collision manoeuvre was simulated in Matlab/Simulink software, then relative change of risk collision was calculated by using the formula (15). As a result of computer simulation investigations there were obtained the characteristics of sensitivity functions $s^{a_i}_r$ at w_1=2 and w_2=1 weight coefficients (Fig. 3), were obtained.

In Figure 4 there are additionally shown sensitivity functions of the risk collision for different values w_1 and w_2 of weight coefficients, are shown additionally

By setting different values of weight coefficients can be made multi-criteria optimization of ship safe trajectory in collision situations, taking into account the compromise between distance and time of excessive rapprochement of ships [9,14,15,21,28].

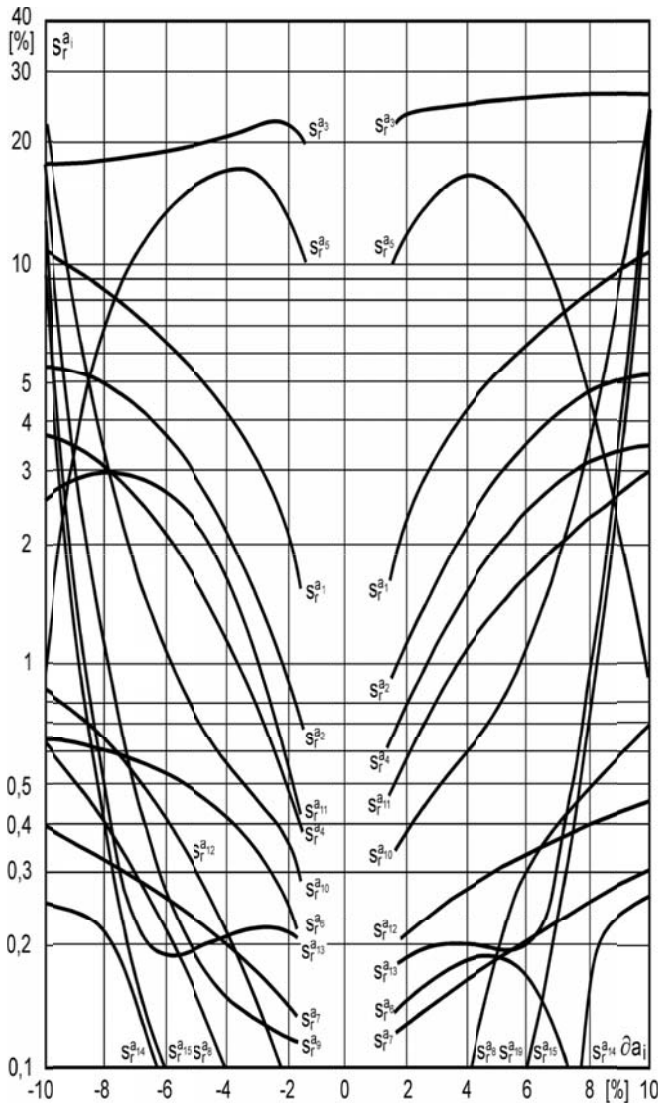

Fig. 3. Sensitivity functions of the risk of collision to the changes of state equations coefficients process model of situation motion of own ship and j-th met ship for weight coefficients w_1=2 and w_2=1

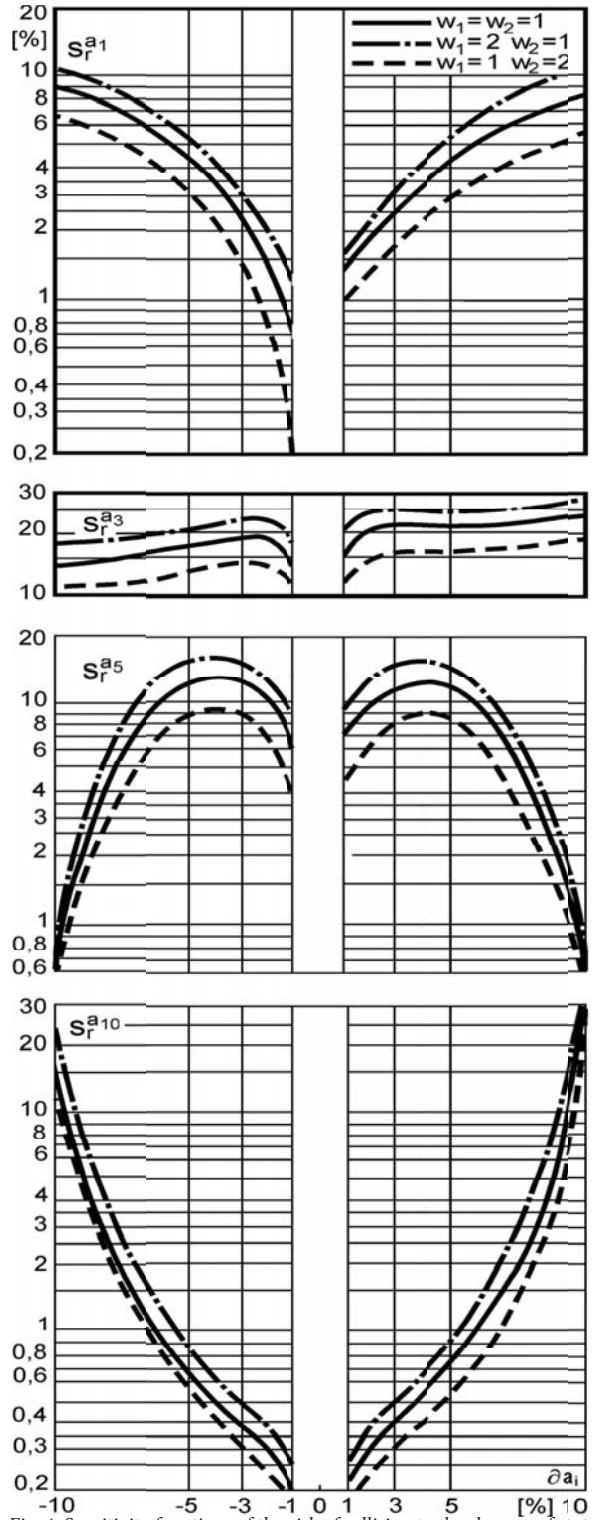

Fig. 4. Sensitivity functions of the risk of collision to the changes of state equations coefficients process model of situation motion of own ship and j-th met ship for different values of weight coefficients

SENSITIVITY FUNCTION OF OPTIMAL AND GAME SHIP CONTROL IN COLLISION SITUATIONS

Sensitivity function of game control based on the equation (5) take the following form:

$$s_i^{gc} = \frac{\partial I_{0,\bar{j}}\left[x_i(u,p)\right]}{\partial x_i} \tag{17}$$

The quality game control index $I_{0,j}$ takes the form of game payment, consisting of integral payments and final payment:

$$I_{0,j} = \int_{t_0}^{t_{Pk}} \left[x_j(t)\right]^2 + r_j(t_{Pk}) + D(t_{Pk}) \tag{18}$$

The integral payment represents loss of way by the ship while passing the encountered ships and the final payment determine the final risk of collision rj(tPk) relative to the *j*-th ship and the final deviation of the own ship trajectory $D(t_{Pk})$ from the reference trajectory.

The investigation of sensitivity of the game control is applied to sensitivity analysis of the final payment $D(t_{Pk})$:

$$s_i^{gc} = \frac{\partial D(t_{Pk})}{\partial x_i} \tag{19}$$

Taking into consideration the practical application of the game control algorithm for the own ship in a collision situation it is recommended to perform the analysis of sensitivity of a safe control with regard to the accuracy degree of the information received from the anti-collision ARPA radar system in the current approach situation, from one side and also with regard to the changes in kinematical and dynamic parameters of the control process from the other side.

Admissible average errors, that can be contributed by sensors of the anti-collision system can have the following values for:

- for radar,
  - » bearing: ±0,22 deg,
  - » form of cluster: ±0,05 deg,
  - » form of impulse: ±20 m,
  - » margin of antenna drive: ±0,5 deg,
  - » sampling of bearing: ±0,01 deg,
  - » sampling of distance: ±0,01 nm,
- for gyrocompas: ±0,5 deg,
- for log: ±0,5 kn,
- for GPS: ±15 m.

The algebraic sum of all errors affecting the proper display of navigational situation, must not exceed ± 5% or ± 3 deg.

SENSITIVITY OF OPTIMAL AND GAME SHIP CONTROL TO INACCURACY OF INFORMATION FROM ARPA ANTI-COLLISION SYSTEM

Let *SC* represents such a set of state and control variables of game process information on the navigational situation that:

$$SC\{x_1,\ x_3,\ x_{8+j},\ x_{9+j},\ u_{j1},\ u_{j2}\} \tag{20}$$

Let then SCARPA represent a set of information from ARPA system containing errors of measurement and processing parameters:

$$SC_{ARPA}\{x_1 \pm \partial x_1, x_3 \pm \partial x_3, x_{8+j} \pm \delta x_{8+j}, x_{9+j} \pm \partial x_{9+j}, u_{j1} \pm \partial u_{j1}, u_{j2} \pm \partial u_{j2}\} \tag{21}$$

Relative measure of sensitivity function of the final payment in the game s_{i1} as a final deviation of the ship's safe trajectory D_{Pk} from the reference trajectory will be:

$$s_{i1}^{gc} = \{s_1, s_3, s_{8+j}, s_{9+j}, s_{j1}, s_{j2}\} \tag{22}$$

SENSITIVITY OF OPTIMAL AND GAME SHIP CONTROL TO PROCESS PARAMETERS ALTERATIONS

Let *SP* represents a set of parameters of the state process control:

$$SP\{p_1,\ p_2,\ p_2,\ p_3,\ p_4\} \tag{23}$$

where:

$p_1=t_m$ – advance time of manoeuvre with respect to the dynamic properties of own ship,

$p_2=D_s$ – safe distance, in good visibility D_s=0,1 ÷ 1,0 *nm*, in restricted visibility D_s=1,0 ÷ 3,0 *nm*,

$p_3=t_k$, - duration of one stage of ships trajectory,

$p_4=\Delta V$ – reduction of own ship speed for a deflection from course greater than 30 deg.

Let then SP_1 represent a set of information containing errors of measurement and processing parameters:

$$SP_1\{p_1 \pm \partial p_1, p_2 \pm \partial p_2, p_3 \pm \partial p_3, p_4 \pm p_4\} \tag{24}$$

Relative measure of sensitivity of the final payment in the game si2 as a final deflection of the ship's safe trajectory DPk from the reference trajectory will be:

$$s_{i2}^{gc} = \{s_{p1}, s_{p2}, s_{p3}, s_{p4}\} \tag{25}$$

SENSITIVITY CHARACTERISTICS OF SAFE SHIP CONTROL IN GOOD VISIBILITY AT SEA

Computer simulation of the multi-step non-cooperative matrix game algorithm, as a computer software supporting the navigator manoeuvring decision, was carried out in Matlab/Simulink software on an example of the real navigational situation of passing j = 18 encountered ships in good visibility at sea, when D_s=0,5 *nm* (Fig. 5 and 6).

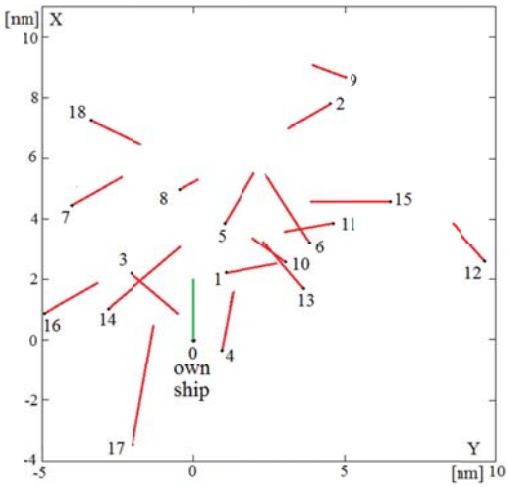

Fig. 5. The 24 minute speed vectors of the own ship and j=18 met ships

The situation was recorded in the Skagerrak Strait on board r/v HORYZONT II, a research and training vessel of the Gdynia Maritime University, on the radar screen of the ARPA anti-collision system Raytheon.

Sensitivity characteristics were determined for the alterations of values ∂x and ∂p within ±5% or ±3 deg (Fig. 7).

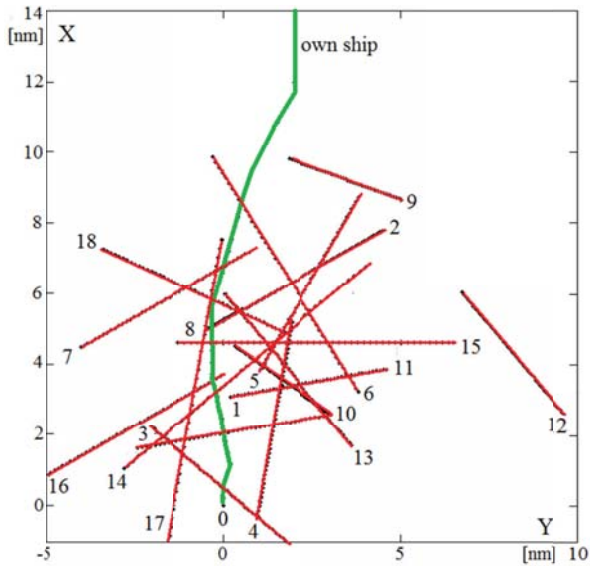

Fig. 6. The safe trajectory of the own ship for the multi-step non-cooperative matrix game algorithm in good visibility Ds=0,5 nm in situation of passing j=18 met ships, r(tk)=0, DPk=2,12 nm

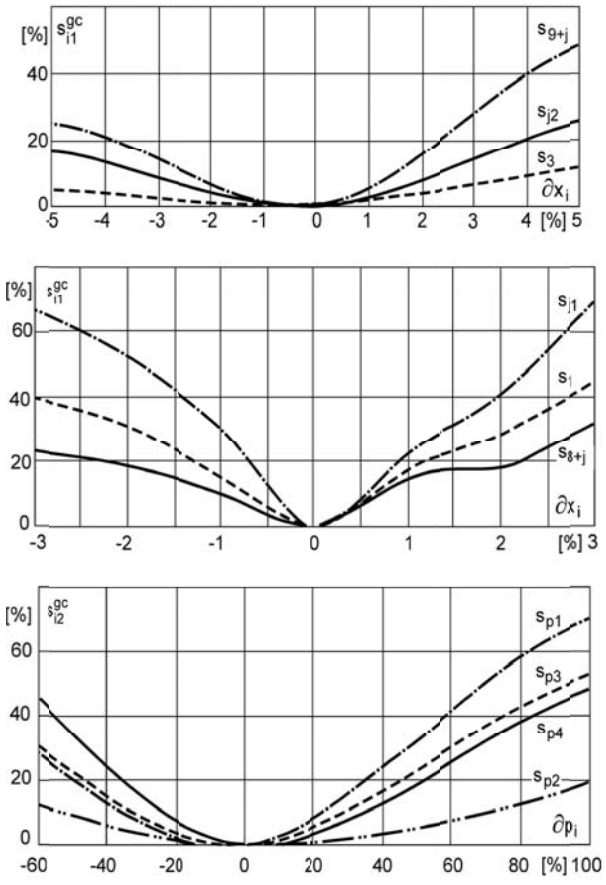

Fig. 7. Sensitivity characteristics of the game control of own ship according to the multi-step non-cooperative matrix game algorithm on an example of the navigational situation j = 18 occuring in the Skagerrak Strait

CONCLUSIONS

Analysis of the results of calculations of the sensitivity function allows to draw the following conclusions:

- in the range of sensitivity function of game ship control process model:
  - » the model process sensitivity to changes of individual coefficients of the state equations varies from 0,01% to 25%,
  - » the highest sensitivity is shown by the coefficients: a_1, a_3, a_5 and a_{15}, the lowest one by the coefficients: a_6, a_8, a_{12} and a_{14},
  - » the highest changes of sensitivity, so called second order sensitivity, have occurred for coefficients: a_9, a_{10}, a_{13} and a_{15},
  - » a greater impact on the model sensitivity is to change the weight coefficient w_1 in contrast to that of w_2,
- in the range of sensitivity function of game ship control in collision situation, considered as the sensitivity of the final game payment:
  - » it is the least for changes of the changes of safe distance and for level of reduction of own ship speed,
  - » it is the greatest for changes of the distance to *j*-th ship and changes of the course of *j*-th ship,
  - » it grows with the degree of the ships cooperation for the purpose of avoiding of collision,
  - » it grows with the number of meeting ships and with the quantity of admissible strategies for own ship and passing ships.

The sensitivity functions obtained as a result of computer simulation investigations define the requirements regarding range and accuracy of ship kinematics and dynamics identification for the model useful for the safe control system synthesis.

The future investigations should be directed to obtain further simplification of the process models taking into account their sensitivity functions.

BIBLIOGRAPHY

1. Astrom K.J.: *Model uncertainty and robust control*. Lecture notes on iterative identification and control design. Lund Institut of Technology, Sweden 2000, pp. 63-100.

2. Baba N., Jain L.C.: *Computational intelligence in games*. Physica-Verlag, New York 2001.

3. Basar T., Olsder G.J.: *Dynamic non-cooperative game theory*. Siam, Philadelphia 2013.

4. Bist D.S.: *Safety and security at sea*. Butterworth Heinemann, Oxford-New Delhi 2000.

5. Bole A., Dineley B., Wall A.: *Radar and ARPA manual*. Elsevier, Amsterdam-Tokyo 2006.

6. Cahill R.A.: *Collisions and their causes*. The Nautical Institute, London 2002.

7. Cruz J.B.: *Feedback systems*. Mc Graw-Hill Book Company, New York 1972.

8. Dorf R.C., Bishop R.H.: *Modern control systems*. Addison-Wesley, California 1998.

9. Engwerda J.C.: *LQ dynamic optimization and differential games*. John Wiley and Sons, West Sussex 2005.

10. Eslami M.: *Theory of sensitivity in dynamic systems*. Springer-Verlag, Berlin 1994.

11. Fossen T.I.: *Marine craft hydrodynamics and motion control*. Wiley, Trondheim 2011.

12. Fujarewicz K.: *Structural sensitivity analysis of systems with delay* (in Polish). XVIII Krajowa Konferencja Procesów Dyskretnych, Zakopane 2014.

13. Gierusz W., Lebkowski A.: *The researching ship "Gdynia"*, Polish Maritime Research, Vol. 19, No. 74, 2012, pp. 11-18.

14. Gluver H., Olsen D.: *Ship collision analysis*. Balkema, Rotterdam 1998.

15. Isaacs R.: *Differential games*. John Wiley and Sons, New York 1965.

16. Lazarowska A.: *Safe ship control method with the use of ant colony optimization*. Solid State Phenomena, Vol. 210, 2014, pp. 95–101.

17. Lisowski J.: *Comparison of dynamic games in application to safe ship control*. Polish Maritime Research, Vol. 21, No. 3, 2014, pp. 3-12.

18. Miller A., Rybczak M.: *Model predictive control algorithm verification with the use of real time xPC target platform*. Joint Proceedings, No. 84, 2014, pp. 73-84.

19. Mohamed-Seghir M.: *The branch-and-bound method, genetic algorithm, and dynamic programming to determine a safe ship trajectory in fuzzy environment*. 18th International Conference in Knowledge Based and Intelligent Information and Engineering Systems. Procedia Computer Science, No. 35, 2014, pp. 634-643.

20. Modarres M.: *Risk analysis in engineering*. Taylor and Francis Group, Boca Raton 2006.

21. Nisan N., Roughgarden T., Tardos E., Vazirani V.V.: *Algorithmic game theory*. Cambridge University Press, New York 2007, p. 717-733.

22. Nise N.S.: *Control systems engineering*. John Wiley and Sons, New York 2015.

23. Nise N.S.: *Control systems engineering*. Wiley, California 2015.

24. Osborne M.J.: *An introduction to game theory*. Oxford University Press, New York 2004.

25. Rosenwasser E., Yusupov R.: *Sensitivity of automatic control systems*. CRC Press, Boca Raton 2000.

26. Sanchez-Pena R.S., Sznaier M.: *Robust systems theory and applications*. Wiley, New York 1998.

27. Skogestad S., Postlethwaite I.: *Multivariable feedback control*. Wiley, Chichester 2005.

28. Straffin P.D.: *Game theory and strategy* (in Polish). Scholar, Warszawa 2001.

29. Szlapczynski R.: *Evolutionary sets of safe ship trajectories with speed reduction manoeuvres within traffic separation schemes*. Polish Maritime Research, Vol. 81, No 1, 2014, pp. 20-27.

30. Tomera M.: *Dynamic positioning system for a ship on harbour manoeuvring with different observers. Experimental results*. Polish Maritime Research, Vol. 83, No. 3, 2014, pp. 13-21.

31. Wierzbicki A.: *Models and sensitivity of control systems* (in Polish). WNT, Warszawa 1977.

CONTACT WITH THE AUTHOR

Józef Lisowski

Department of Ship Automation
Faculty of Electrical Engineering
Gdynia Maritime University
83 Morska St.
81-225 Gdynia
Poland

POLISH MARITIME RESEARCH 4(88) 2015 Vol. 22; pp. 34-40
10.1515/pomr-2015-0068

SWARM INTELLIGENCE APPROACH TO SAFE SHIP CONTROL

Agnieszka Lazarowska
Gdynia Maritime University, Poland

ABSTRACT

This paper presents an application of the Ant Colony Optimization (ACO) technique in a safe ship control system. The method developed solves the problem of path planning and collision avoidance of a ship in the open sea as well as in restricted waters. The structure of the developed safe ship control system is introduced, followed by a presentation of the applied algorithm. Results showing the problem-solving capability of the system are also included. The aim of the system developed is to increase automation of a safe ship control process. It is possible to apply the proposed method in Unmanned Surface Vehicles (USVs) control system, what will contribute to the enhancement of their autonomy.

Keywords: Ant Colony Optimization; collision avoidance; computer simulation; marine transport; path planning; safe ship control; safety at sea; swarm intelligence

INTRODUCTION

Technological development led to an increased marine traffic, which caused navigation to become more demanding for deck officers. A safe ship control system, containing equipment such as a log, a gyrocompass, a GPS, a radar with an Automatic Radar Plotting Aid (ARPA), an Automatic Identification System (AIS), an Electronic Chart Display and Information System (ECDIS) and an autopilot, enables realization of various methods of navigator's decision support.

Safe ship control is a complex process, because it requires a continuous analysis of large amount of information and quick decision making. Incorrect assessment of the current navigational situation based upon data from navigational devices can lead to a collision situation, often with very tragic consequences.

The newest ARPA systems enable manual and/or automatic tracking of up to 100 objects detected by a radar, and then simulating the manoeuvre planned by the navigator (trial manoeuvre function), but do not determine safe course or speed changes.

The development of modern computational intelligence methods enables the synthesis of a safe ship control system. The aim of a safe ship control system is to determine a safe course or speed manoeuvre, or a safe trajectory of the ship, taking into account the dynamic properties of the vessel at various loading conditions and at various operational speeds, manoeuvring rules of the vessel in fair weather condition and in reduced visibility at sea, limitations of the environment and the corresponding quality index of control, taking into account both the optimality and safety criterion.

Research on ships collision avoidance started in the 1960s and the first studies were concerned with a collision avoidance manoeuvre in an encounter situation between two ships. There was a necessity to consider the International Regulations for Preventing Collisions at Sea (COLREGs) in solving a collision situation, therefore in 1974 Jones [12] developed the manoeuvre diagram to provide the possibility of including the COLREGs in determining the evasive manoeuvre of a ship. In the 1970-1980s the concept of collision risk assessment with the use of a ship domain was developed by Fujii & Tanaka (1971) [9], Goodwin (1975) [10], Davis et al. (1980) [7] and Coldwell (1983) [6]. In the 1970s the idea of determining optimal collision avoidance manoeuvres with the use of the differential games theory was introduced by Olsder & Walter (1977) [17] and Kudriaszov & Lisowski (1979) [13], and considered for an encounter situation between two ships. Later Lisowski developed a differential games approach for multi-ship encounter situations [16].

In the 2000s ship path planning approaches were reported. A deterministic path planning method was introduced by Chang et al. in 2003 [5] and developed by Szłapczyński in 2006

[20]. Artificial intelligence methods for ship path planning were reported by Śmierzchalski & Michalewicz (2000) [22], Lisowski (2001) [15], Ito & Zeng (2001) [11], Tam & Bucknall (2010) [23], Tsou & Hsueh (2010) [25], Perera et al. (2011) [18], Szłapczyński (2012) [21] and others. However, all of these methods are not deprived of disadvantages. They are characterized by the limitations such as disregarding of the ship's dynamics or static obstacles and ignoring some of the COLREGs.

The paper presents an application of one of the modern global optimization methods to a safe ship control process. The idea of utilizing the Ant Colony Optimization (ACO) method in a decision support system for ships was introduced by Lazarowska in 2012 [14]. The method is inspired by a collective behaviour of ants and due to that reason it is called the Ant Colony Optimization (ACO). ACO belongs to Swarm Intelligence (SI) methods. The term SI was introduced by G. Beni and J. Wang in relation to cellular robotic systems [2]. E. Bonabeau, M. Dorigo and G. Theraulaz extended the definition of SI, defining this term as any attempt to build an algorithm inspired by the collective behaviour of the colony of insects or other animal communities [3].

The first problem solved with the use of ACO was the Traveling Salesman Problem (TSP) [8], which is a transition path optimization task. Brand et al. [4], M. Pluciński [19] and others developed ACO based algorithms for mobile robot path planning. Other applications of ACO include feature selection [1], vehicle routing problem (VRP), data network routing and ship routing [24]. In this paper ACO is used in a safe ship path planning method.

SAFE SHIP CONTROL UTILIZING ACO

The task of a safe ship control system is to determine safe controls of a ship, which is a safe course and/or speed change or a sequence of safe course and/or speed changes, called a safe ship trajectory. This is accomplished with the use of an appropriate control algorithm. The input to the algorithm is the current state of the process. The state of the process is determined with the use of information describing the actual navigational situation, which include:

- the course and speed of the own ship (OS),
- the course and speed of j-th target ship (TS),
- the bearing of the j-th target ship,
- the distance of the j-th target ship from the own ship,
- data about static obstacle (shoals, lands, buoys).

A diagram of a safe ship control system is shown in Fig. 1.

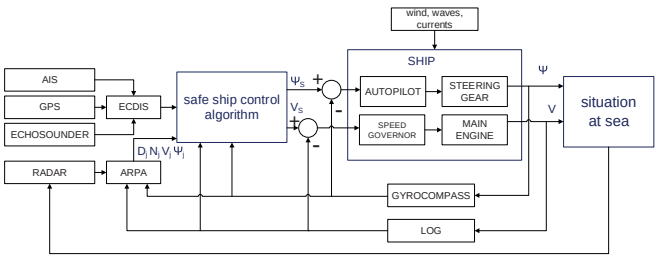

Fig. 1. A block diagram of safe ship control system (Ψ – OS course, V – OS speed, Ψj – TS course, Vj – TS speed, Nj – TS bearing from OS, Dj – TS distance from OS, Ψs – safe course of OS, Vs – safe speed of OS)

In the method developed the following assumptions were made:

- to take into account static and dynamic limitations,
- to determine a safe ship trajectory to a specified endpoint,
- a kinematic model of ship motion,
- to take into account the dynamics of the OS through the application of the time of manoeuvre,
- navigational data concerning target ships from ARPA and AIS,
- to determine a safe ship trajectory in compliance with COLREGs,
- a safety area around the TS in the form of a hexagon domain,
- computational time not exceeding sixty seconds,
- reproducible results,
- not taking into account the strategies of TSs.

MODEL OF THE PROCESS

It was assumed that TS does not change its course and speed. The process of collision avoidance at sea was described with the use of a kinematic model of ship motion, where state variables and controls are defined in the following way: $x_1 = X$, $x_2 = Y$, $x_{2j+1} = X_j$, $x_{2j+2} = Y_j$, $u = \Psi$, where $j = 1,2, ...,$ m – number of encountered TSs, X and Y are coordinates of the OS position, X_j and Y_j are coordinates of the TS position. The state equation of the safe ship control process are described by equations (1). Dynamic properties of OS are considered during the assessment of a determined trajectory in the form of the time of manoeuvre.

$$\begin{aligned} \dot{x}_1 &= V \times \sin u(t) = V \times \sin \Psi(t) \\ \dot{x}_2 &= V \times \cos u(t) = V \times \cos \Psi(t) \\ \dot{x}_{2j+1} &= V_j \times \sin \Psi_j(t) \\ \dot{x}_{2j+2} &= V_j \times \cos \Psi_j(t) \end{aligned} \tag{1}$$

SAFE SHIP CONTROL ALGORITHM

After reception of information describing the current navigational situation, a relative course, bearing and speed of each TS is calculated. The procedure of determining dangerous objects consists of checking for each TS, whether it is a dangerous object (Fig. 3). A dangerous object is an object which intersects its course with the course of the OS. Then a division of the OS route from an actual position to an endpoint into a certain number of steps is executed and on that basis a graph of possible waypoints of the OS is built in the allowable state space (Fig. 4). The calculation of a safe ship trajectory with the use of ACO consists of three main stages: the data initialization, the solutions construction (Fig. 5) and the pheromone trail update procedure (Fig. 6). When the algorithm reaches the maximum number of iterations or the maximum computational time, the best solution is selected based upon the fitness function calculation (Fig. 7). After that the following output data are displayed: the course of the OS at every line segment of the determined trajectory, the time taken for the OS to reach the endpoint, the distance travelled and a graphical presentation of the safe ship trajectory.

A pseudo-code of the safe ship control algorithm utilizing ACO is shown in Fig. 2.

```
Input: Ψ, V, Ψ_j, V_j, N_j, D_j, static restrictions
1: calculate Ψ_rj, N_rj, V_rj
2: determine dangerous objects
3: build a graph of permissible OS waypoints
4: initialize α, β, ρ,τ_0, m, it
5:    for i=1, …, it, do
                                  6:
      if (t < t_max) then
7:                 solutions construction
8:                 pheromone update procedure
                                  9:
      end-if
10:   end-for
11: choose the best solution
Output: Ψ_S, V_S, time, d, graphical solution
```

Fig. 2. A pseudo-code of the safe ship control algorithm (Ψrj – TS relative course, Nrj – TS relative bearing, Vrj – TS relative speed, α – coefficient defining the importance of τ, β – coefficient defining the importance of heuristic value, ρ – pheromone evaporation rate,τ0 – initial pheromone trail amount, m – number of ants, it – number of iterations, tmax – maximum computational time, time – time of OS passage to the endpoint, d – length of the safe trajectory

```
Procedure of determining dangerous objects
1: for j=1, …, n, do
2:    if (intersection point==empty) then
3:       mark TS as safe
4:    else
                                  5:
      if (intersection point> allowable space) then
6:                mark TS as safe
                                  7:
      else
8:                calculate distance of OS to intersection
point
9:                calculate time of OS to intersection point
10:            calculate TS position
                                  11:
      end-if
12:   end-if
13: end-for
```

Fig. 3. Procedure of determining dangerous objects (n – number of TSs)

```
Procedure of building a graph of possible OS waypoints
1: division of OS route
2: waypoint generation
3: placement of TS domains
4: for j=1, …, n, do
5:    for w=1, …, w_max, do
                                  6:
      if (w exceeds TS domains) then
7:                mark w as exceeding constraints
                                  8:
      end-if
9:    end-for
10: remove waypoints exceeding constraints
11: end-for
```

Fig. 4. Procedure of building a graph of possible OS waypoints (n – number of TSs, wmax – number of waypoints)

```
Procedure of ACO solution construction
1: for ant=1, …, m, do
2:    for step=1, …, step_max, do
                                  3:
      if (wp_i != wp_e) then
4:                action choice rule
                                  5:
      end-if
6:    end-for
7:    calculate the length of ant's path
8:    if (ant's path < min path) then
9:       min path:= ant's path
10:   end-if
11: end-for
```

Fig. 5. Procedure of ACO solution construction

```
Procedure of pheromone trail update
1: for w=1, …, w_max, do
2:    τ[w]:=(1-ρ)× τ[w]
3: end-for
4: for ant=1, …, m, do
5:    for w=1, …, w_max, do
                                  6:
      if (w belongs to ant's path) then
7:                τ[w] := τ[w] + Δτ
                                  8:
      end-if
9:    end-for
10: end-for
```

Fig. 6. Procedure of pheromone trail update

Procedure of the best solution selection
1: **for** *i*=1, …, *paths*, **do**
2: division of path into *k* stages
3: placement of TS domains
4: **for** *k*=1, …, k_{max}, **do**
5: constraints placement
6:
if (OS exceeds constraints) **then**
7: mark *i* as incorrect path
8: break;
9:
end-if
10: **end-for**
11: mark *i* as correct path
12: **end-for**
13: determine the best path from correct paths

Fig. 7. Procedure of the best solution selection

RESULTS OF SIMULATION TESTS

The developed algorithm for the safe ship control was implemented in the MATLAB programming language. The choice of this environment was due to the built-in plotting and dynamic simulation functions that allow easy graphical presentation of results. The algorithm was tested extensively using dozens of various navigational situations. Calculations were made using a PC with an Intel Core i5 M430 2.27 GHz, 2GB RAM processor and 32-bit Windows 7 Professional system. Results of several representative test cases are presented below in Fig. 8 to 19.

The results obtained allow to formulate the following conclusions:

- every solution constitutes a safe ship trajectory, what means that at any stage of the own ship movement along the path the static and dynamic navigational restrictions are not exceeded,
- solutions fulfil the COLREGs,
- results, despite the probabilistic nature of the applied optimization method, are the same for each repetition of calculations for the same navigational situation,
- the developed algorithm has low computational time, not exceeding one minute even for complex situations,
- the algorithm is suitable for use in a safe ship control system due to the fulfilment of all the most important criteria, that is the safety, compatibility with COLREGs, short computational time and repeatability of solution,
- solutions returned by an algorithm from the perspective of all of the vessels involved in the navigational situation do not intersect, what allows the use of such a safe ship control system by all of the vessels simultaneously.

The COLREGs compliance of solutions can be observed by analysing the graphical presentation of results. For example a trajectory calculated by the algorithm for a navigational situation presented in Fig. 16 fulfils rule 15 of COLREGs. Rule 15 states that in the crossing situation of two power-driven vessels, the vessel that has the other vessel on her starboard side shall keep out of the way and if the circumstances of the case admit, avoid crossing ahead of the other vessel. In the situation presented in Fig. 16 OS marked with 0 and TS 2 are crossing. As it can be seen in Fig. 17, OS which is the give-way ship, keeps out of the way and passes astern TS, what proofs that OS trajectory is compliant with rule 15 of COLREGs.

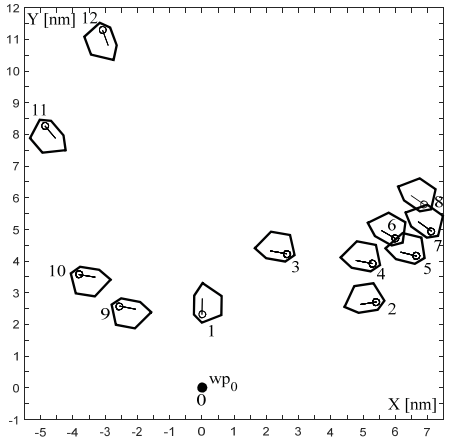

Fig. 8. Navigational situation with 12 TS - OS at wp_0

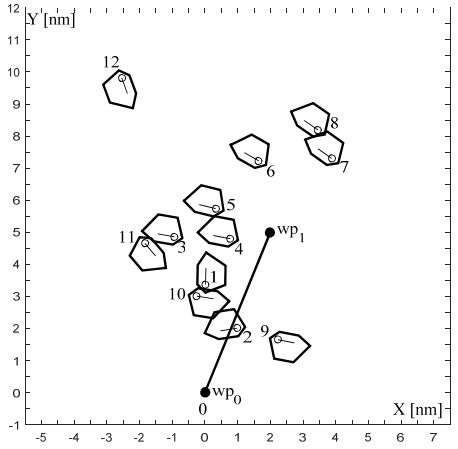

Fig. 9. Graphical solution for situation with 12 TS - OS at wp_1

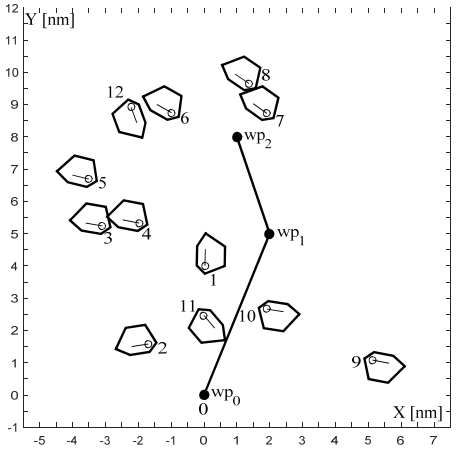

Fig. 10. Graphical solution for situation with 12 TS - OS at wp_2

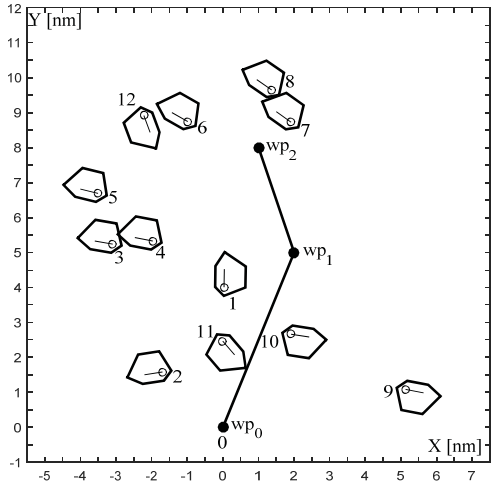

Fig. 11. Graphical solution for situation with 12 TS - OS at wp_e

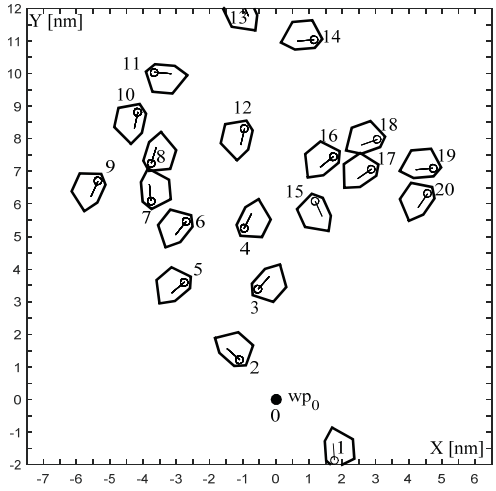

Fig. 12. Navigational situation with 20 TS - OS at wp_0

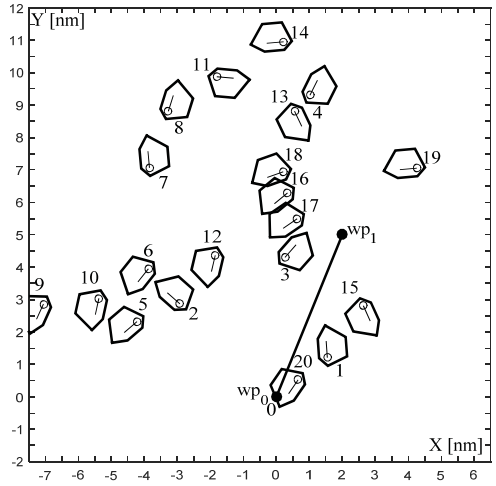

Fig. 13. Graphical solution for situation with 20 TS - OS at wp_1

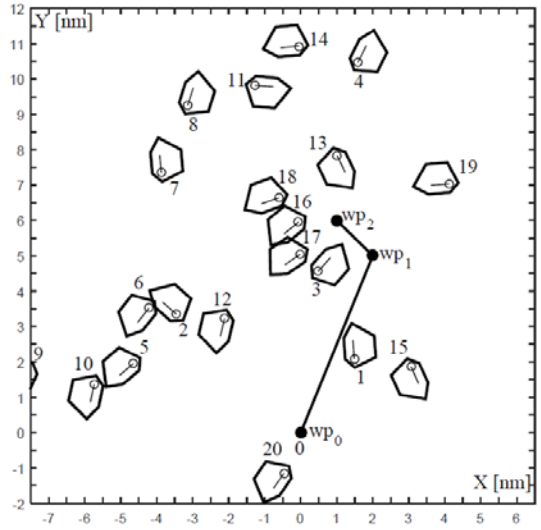

Fig. 14. Graphical solution for situation with 20 TS - OS at wp_2

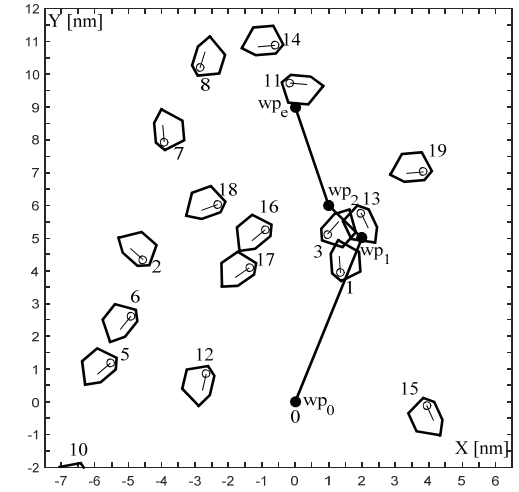

Fig. 15. Graphical solution for situation with 20 TS - OS at wp_e

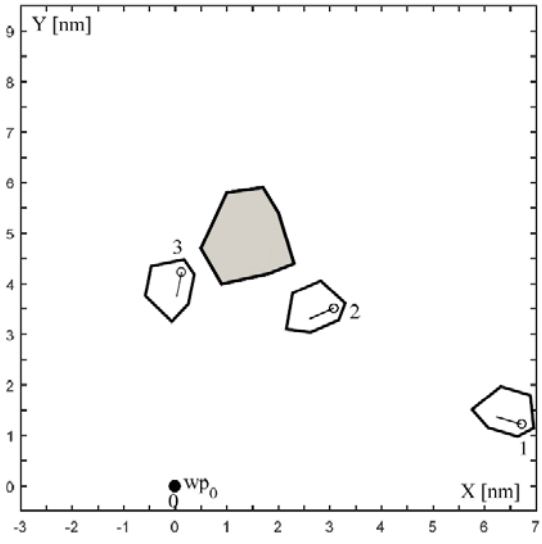

Fig. 16. Navigational situation with an island and 3 TS - OS at wp_0

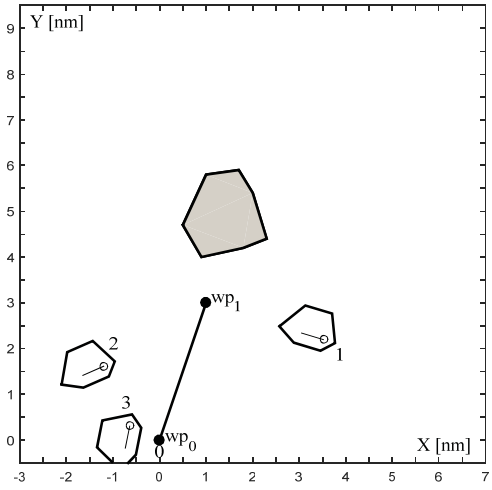

Fig. 17. Graphical solution for situation with 3 TS - OS at wp_1

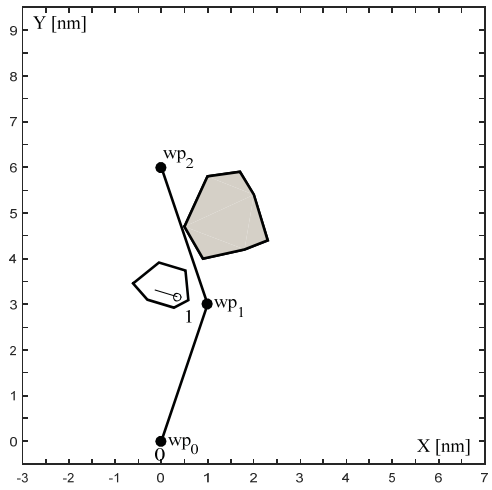

Fig. 18. Graphical solution for situation with an island and 3 TS - OS at wp_2

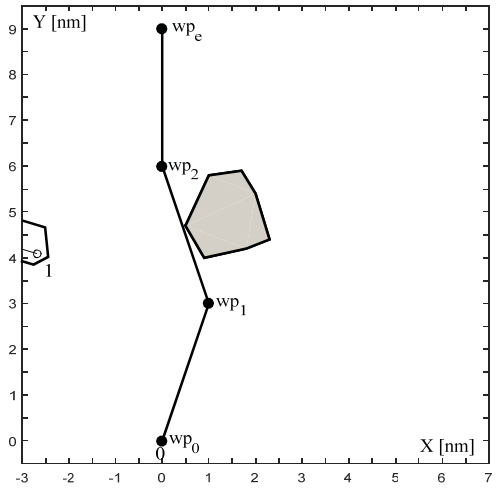

Fig. 19. Graphical solution for situation with an island and 3 TS - OS at wp_e

CONCLUSIONS

Analysis of the safe ship control method, taking into account the condition of optimal control, and results of simulation studies of the developed algorithm allows to formulate the following concluding remarks.

Presented method of safe ship control utilizing ACO can be easily adapted for use in collision avoidance support systems in aviation and land navigation.

Developed method of safe, optimal course changes in collision situation at sea, with the presence of a great amount of target ships and taking into account the static and dynamic limitations, is the process of determining the safe, optimal path of a moving object in a dynamic environment, and the solution of this problem is widely applicable in robotics and military, including control systems of unmanned vehicles.

The synthesis of safe ship control system using stochastic global optimization method allowed to take into account the COLREGs, greater amount of dynamic and static navigational restrictions, dynamic properties of the ship, determination of a safe ship trajectory to the specified endpoint and obtain not colliding solutions from the perspective of all of the vessels involved in the collision situation.

The results of the simulation tests show that the process of reproducing the behaviour of a biological system, such as an ant colony, to resolve complex problems of maritime transport, marine environment protection and increase of safe ship control automation through an automatic determination of safe, optimal course changes in collision situation at sea, indicates a high potential of nature-inspired methods in practical industrial applications.

The developed method is suitable for solving situations in areas of heavy traffic, where most of the collisions occur.

The analysis of simulation results showed that despite the application of a stochastic optimization method, the algorithm provides reproducible solutions.

The proposed algorithm is robust to changes of target ships strategies, because it is able to continuously return solutions, based on actual data from ARPA and AIS, in a very short time.

The possibility to change the shape and size of the target ship domain enables taking into account weather conditions of good and limited visibility and also the preferences of the decision maker - the system operator.

BIBLIOGRAPHY

1. Barbosa H.J.C.: *Ant Colony Optimization - Techniques and Applications,* InTech, 2013.

2. Beni G., Wang Jing: *Theoretical problems for the realization of distributed robotic systems*. IEEE International Conference on Robotics and Automation, 1991.

3. Bonabeau E., Dorigo M., Theraulaz G.: *Swarm Intelligence: From Natural to Artificial Systems*. Oxford University Press, Inc., 1999.

4. Brand M., Masuda M., Wehner N. , Yu Xiao-Hua: *Ant Colony Optimization Algorithm for Robot Path Planning*, International Conference On Computer Design And Applications, 2010.

5. Chang Ki-Yin, Jan G. E., Parberry I.: *A Method for Searching Optimal Routes with Collision Avoidance on Raster Charts*. The Journal of Navigation, Vol. 56, 2003, p. 371–384.

6. Coldwell T.G.: *Marine Traffic Behaviour in Restricted Waters*. The Journal of Navigation, Vol. 36, 1983, p. 430–444.

7. Davis P.V., Dove M. J., Stockel C. T.: *A Computer Simulation of Marine Traffic Using Domains and Arenas*. The Journal of Navigation, Vol. 33, 1980, p. 215–222.

8. Dorigo M., Stützle T.: *Ant Colony Optimization*. The MIT Press, 2004.

9. Fujii Y., Tanaka K.: *Traffic Capacity*. The Journal of Navigation, Vol. 24, 1971, p. 543–552.

10. Goodwin E. M.: *A Statistical Study of Ship Domains*. The Journal of Navigation, Vol. 28, 1975, p. 328–344.

11. Ito M., Zeng Xiao-Ming: *Planning a collision avoidance model for ship using genetic algorithm*. IEEE International Conference on Systems, Man, and Cybernetics, 2001.

12. Jones K. D.: *Application of a Manoeuvre Diagram to Multi-ship Encounters*. The Journal of Navigation, Vol. 27, 1974, p. 19–27.

13. Kudriaszov V., Lisowski J.: *Model of positional game applied for the synthesis of safe ship control*. Archiwum Automatyki i Telemechaniki, Vol. 24, 1979, p. 483–497.

14. Lazarowska A.: *Decision support system for collision avoidance at sea*. Polish Maritime Research, Vol. 19, Issue S1 (74), 2012, p. 19–24.

15. Lisowski J.: *Computational intelligence methods in the safe ship control process*. Polish Maritime Research, Vol. 8, Issue 1, 2001, p. 18–24.

16. Lisowski J.: *Comparison of dynamic games in application to safe ship control*. Polish Maritime Research, Vol. 21, Issue 3, 2014, p. 3–12.

17. Olsder G. J., Walter J. L.: *A differential game approach to collision avoidance of ships*. Proceedings of the 8th IFIP Conference on Optimization Techniques, Würzburg, 1977.

18. Perera L. P., Carvalho J. P., Guedes Soares C.: *Fuzzy logic based decision making system for collision avoidance of ocean navigation under critical collision conditions*. Journal of Marine Science and Technology, Vol. 16, No.1, 2011, p. 84–99.

19. Pluciński M.: Application of the Ant Colony Algorithm for the Path Planning. Enhanced Methods in Computer Security, Biometric and Artificial Intelligence Systems, 2005, p. 345–352.

20. Szłapczyński R.: *A New Method of Ship Routing on Raster Grids, with Turn Penalties and Collision Avoidance*. The Journal of Navigation, Vol. 59, 2006, p. 27–42.

21. Szłapczyński R.: *Evolutionary approach to ship's trajectory planning within Traffic Separation Schemes*. Polish Maritime Research, Vol. 19, Issue 1, 2012, p. 11–20.

22. Śmierzchalski R., Michalewicz Z.: *Modeling of Ship Trajectory in Collision Situations by an Evolutionary Algorithm*. Transactions on Evolutionary Computation, Vol. 4, 2000, p. 227–241.

23. Tam Ch., Bucknall R.: *Path-planning algorithm for ships in close-range encounters*. Journal of Marine Science and Technology, Vol. 15, 2010, p. 395–407.

24. Tsou M.-Ch., Cheng H.-Ch.: *An Ant Colony Algorithm for efficient ship routing*. Polish Maritime Research, Vol. 20, Issue 3, 2013, p. 28–38.

25. Tsou M.-Ch., Hsueh Ch.-K.. *The Study of Ship Collision Avoidance Route Planning by Ant Colony Algorithm*. Journal of Marine Science and Technology - TAIWAN, Vol. 18, 2010, p. 746–756.

CONTACT WITH THE AUTHOR

Agnieszka Lazarowska

Gdynia Maritime University
11/12 Narutowicza St.
80 - 233 Gdańsk
Poland

POLISH MARITIME RESEARCH 4(88) 2015 Vol. 22; pp. 41-47
10.1515/pomr-2015-0069

A MODEL OF THERMAL ENERGY STORAGE ACCORDING TO THE CONVENTION OF BOND GRAPHS (BG) AND STATE EQUATIONS (SE)

Marian Cichy, Prof.
Jacek Kropiwnicki, Ph. D.
Zbigniew Kneba, Ph. D.
Gdańsk Univeristy of Technology, Poland

ABSTRACT

The main advantage of the use of the Bond Graphs method and State Equations for modeling energy systems with a complex structure (marine power plants, hybrid vehicles, etc.) is the ability to model the system components of different physical nature using identical theoretical basis. The paper presents a method of modeling thermal energy storage, which is in line with basic BG theory. Critical comments have been put forward concerning multiport energy storage introduced by other authors or the so-called C-field. In suggested approach, the decision not to use pseudo Bond Graphs has been justified as not being in line with basic BG theory. On the basis of molecular physics it was considered that the state variable, in physical and mathematical sense, should be temperature rather than entropy. Examples of the application of the proposed approach to thermodynamic processes and heat exchange have been presented. The application of a single graph as a model for thermal energy storage has been illustrated by a way of numerical simulation examples.

Keywords: Energy systems modeling; Bond Graphs method

INTRODUCTION

In complex energy systems heat exchange elements are used to determinate the total efficiency and the impact of the systems on the environment [7, 19]. Usage of mathematical modeling and numerical simulation for construction improvement and energy saving, creates the need for a unified and comprehensive modeling of the entire system [2, 3, 8, 14, 16, 17, 18, 20, 21, 22]. The method, which enables the realization of such tasks is the method of BG and SE.

In basic BG theory applied in problems in the area of mechanics, hydraulics, electricity, power stations, marine power plants and complex energy systems [4, 5, 11, 26, 28, 30] the following graphs with single nodes are used as "external" model elements:

- Sources of effort and sources of flow,
- Kinetic and potential energy storage,
- Elements that dissipate energy (dissipating elements).

Elements with multiport nodes are one nodes, zero nodes and energy converters in the form of transformers and gyrators.

The application of this basic theory to thermal processes has encountered difficulties from the start. These difficulties are mainly related to the failure to find an answer to following questions: Which parameter does the accumulation of energy represented or in other words, which parameter can be considered to be the state variable in mathematical sense? Does the accumulated thermal energy constitute potential energy or kinetic energy? Does the introduction of the concept of "resistance" [11, 27, 28] to the modeling of thermal processes represent the dissipation of energy or its degradation? The lack of answer to these questions led to the introduction of so-called pseudo bond graphs (PBG) [4, 10, 11, 12, 25, 26, 27, 29] in parallel with real bond graphs. This was a considerable departure from the basic theory, in which the unit of the product of generalized effort and generalized flow is the unit of power. Further elements, which have been specially introduced to the thermal process models are double nodes of energy storage and of thermal resistance as well as the graph defined by a double pair of energetic parameters [4, 21, 26].

The graph representing the thermal energy storage adopted by the cited authors is shown in figure 1.

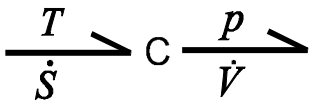

Fig. 1. BG model of thermal energy storage adopted in papers [11, 28, 30]

The energy storage model in the form as shown in figure 1 does not fit the general BG theory. General BG theory concerns energy storage element as an 1-port type element, which fulfills the following relation:

$$\sum_{i=1}^{N} e_i f_i = 0 \tag{1}$$

On the basis of molecular physics [1, 6, 13, 24], it is possible to state that the only form of accumulating thermal energy in gases is the kinetic energy of molecules, which is exclusively dependent on temperature. In solid bodies where intermolecular forces play an important role, molecules form oscillators that store kinetic and potential energy [26]. The heat capacity in constant-volume of solid bodies is dependent on temperature and is determined on the basis of Debye theory [6, 13, 24].

The basic objective of this paper is to show that the models of thermal processes in the form of BG can be created by solely applying elements incorporated in basic BG theory. This means, that the introduction of 2-port type energy storage element and 2-port type thermal resistance element into the modeling of thermal processes, pseudo bond graphs in particular, is not expedient and just complicates the modeling of complex energy systems that require a uniform approach to modeling the elements of the system, in which the processes of a physical nature occur. An example of such a system is a model of an internal combustion engine described in the paper [8].

THE PROPOSAL OF A NEW APPROACH TO THE MODELING OF THERMAL PROCESSES

As already stated in the proposed approach, solely the elements of the BG are applied that have been incorporated in the modeling of mechanical, hydraulic and electrical processes. Temperature rather than entropy [23] has been adopted as the state variable defining the storage of thermal energy. In basic BG theory, the graph representing thermal energy storage is a 1-port type element [8, 9]. The speed of accumulation is defined by the relation:

$$\frac{\mathrm{d}U}{\mathrm{d}t} = \dot{E}_A = \frac{\mathrm{d}(C_v m T)}{\mathrm{d}t} \tag{2}$$

It was assumed that R element is 1-port type element and represents energy loss process, due to irreversible energy transfer to the atmosphere. The problem of dissipation element R will be illustrated by example in this chapter below. State equations are determined on the basis of the relation obtained directly from the graphical model:

$$\dot{E}_A = \sum_{i=1}^{N} \dot{E}_i \tag{3}$$

On the basis of molecular physics [1, 6, 13, 24], it is possible to state that the only form of accumulating thermal energy in gases is the kinetic energy of molecules, which is exclusively dependent on temperature. In solid bodies where intermolecular forces play an important role, molecules form oscillators that store kinetic and potential energy [26]. The heat capacity in constant-volume of solid bodies is dependent on temperature and is determined on the basis of Debye theory [6, 13, 24].

The basic objective of this paper is to show that the models of thermal processes in the form of BG can be created by solely applying elements incorporated in basic BG theory. This means, that the introduction of 2-port type energy storage element and 2-port type thermal resistance element into the modeling of thermal processes, pseudo bond graphs in particular, is not expedient and just complicates the modeling of complex energy systems that require a uniform approach to modeling the elements of the system, in which the processes of a physical nature occur. An example of such a system is a model of an internal combustion engine described in the paper [8].

THE PROPOSAL OF A NEW APPROACH TO THE MODELING OF THERMAL PROCESSES

As already stated in the proposed approach, solely the elements of the BG are applied that have been incorporated in the modeling of mechanical, hydraulic and electrical processes. Temperature rather than entropy [23] has been adopted as the state variable defining the storage of thermal energy. In basic BG theory, the graph representing thermal energy storage is a 1-port type element [8, 9]. The speed of accumulation is defined by the relation:

$$\dot{\mathbf{T}} = f_T(\mathbf{T}, \mathbf{U}) \tag{4}$$

where:

T - the vector of the temperatures of individual elements of the system,

U – the vector the independent functions of time characterizing the energy fluxes in the system under consideration (control vector).

The energy sources in the thermal processes adopted in the paper are shown on figure 2. It should be noted, that in the "b" type source, both energetic parameters may be independent functions of time. A new development is adopting source "c", in which the thermal flux is an independent function of time. Such source is present in a feedwater heater or a microwave oven, for example. Energy converters (fields) have been introduced (fig. 2) without the need to declare their type; whether they are a transformer or gyrator. Solely the basic condition (1) is fulfilled, which means:

$$e_{in} f_{in} = e_{out} f_{out} \tag{5}$$

Relations between parameters pointed in equation (5) can be either linear or nonlinear.

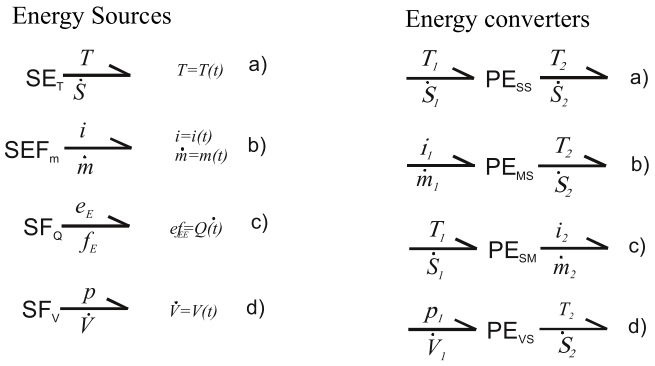

Fig. 2. Energy sources and converters used in the proposed modeling method

The problem of energy transducers and dissipation element R will be illustrated by example of en electrical circuit with resistor shown on fig. 3.

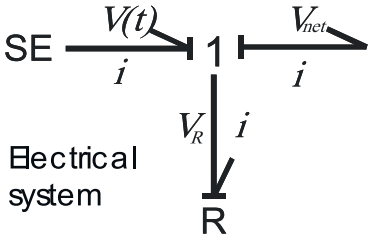

Fig. 3. Electrical circuit with resistor

R element transforms electrical energy to thermal energy. A real resistor is a thermal energy storage element with it's properties: mass, specific heat, area which exchanges heat with the ambient. A resistor model should respect those parameters and have the possibility to calculate temperature by some different ways of heat exchange with the ambient. According to our proposal, using energy transducer and heat dispersing element allows to construct a model which joins electrical and thermal elements (fig. 4).

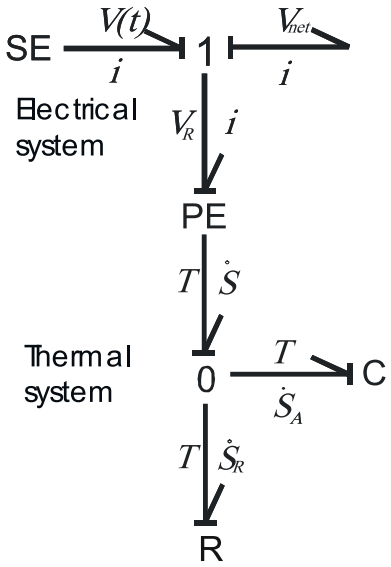

Fig. 4. Model which joins electrical and thermal elements

PE element transforms electrical energy to thermal energy, however R element disperses this energy to the ambient. There is no doubt that our model allows better processes simulation which are taking place in above example. It is obvious, that dissipating energy flux during steady state ($\dot{S}_A = 0$) is equal $T\dot{S}_R = V_R i$.

In the following paragraphs application examples of this approach will be presented as well as numerical simulations using BG elements shown on figure 2 and state equations.

BG MODEL OF THERMAL ENERGY STORAGE IN THERMODYNAMIC PROCESSES

An illustration of the application of the proposed approach to modeling of thermal energy storage in a thermodynamic process is the process of the change in volume $\dot{V}(t)$ shown diagrammatically on figure 5 of a defined mass of gas m, to which a thermal flux is fed Q(t). The BG model of this process using the elements from figure 2 is shown on figure 6.

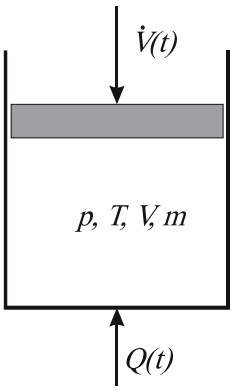

Fig. 5. Diagram of the thermodynamic process under consideration

The control vector in the state equation (4) for the BG model on figure 4 is:

$$\mathbf{U} = \begin{bmatrix} \dot{V} \\ Q \end{bmatrix} \tag{6}$$

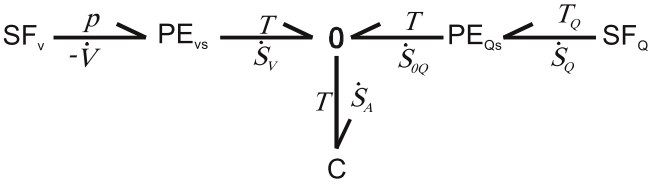

Fig. 6. Model of the thermodynamic process in the form of a bond graph

The basic state equation in accordance with the general relation (3) directly obtained from the BG model on figure 6 is:

$$T\dot{S}_A = -p\dot{V} + T_Q\dot{S}_Q \tag{7}$$

In accordance with the adopted definitions:

$$T\dot{S}_A = \frac{dU}{dt} \text{ and } T_Q \dot{S}_Q = Q$$

the equation (7) represents the first law of thermodynamics. After incorporating relation (2) in the relation (7) and applying the Clapeyron equation, the relation (7) will be transformed into the general form of a state equation (4), which in the case under consideration is the form of:

$$\dot{T} = -\frac{R}{C_V} * \frac{\dot{V}(t)}{V(t)} T + \frac{Q(t)}{C_V m} \quad (8)$$

NUMERICAL EXAMPLE OF A SIMULATION OF THE THERMODYNAMIC PROCESS

The example concerns the compression process with a thermal flux being fed. Oxygen has been adopted as the medium (R = 259.8 kJ/kgK, C_V = 0.66 kJ/kgK). The adoption of a constant value for specific heat does not change the equation (8). The initial conditions for t=0:

p_p =105 Pa; T_p =290 K; V_p =10^{-2} m^3.

From the state equation, the mass of the medium m = 1.33 10^{-2} kg. The course of the change in volume has been taken to be in the form of a function:

$$V = A_V \cos \omega t + A_V + V_k \quad for\ 0 \le t \le \tau / 2 \quad (9)$$

In the calculations, it has been accepted that: V_k = 10^{-3} m^3; τ = 0.1 s. Based on this data the following was calculated:

$$\omega = \frac{2\pi}{\tau} = 31.4\ rad/s\ ; \quad A_V = \frac{V_p - V_k}{2} = 4.5 \cdot 10^{-3}\ m^3$$

The speed of the change in volume for $t \in \langle 0, \tau \rangle$ is expressed by way of the relation:

$$\dot{V} = -\omega\ A_V \sin \omega t \quad (10)$$

The course of the thermal flux has been defined by the relation:

$$Q(t) = -\frac{4Q_{\max}}{\tau^2} t(t - \tau) \quad \text{for } t \in \langle 0, \tau \rangle \quad (11)$$

where:
Q_{max} – maximal thermal flux for $t \in \langle 0, \tau \rangle$
(Q_{max} = 5 kW).

The course of temperature and pressure for the assumed excitations V(t) and Q(t) is shown on figures 7 and 8.

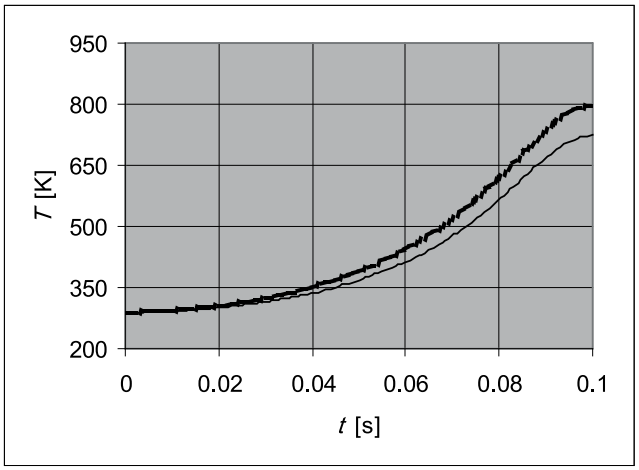

Fig. 7. Course of temperature in the cylinder for the above data: thick line – with heat exchange, according to the relation (12), Q_{max} = 5 kW; thin line – without heat exchange

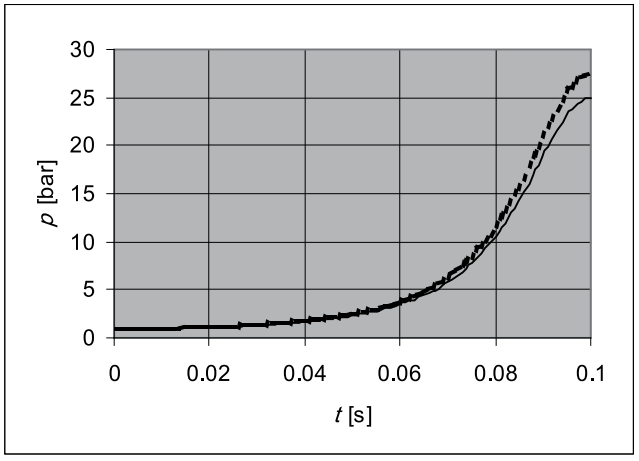

Fig. 8. Course of pressure in the cylinder for the above data: thick line – with heat exchange, according to the relation (12), Q_{max} = 5 kW; thin line – without heat exchange

It is easy to prove that work without any heat exchange process (presented on fig. 5 and 6) is an adiabatic transformation.

BG MODEL OF THE BASIC ELEMENTS OF HEAT EXCHANGE

The presented example of modeling encompasses energy transfer processes in the flux of a flowing fluid, heat exchange by convection and conduction as well as dissipation of energy by convection to the environment and by outflow of energy contained in the mass of the flowing medium. A diagram of the system under consideration is shown on figure 9. A model of these processes in the form of a BG, with the elements introduced as part of this approach (fig. 2) being applied is shown on figure 10.

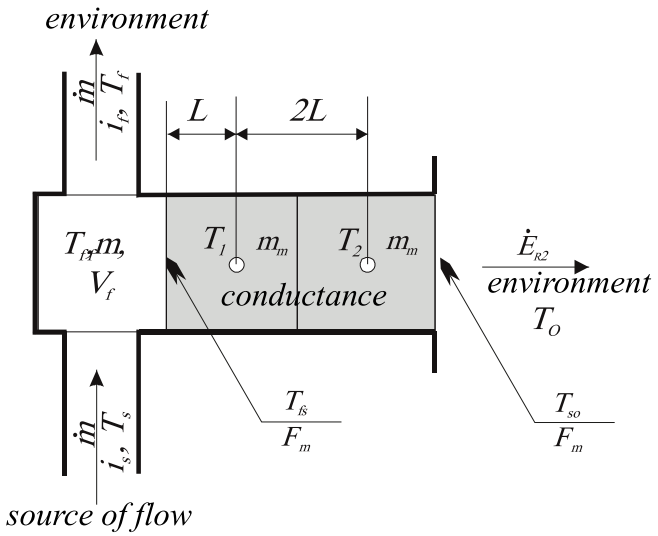

Fig. 9. Example of a system of heat exchange by convection and conductance

In accordance with the BG model the state variable vector for the example under consideration is:

$$\mathbf{T} = \begin{bmatrix} T_f & T_1 & T_2 \end{bmatrix}^T \tag{12}$$

The following notations will be introduced for thermal energy flux:

- The energy flux of the source SEFm: $\dot{E}_S = \dot{m} \cdot i_S$,
- Accumulated energy fluxes C_f in the liquid heat exchanger: $\dot{E}_{Af} = \dot{m} i_A$; C_1 and C_2 in the first and second conducting element: $\dot{E}_{A1} = T_1 \cdot \dot{S}_{A1}$; $\dot{E}_{A2} = T_2 \cdot \dot{S}_{A2}$,
- Energy flux transferred in the exchanger through the liquid to the first conducting element: $\dot{E}_f = \dot{m} \cdot i_f = T_1 \cdot \dot{S}_{11}$,
- Energy flux transferred by the first conducting element to the second conducting element: $\dot{E}_{12} = T \cdot_1 \dot{S}_{12} = T_2 \cdot \dot{S}_{21}$
- Energy fluxes dissipated by the outflow of the liquid Ro1 and by convection to the environment R_{o2}: $\dot{E}_{R1} = \dot{m} \cdot i_R$; $\dot{E}_{R2} = T_2 \cdot \dot{S}_{22}$.

The basic form of state equations obtained directly from the BG model is as follows:

$$\begin{aligned} \dot{E}_{Af} &= -\dot{E}_f - \dot{E}_{fRo1} + \dot{E}_S \\ \dot{E}_{A1} &= \dot{E}_f - \dot{E}_{12} \\ \dot{E}_{A2} &= \dot{E}_{12} - \dot{E}_{Ro2} \end{aligned} \tag{13}$$

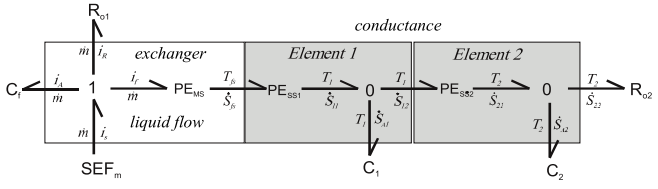

Fig. 10. BG model of the heat exchange processes for the system in figure 6

By substituting the general relation (2) for the speed of thermal energy accumulation and applying the basic convection relations:

$$\dot{E}_{kon} = \alpha F \left(T_H - T_L \right) \tag{14}$$

and conduction relations:

$$\dot{E}_{prze} = \frac{\lambda F_p}{L_p} \left(T_i - T_{i-1} \right) \tag{15}$$

and by expressing the temperature of the walls T_{fs} and T_{so} via elements of the vector T and U, the form of state equations is obtained (4), which linear form supplemented by algebraic equations is:

$$\begin{aligned} \dot{\mathbf{T}} &= \mathbf{AT} + \mathbf{BU} \\ \mathbf{Y} &= \mathbf{CT} + \mathbf{DU} \end{aligned} \tag{16}$$

where:

A, B, C and D – matrices whose elements are real numbers,

Y – the vector of parameters arbitrarily selected for the analysis of parameters (e.g. temperature, heat fluxes, entropy fluxes).

The excitation vector for the case under consideration has the following form in the model (16):

$$\mathbf{U} = \begin{bmatrix} T_s & T_o \end{bmatrix}^T \tag{17}$$

Assuming in this example, that the specific heats, the rate of flow of the fluid and the heat exchange coefficients α and λ are constant the state equation is linear and has the form (16). The usage of this method has been also described in [7, 15].

EXAMPLE OF NUMERICAL SIMULATION

For the model shown on figure 9 water has been adopted as the flow medium and aluminum as the conducting material. The model's parameters are contained in table 1. Following transformations and substitution of the parameters stated in table 1, the following equation matrices were obtained (16):

$$\boldsymbol{A} = \begin{bmatrix} -0.053226 & 0.0120737 & 0.0 \\ 0.0123999 & -0.02855 & 0.016151 \\ 0.0 & 0.016151 & -0.016226 \end{bmatrix}$$

$$\boldsymbol{B} = \begin{bmatrix} 0.04115 & 0.0 \\ 0.0 & 0.0 \\ 0.0 & 7.53 \cdot 10^{-5} \end{bmatrix}$$

Tab. 1. Model Parameters

Seq. No.	Parameter	Value
1	Mass of water in the exchanger m_f [kg]	0.0729
2	Mass of the conducting element m_m [kg]	0.33125
3	Length of the conducting element 2L [m]	0.05
4	Convection exchange area from the liquid side F_f [m^2]	0.0025
5	Convection exchange area from the environment side F_o [m^2]	0.0025
6	Cross section area of the conducting element F_p [m^2]	0.0025
7	Density of water ρ_f[kg/m^3]	972
8	Density of metal ρm[kg/m^3]	2650
9	Specific heat of water C_f[J/kg]	4200
10	Specific heat of aluminum C_m[J/kg]	900
11	Thermal conductivity of aluminum λ_m[W/mK]	160.5
12	Surface conductance from the liquid side α_f[W/m^{2}K]	4000
13	Surface conductance from the environment side α_o[W/m^{2}K]	15
14	Mass rate of flow of the liquid $\dot{m}$ [kg/s]	0.003

Excitation functions (17) were taken to be step functions:

$$T_s = \begin{cases} 293 \ for \ t < 0 \\ 360 \ for \ t \geq 0 \end{cases} ; \ T_o = \begin{cases} 293 \ for \ t < 0 \\ 293.0001 \ for \ t \geq 0 \end{cases}$$

The following were adopted as the initial conditions for t = 0:

$$\mathbf{X}_0 = \begin{bmatrix} 293 & 293 & 293 \end{bmatrix}^T$$

Figure 11 shows the course of temperature in individual elements of the system.

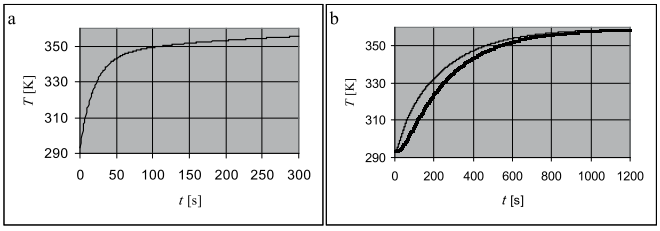

Fig. 11 Course of temperatures: a – in the liquid element; b – in the metal elements: thin line – 1st, thick line – 2nd element

FINAL CONCLUSIONS

In this paper, it has been demonstrated that using dual energy storage in the form shown on figure 1 in the modeling of thermal processes by means of bond graphs is not expedient and it is not in line with basic BG theory. The creators of this type of element most probably assumed that there are two forms of accumulating thermal energy. However, according to molecular thermodynamic theory, there is only one form of accumulating thermal energy. In his paper, Anselm [1] formulates the problem thus: "from a molecular point of view, the possibility of changing the system's energy in two ways – by the work carried out on the system and the exchange of heat with the environment – becomes self-evident". On the basis of the quoted examples of models of thermodynamic processes and heat exchange, it has been shown that using thermal energy storage in the form of a single node that is applied in basic BG theory for modeling mechanical, hydraulic and electrical processes in BG models of thermal processes is possible and perfectly justified. In the opinion of the Authors, there are no logical arguments that support using so-called "pseudo bond graphs" [4, 10, 11, 12, 25, 26, 27, 29] for modeling thermal processes, as these do not fulfill the basic condition of the product of the generalized energetic parameters having the same measure as power. It is not possible to agree with some authors [23] adopting entropy as a state variable (in a physical and mathematical sense) that characterizes the accumulation of thermal energy. In accordance with molecular thermodynamic theory it is only temperature that can be such a state variable and this has been adopted in the method of modeling thermal processes presented in this paper. In the proposed method of modeling thermal processes a graph simulating the loss of energy has been adopted as element R.

LITERATURE

1. Anselm A. I.: Podstawy fizyki statystycznej i termodynamiki. Państwowe Wydawnictwo Naukowe, Warszawa 1980.
2. B. Ould Bouamama K. Medjahera, A.K. Samantarayb, M. Staroswiecki: Supervision of an industrial steamgenerator. Part I: Bond graph modeling. Control Engineering Practice 14 (2006), pp. 71–83.
3. Badoud A.E., et al.: Bond graph modelling and optimization of photovoltaic pumping system. Simulation and experimental results. Simulation Modelling Practice and Theory 36 (2013), pp. 84–103.
4. Borutzki W.: Bond Graph Metodology. Springer Verlag, Erlangen 2010.
5. Borutzki W.: Bond graph modelling and simulation of multidisciplinary systems – An introduction. Simulation Modelling Practice and Theory 17 (2009), pp. 3–21.
6. Burtshtein A. I.: Introduction to Thermodynamics and Kinetic Theory of Matter. John Willey& Sons, Inc., 1995.
7. Cichy M., Kneba Z., Kropiwnicki J.: Zastosowanie metody grafów wiązań do modelowania układów chłodzenia silników spalinowych. Archiwum Motoryzacji, nr 1, 2005, pp. 21-34.
8. Cichy M.: Modelowanie systemów energetycznych. Wydawnictwo Politechniki Gdańskiej, Gdańsk, 2001.
9. Cichy M.: Nowe podejście do modelowania procesów cieplnych za pomocą grafów wiązań i równań stanu. Prace Naukowe Politechniki Szczecińskiej, Szczecin, 2000.
10. Hubbard M., Brever J. W.: Pseudo Bond Graphs of circulating fluids with Application to Solar Heating Design. Journal of the Franklin Institute, Vol. 311, No. 6, June, 1981.

11. Karnopp D. C., Margolis D. L., Rosenberg R. C.: System dynamics: a unified approach. Wiley, New York, 1990.

12. Karnopp D.: Pseudo Bond Graphs for Thermal Energy Transport. Journal of Dynamic Systems, Measurement and Control. Vol. 100, Sept. 1978.

13. Kittel C.: Wstęp do fizyki ciała stałego. Wydawnictwo Naukowe PWN, Warszawa, 1999.

14. Kneba Z.: Bond graph modeling of the new generation engine cooling systems. Journal of KONES. Powertrein and Transport, Vol. 13, No. 1, 2006.

15. Kneba Z.: Model chłodnicy płytowej pracującej w układzie chłodzenia samochodowego silnika spalinowego. Archiwum Motoryzacji, nr 1, 2006, pp. 37-45.

16. Kropiwnicki J., Kneba Z., Ziółkowski M.: Test For Assessing the Energy Efficiency of Vehicles with Internal Combustion Engines. International Journal of Automotive Technology, Vol. 14, No. 3 (2013), pp. 479-487.

17. Kurniawan A., et al.: Bond graph modelling of a wave energy conversion system with hydraulic power take-off. Renewable Energy 38 (2012), pp. 234-244.

18. Medjaher K., et al.: Bond graph model of a vertical U-tube steam condenser coupled with a heat exchanger. Simulation Modelling Practice and Theory 17 (2009), pp. 228–239.

19. Mielewczyk A.: A discrete model of the plate heat exchanger. Polish Maritime Research No. 2 (2008), pp. 71-76.

20. Nquien H.: A simulation model of heat exchange in the ship diesel engine cylinder - environment system. Polish Maritime Research No. 1 (2002).

21. Ould Bouamama B.: Bond graph approach as analysis tool in thermofluid model library conception. Journal of the Franklin Institute 340 (2003), pp. 1–23.

22. Pudlik W.: Wymiana i wymienniki ciepła. Politechnika Gdańska, Gdańsk, 1988.

23. Shoureshi R., McLaughlin K. M.: Analytical and Experimental Investigation of Flow-Reversibile Heat Exchangers Using Temperature-Entropy Bond Graphs. Journal of Dynamic Systems, Measurement and Control, Vol. 106, June 1984.

24. Sproull R. L.: Modern Physics. John Willey& Sons, Inc., New York, Chapman & Hall, Limited London, 1958.

25. Surjya K. Pal, Derek A. Linkens: Temperature distribution in steel during hot rolling: pseudo-bond graph view. Simulation Modelling Practiceand Theory 10, 2002, pp. 69-85.

26. Thoma J.U., Boumama B.O: Modelling and Simulation in Thermal and Chemical Engineering – a Bond Graph Approach. Springer, 2000.

27. Thoma J.U.: La termodinamica per immagini. Tecniche Nuove, Milano, 1981.

28. Thoma J.U.: Simulation by Bondgraphs. Springer, Berlin, 1990.

29. Tylee J. L. : Pseudo Bond Graph Representation of PWR Pressurizer Dynamics. Journal of Dynamic Systems, Measurement, and Control, Vol. 105, December 1983.

30. Wellstead P. E.: Introduction to System Modelling. Academic Press, London 1979.

CONTACT WITH THE AUTHOR

M. Cichy
e-mail: mcichy@pg.gda.pl

J. Kropiwnicki
e-mail: jkropiwn@pg.gda.pl

Z. Kneba
e-mail: jkropiwn@pg.gda.pl

Faculty of Mechanical Engineering
Gdansk University of Technology
Narutowicza 11/12 St.
80-233 Gdańsk
POLAND

POLISH MARITIME RESEARCH 4(88) 2015 Vol. 22; pp. 48-52
10.1515/pomr-2015-0070

NUMERICAL ANALYSIS OF EMISSIONS FROM MARINE ENGINES USING ALTERNATIVE FUELS

Lamas, M.I., Assoc. Professor[a]
Rodríguez, C.G., Ph.D Student[a]
Telmo, J. Assoc. Professor[b]
Rodríguez, J.D., Assoc. Professor[a]

a Escuela Politécnica Superior. Universidade da Coruña, Spain

b Escuela Politécnica Superior. Universidade de Santiago de Compostela, Spain

ABSTRACT

The current restrictions on emissions from marine engines, particularly sulphur oxides (SO_x), nitrogen oxides (NO_x) and carbon dioxide (CO_2), are compelling the shipping industry to a change of tendency. In the recent years, many primary and secondary reduction techniques have been proposed and employed in marine engines. Nevertheless, the increasingly restrictive legislation makes it very difficult to continue developing efficient reduction procedures at competitive prices. According to this, the paper presents the possibility to employ alternative fuels. A numerical model was developed to analyze the combustion process and emissions using oil fuel, natural gas and hydrogen. A commercial marine engine was studied, the Wärtsilä 6L 46. It was found, that hydrogen is the cleanest fuel regarding CO_2, hydrocarbons (HC) and carbon monoxide (CO). Nevertheless, it is very expensive for marine applications. Natural gas is cheaper and cleaner than fuel oil regarding CO_2 and CO emissions. Still, natural gas emits more NO_x and HC than oil fuel. SO_x depends basically on the sulphur content of each particular fuel.

Keywords: fuel; natural gas; hydrogen; marine engine; emissions

INTRODUCTION

Nowadays, environmental pollution is increasing at an alarming rate. In the marine field, ships are responsible for 15% of global NO_x emissions, 6% of global SO_x emissions and 2% of global CO_2 emissions from fossil fuels, Skjølsvik et al. [1]. These important levels forced to limit emissions from ships by regional and international authorities such as Environmental Protection Agency, European Commission, International Maritime Organization, etc.. At the international level, the International Maritime Organization (IMO) is a United Nations agency that deals with maritime safety, security and pollution coming from ships. In 1973, the IMO adopted "MARPOL 73/78, The International Convention for the Prevention of Pollution from Ships", to minimize pollution coming from ships. MARPOL is the main international agreement addressing the issue of pollution coming from ships. Annex VI of the MARPOL, "Prevention of air pollution from ships" regulates SO_x, NO_x and, more recently, CO_2. MARPOL Annex VI also regulates ozone depleting substances, volatile organic compounds from tankers, shipboard incineration and fuel oil characteristics.

Regarding SO_x, Annex VI of the MARPOL limits the sulphur content in fuels. From January 2012, the IMO requirements of maximum sulphur content in any fuel used onboard ships were reduced from 4.5% to 3.5%. From January 2020, sulphur content should not exceed 0.5%. The options for compliance with IMO new regulations include the use of low sulphur fuels/distillates, heavy fuel oil with a scrubber, natural gas, or other alternative fuels. Regarding NO_x, Annex VI of the MARPOL establishes a curve which indicates the maximum allowable NO_x emission levels related to the engine speed, applicable to marine diesel engines built after 2000 (Tier I), 2011 (Tier II) and 2016 (Tier III). Regarding CO_2, a new chapter has recently been added to MARPOL Annex VI, "Chapter 4, Regulations on energy efficiency for ships", to make the Energy Efficiency Design Index (EEDI) mandatory for new ships above 400 gross metric tons built after 1st January 2013 and the Ship Efficiency Management Plan (SEEMP) for all ships above 400 gross metric tons. The EEDI provides the grams of CO_2 per ship's capacity-mile and is calculated by a formula based on the technical design

parameters for a given ship. The SEEMP is an approach for shipping companies to manage ship and fleet efficiency performance over time.

Due to these legislative requirements, the rate of emissions is an important factor in the selection of marine engines. There are several strategies to reduce NO_x emissions from marine engines such as geometry (Bigos and Puskar [2]), modification of injection parameters (Kontoulis et al., [3] and Pantiagonis et al. [4]), water addition (Lamas and Rodríguez [5]), EGR (Millo et al. [6]), SCR (Jayaran [7]), etc. Regarding SO_x, an alternative to use low-sulphur fuels is to employ heavy fuel oil with scrubbers (Andreasen and Mayer [8]) or alternative fuels (Banawan et al. [9], Seddiek and Elgohary [10]). Regarding CO_2, reduction measurements are so expensive that the only CO_2 reduction techniques are to reduce speed and employ alternative fuels (Eide et al. [11]).

The aim of the present paper is to study the effect of alternative fuels in the emissions from marine engines. Three fuels were compared: fuel oil, natural gas and hydrogen. CO_2, HC, CO and NO_x emissions were analyzed. SO_x emissions were not analyzed because these depend on the sulphur content of each particular fuel. The engine analyzed was the Wärtsilä 6L 46 marine engine.

ANALYZED ENGINE AND COMBUSTION PROCESS

The Wärtsilä 6L 46 studied in the present work is a four-stroke, medium-speed marine diesel engine with six cylinders. Each cylinder has two intake and two exhaust valves. The numerical simulation of this engine and validation with experimental measurements were developed in previous works, Lamas et al. [12] and Lamas and Rodríguez [13]. The mesh employed in these works is indicated in Fig.1. A comparison between numerical and experimental in-cylinder pressure is indicted in Fig. 2. As can be seen, a good concordance was found. Numerical and experimental emissions were also satisfactory compared in Lamas and Rodríguez [12]. This study continues these previous works analyzing the influence of the fuel employed.

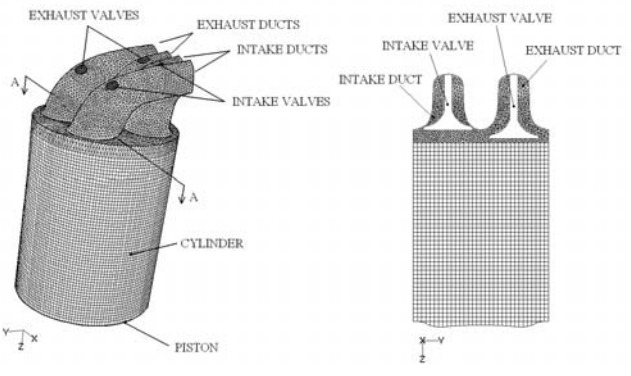

Fig 1. Computational mesh at bottom dead center position. (a) 3D view; (b) AA section

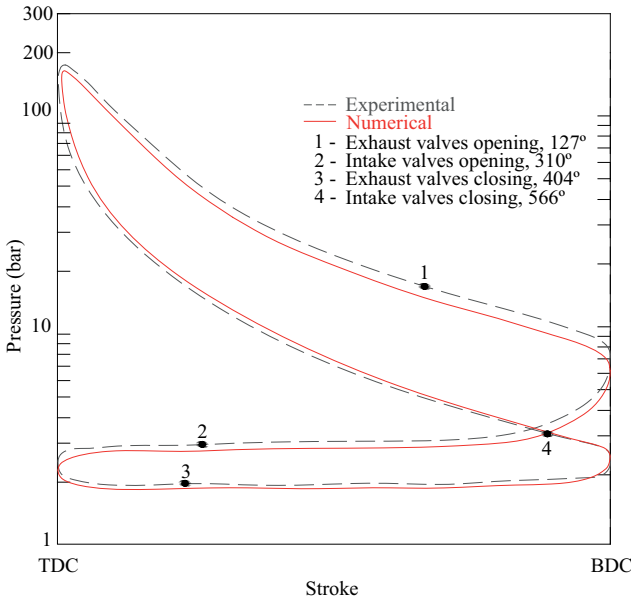

Fig 2. In-cylinder pressure obtained numerically and experimentally

Operating with fuel oil, this engine follows the diesel operating cycle. The injection system is indicated in Fig. 3. The fuel oil is introduced by a 10 holes injector in the form of a spray of liquid droplets. As the air contained in the cylinder is at high pressure and temperature, the fuel oil vaporizes and mixes with this air. After that, ignition takes place. Atomization, vaporization, fuel-air mixing and combustion continue until all the necessary fuel has passed through each process. In addition, mixing of the air remaining in the cylinder with burning and already burned gas continues throughout the combustion and expansion processes.

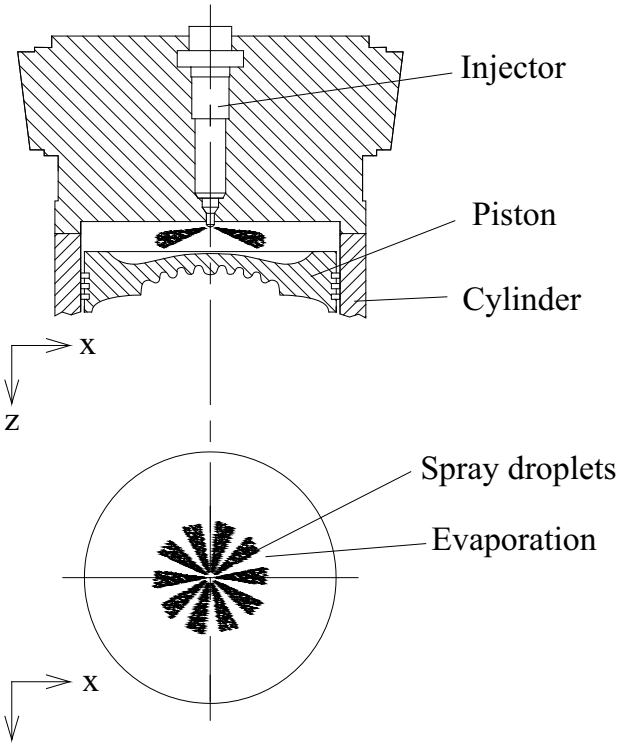

Fig. 3. Spray injection in the Wärtsilä 6L 46

Operating with gas, some marine engines employ the spark-ignited lean-burn Otto cycle. In this process the gas is mixed with air before the inlet valves and then ignited by a spark plug. The main disadvantage of this process is the risk of detonation because the auto-ignition of the mixture is difficult to control. In order to solve this problem, other marine engines are dual fuel powered and can operate in gas or fuel oil mode. Operating in gas mode, the gas is injected according to a diesel process at high pressure and is ignited by a pilot injection of diesel. These engines are more tolerant in terms of methane number than other gas engine concepts. Operating with hydrogen, both options 100% hydrogen and dual fuel are possible. Hydrogen engines also have a high risk of detonation.

NUMERICAL PROCEDURE

The engine described in the previous section was numerically simulated to analyze the emissions. Three fuels were employed, fuel oil, natural gas and hydrogen. Regarding natural gas and hydrogen, the dual fuel mode with pilot injection was simulated. A 1% amount of pilot fuel was initially employed, Wärtsilä [14], and the influence of this quantity was analyzed. The primary fuel, natural gas or hydrogen, controls the engine power output, while the pilot diesel fuel auto-ignites and creates ignition source for the surrounding gaseous fuel mixture to be burned.

The governing equations are indicated in the previous works, Lamas et al. [12] and Lamas and Rodríguez [13]. The conservation of mass, momentum and energy were solved. Since the flow inside the engine is turbulent, a turbulent model was used adding transport equations. Particularly, the k-ε turbulence model was employed. In order to account for the combustion process, species conservation equations were solved.

RESULTS

Operating with fuel oil, the mass fraction of fuel is indicated in Fig. 4. The injection of fuel takes place from -12° to -1° crankshaft angles. Fig. 4 represents -10°, -5° and 0° (top dead center). As can be seen, the mass fraction of fuel is high in the zone close to the fuel tip (-10° and -5°). After the injection of fuel has finished, the mass fraction of fuel is reduced progressively (0°).

A comparison of the fuel concentration using fuel oil, natural gas and hydrogen is indicated in Fig. 5. The -10° crankshaft angle is represented. As can be seen, hydrogen promotes the larger fuel concentration region. It releases a high amount of energy during combustion compared to both fuel oil and natural gas. Nevertheless, fuel oil has the smaller fuel concentration region, releasing a lower amount of energy. This behavior is also appreciated in Fig. 6, which indicates the in-cylinder pressure using fuel oil, natural gas and hydrogen. Hydrogen promotes higher pressures than fuel oil and natural gas while fuel oil promotes lower pressures.

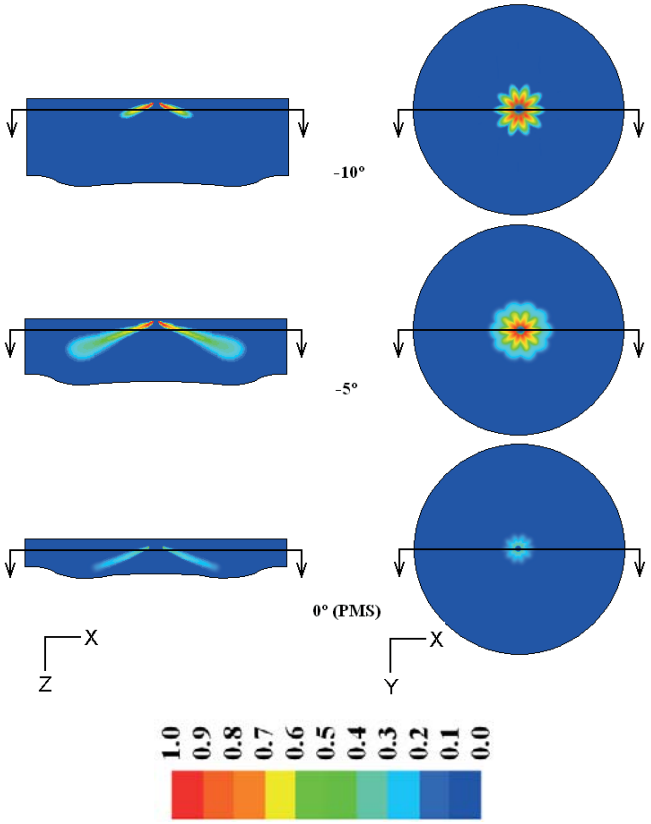

Fig 4. Mass fraction of fuel operating with fuel oil

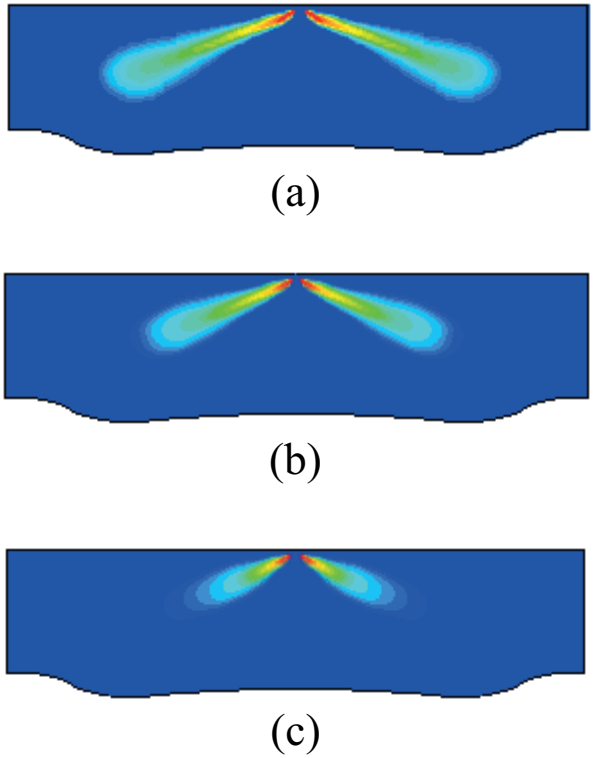

Fig. 5. Fuel concentration at -10°; (a) fuel oil; (b) natural gas; (c) hydrogen

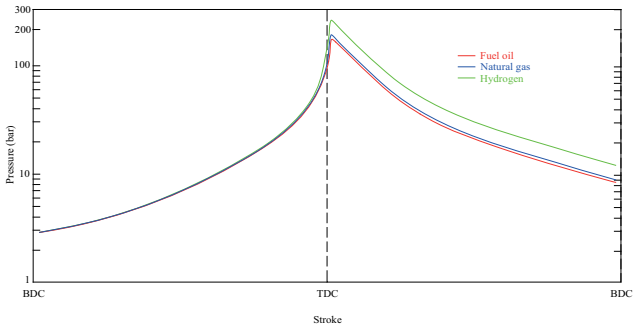

Fig. 6. In-cylinder pressure using fuel oil, natural gas and hydrogen

Regarding the temperature field, its characterization is very important to determine NO_x formation since this pollutant is strongly dependent on the temperature. Higher temperatures promote higher NO_x emissions. Table 1 indicates the maximum temperature, pressure and emissions in g/kW-h using the three fuels analyzed. As can be seen, hydrogen promotes the highest combustion temperature and thus high NO_x emissions. Nevertheless, it is too clean regarding CO_2, CO and HC. It is worth to mention that NOx is relatively easy to reduce with the current technology due to the restrictive legislation imposed in the last years. This makes hydrogen a promising fuel if the price is reduced in the next years.

Regarding fuel oil and natural gas, CO_2 and CO emissions are higher using fuel oil and HC emissions are lower. This is due to the C/H proportion, which is higher for fuel oil than for natural gas. As natural gas has a lower C/H proportion than fuel oil, HC emissions are higher and CO_2 and CO emissions are lower.

Tab. 1. Emissions, maximum pressure and maximum temperature using fuel oil, natural gas and hydrogen

	CO_2 (g/kW-h)	CO (g/kW-h)	NO_x (g/kW-h)	HC (g/kW-h)	P_{max} (bar)	T_{max} (°C)
Fuel oil	1490.4	4.08	11.8	4.66	182.3	2158.2
Natural gas	1221.2	2.41	14.7	7.61	191.3	2269.7
Hydrogen	7.45	0.008	17.2	0.011	233.4	2407.6

The most important advantage of using hydrogen is the zero CO_2 and CO emission levels. The small CO_2 and CO amount is caused by the pilot injection to ignite the mixture. Fig. 7 indicates the emissions compared to the pilot percentage, from 1 to 20%. As can be seen, increasing the pilot percentage reduces the NO_x but increases CO_2, CO and HC emissions. Regarding natural gas, emissions compared to the pilot percentage are indicated in Fig. 8. As expected, increasing the pilot percentage reduces NO_x and HC but increases CO_2 and CO.

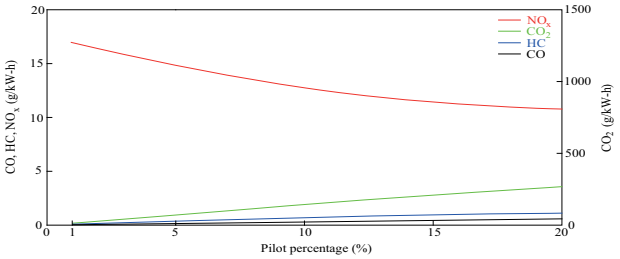

Fig. 7. Emissions against pilot percentage. Hydrogen.

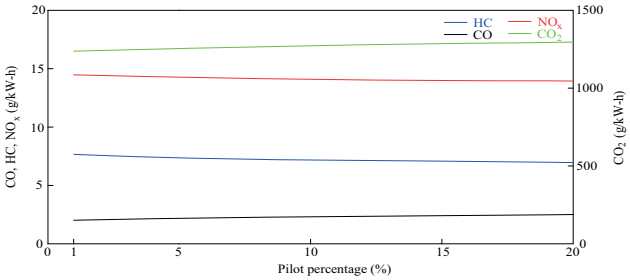

Fig. 8. Emissions against pilot percentage. Natural gas

CONCLUSIONS

Emissions from ships represent one of the main issues due to the negative impact on the environment. This paper employed a numerical model to compare three fuels in a commercial marine engine, the Wärtsilä 6L 46. Three fuels were compared: fuel oil, natural gas and hydrogen. CO_2, HC, CO and NO_x emissions were analyzed. SO_x emissions were not analyzed because these depend on the sulphur content of each particular fuel. It was found that, environmentally, hydrogen is the best option when CO_2, HC and CO emissions are considered. Nevertheless, hydrogen is too expensive and emits more NO_x than fuel oil and natural gas. Nowadays, NO_x reduction technologies have made considerable progress; still, the price constitutes an important problem to employ hydrogen in marine engines.

Natural gas is the best alternative fuel for marine applications due to its low cost, availability and adaptability for existing engines. The main disadvantage of natural gas is the risk of knocking. Natural gas can promote premature combustion and thus damaging vibrations. Fuel oil is more expensive than natural gas and emits more CO2, and CO. Besides, due to the sulphur content in the fuel, fuel oil emits more SOx than natural gas and hydrogen.

ACKNOWLEDGEMENTS

The authors would like to express their gratitude to "Talleres Pineiro, S.L.", marine engines maintenance and repair shop.

REFERENCES

1. Skjølsvik, K.O.; Andersen, A.B.; Corbett, J.J.; Skjelvik, J.M. Study on greenhouse gas emissions from ships. Final Report to the International Maritime Organization, MT Rep. Mtoo A23-038, MARINTEK, Trondheim, Norway, 2000

2. Bigos, P.; Puskar, M. Influence of cylinder shape and combustion space on engine output characteristic of two-stroke combustion engine. Zdvihací zařízení v teorii a praxi 3, 2008

3. Kontoulis, P.; Chryssakis, C; Kaitktsis, L. Analysis of combustion and emissions in a large two-stroke marine diesel engine using CFD and T-φ mapping. 18th International Multidimensional Engine Modeling User's Group Meeting at the SAE Congress. Detroit, MI, 2008

4. Panagiotis, A.; Chryssakis, C.; Kaiktsis, L. Optimization of injection characteristics in a large marine diesel engine using evolutionary algorithms. SAE Paper 2009-01-1448, 2009

5. Lamas, M.I.; Rodriguez, C.G. Emissions from marine engines and NOx reduction methods, Journal of Maritime Research, volume 9(1), pp. 77-82, 2012

6. Millo, F.; Bernardi, M.G.; Delneri, D. Computational analysis of internal and external EGR strategies combined with Miller cycle concept for a two stage turbocharged medium speed marine diesel engine. SAE Paper 2011-01-1142, 2011

7. Jayaran, V.; Nigam, A.; Welch, W.A.; Millar, J.W.; Cocker, I.I.: Effectiveness of emission control technologies for auxiliary engines on ocean-going vessels. Journal of the Air & Waste Management Association, vol 61(1), pp 14-21, 2011

8. Andreasen, A.; Mayer, S. Use of seawater scrubbing for SO2 removal from marine engine exhaust gas. Energy and fuels, vol. 21, pp. 3274-3279, 2007

9. Banawan, A.A.; El-Gohary, M.M.; Sadek, I.S. Environmental and economical benefits of changing from marine diesel oil to natural gas fuel for sort-voyage high-power passenger ships. Engineering for the Maritime Environment, vol. 224, pp. 103-110, 2010

10. Seddiek, I.S.; Elgohary, M.M. Eco-friendly selection of ship emissions reduction strategies with emphasis on SOx and NOx emissions. International Journal of Naval Architecture and Ocean Engineering, vol. 6, pp. 737-748, 2014

11. Eide, M., Longva, T., Hoffmann, P., Endresen, Ø., and Dalsøren, S.: Future cost scenarios for reduction of ship CO2 emissions. Maritime Policy & Management., vol. 38, pp. 11–37, 2011

12. Lamas, M.I., Rodríguez, C.G. and Rebollido, J.M. Numerical model to study the valve overlap period in the Wärtsilä 6L 46 four-stroke marine engine. Polish Maritime Research, vol. 19(1), pp. 31-37, 2012

13. [13] Lamas, M.I. and Rodríguez, C.G. Numerical model to study the combustion process and emissions in the Wärtsilä 6L 46 four-stroke marine engine. Polish Maritime Research, vol. 20(2), pp. 61-66, 2013.

14. www.wartsila.com

CONTACT WITH AUTHOR

Lamas, M.I.,
isabellamas@udc.es

POLISH MARITIME RESEARCH 4(88) 2015 Vol. 22; pp. 53-58
10.1515/pomr-2015-0071

INLET AIR FOGGING OF MARINE GAS TURBINE IN POWER OUTPUT LOSS COMPENSATION

Zygfryd Domachowski, Prof.
Marek Dzida, Assoc. Prof.
Gdańsk Univeristy of Technology, Poland

ABSTRACT

The use of inlet air fogging installation to boost the power for gas turbine engines is widely applied in the power generation sector. The application of fogging to mechanical drive is rarely considered in literature [1]. This paper will cover some considerations relating to its application for gas turbines in ship drive.
There is an important evaporative cooling potential throughout the world, when the dynamic data is evaluated, based on an analysis of coincident wet and dry bulb information. This data will allow ships' gas turbine operators to make an assessment of the economics of evaporative fogging. The paper represents an introduction to the methodology and data analysis to derive the direct evaporative cooling potential to be used in marine gas turbine power output loss compensation.

Keywords: marine gas turbine; ambient temperature; power output loss compensation; inlet air fogging; methodology

INTRODUCTION

The gas turbine output as well as efficiency strongly depends on the ambient temperature. For every 1^0C rise in ambient temperature, a gas turbine output drops by 0,5 − 0,9 %, and a heat rate increases about 0,2 % [2]. The detrimental effect of ambient temperature on gas turbine output and efficiency creates problems for operators of as well power generation and mechanical drive units. In hot and dry air regions, gas turbine power output is dramatically reduced because of the reduction in gas turbine air mass flow. This effect is particularly predominant with aero derivative units that are commonly used in the marine drive, see Fig. 1. Cooling the air to the wet bulb temperature will increase the density of the air, increase the air mass flow, and boost the gas turbine engine power and efficiency.

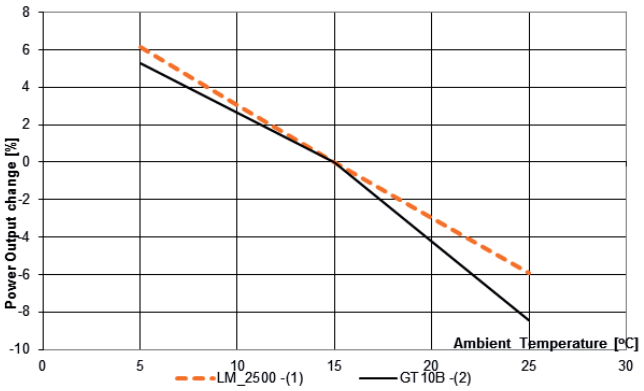

Fig. 1. Typical Temperature – Power Relation for Aero derivative Marine Gas Turbine (Two – Shaft) LM2500 (1) and Electric Power Gas Turbine GT10B (2)

To compensate a gas turbine output loss when ambient temperature rises, several inlet air cooling technologies are available. In such case, a selection of the climatic design point is of principal importance [3]. Then the choice of the gas turbine power augmentation technology depends on the following factors:

- The type of the gas turbine service.
- The cost of the fuel.
- The benefits of power augmentation.
- The variability of climatic conditions.

ELECTRIC POWER GENERATION

In the electric power generation, the gas turbine output augmentation can impact economics and /or frequency control performance of the electric power gird. Three modes of gas turbine service in the power generation can be distinguished.

- Based load, e.g. combined cycle of large power plants where additional power at any time results in additional revenue.
- Peaking service, where meeting the higher demand enables to satisfy the required frequency performance. In the same time the revenue is much higher than standard.
- Supporting wind power plants, where vagaries of the wind speed need adequate local support from conventional sources to provide limiting of the power and frequency fluctuations [5].

The design point for a gas turbine which is planned to be installed very often is the basis of design for the project in some areas. When the application of gas turbine power augmentation technologies such as evaporative cooling or mechanical chilling is assumed, then the selection of the design point is based on the use of locally collected weather data. On such basis, an accurate and appropriate analysis should be developed to compare different cooling technologies taking into account the type of project, the power demand diagram, coincident air temperature and humidity, electricity and fuel prices. Especially in hot arid areas, the cooling approaches are in use for several decades [7].

In specific location of a gas turbine, an analysis of climatic data is necessary to provide the full year sites' temperature profile. This data can be used to generate the so-called cooling „degree hours" [2] which are a measure of available cooling potential. For each hour of the year such an analysis allows a gas turbine operator to evaluate the available power gain from power augmentation. Usually several climatic data sources are available. Most of them are average (typical and representative) weather data. Most frequently, they may provide a sufficient description of an estimated value of the cooling potential in specific location.

POWER AUGUMENTION OF SHIP GAS TURBINE

The marine gas turbines offer advantages for specific ship categories such as cruise ships, fast ferries, fast cold storage vessels, general refrigerated ships, fruit carriers, packet ships, mega – yachts, naval vessels. All fast ships need prime mover operation at maximum performance parameters. Full power operation at prime mover optimal parameters results in maximum speed of a ship on one hand and environmentally friendly conditions on the other hand. The change of ambient air temperature influences prime mover performance. Voyaging at cold weather (air temperature lower than the design point), the thermal efficiency is improved. Above the design point air temperature, the thermal efficiency of a gas turbine decreases which results in power output decrease. This effect can be more severe on aero derivative engines mostly used in ship drive, Fig. 1.

For ship drive applications, when output power from the gas turbine falls on hot days, very often power output demand is high and the power margins originally designed into the driver have been exhausted. In such circumstances augmenting gas turbine power output can have an important impact on profitability.

AIR TEMPERATURE CHANGE DURING SHIP VOYAGE

Viewing an air temperature change lets us take into account separately a short, and a long sea voyage of a ship. The Baltic Sea on one hand and the Mediterranean Sea on the other can be considered for a short voyage e.g. of a ferry equipped with gas turbine.

In Fig. 2 and in Fig. 3 the air temperature on the shore of Baltic Sea in January (in winter), and in July (in summer) is represented; Fig. 4 and Fig. 5 - air temperature on the shore of Mediterranean Sea.

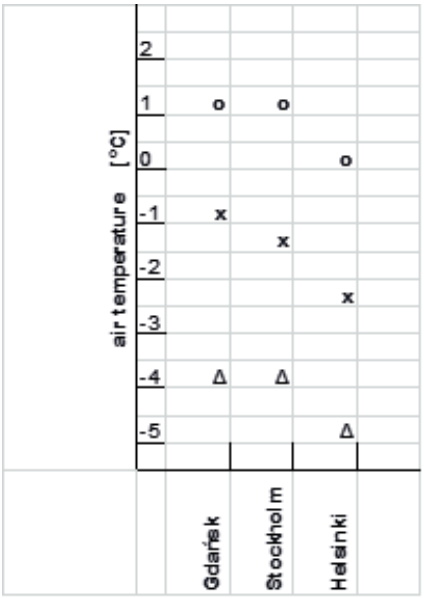

Fig. 2. Air Temperature on the Shore of Baltic Sea in January o- max; x- average; Δ- min

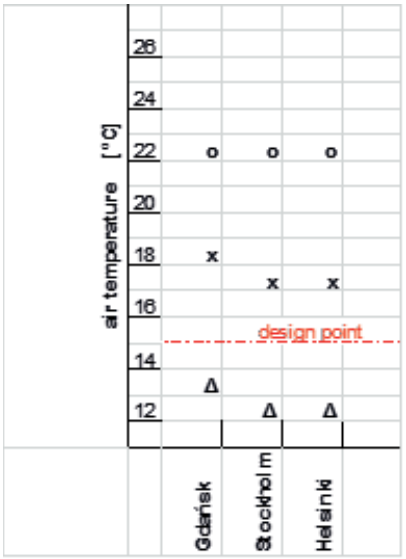

Fig. 3. Air Temperature on the Shore of the Baltic Sea in July o- max; x- average; Δ- min

For a long sea voyage consider e.g. the distance between the Baltic Sea region and the Far East area. Air temperature in several ports on such a way is represented in Fig. 6 (January) and Fig. 7 (July).

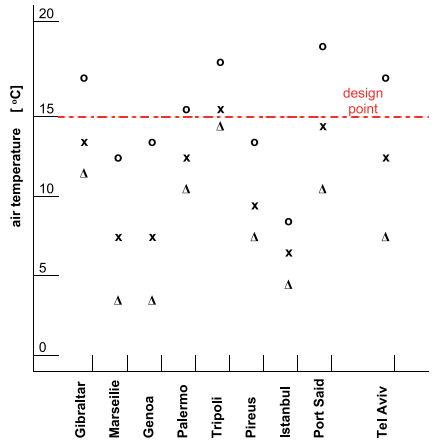

Fig. 4. Air Temperature on the Shore of the Mediterranean Sea in January o- max; x- average; Δ- min

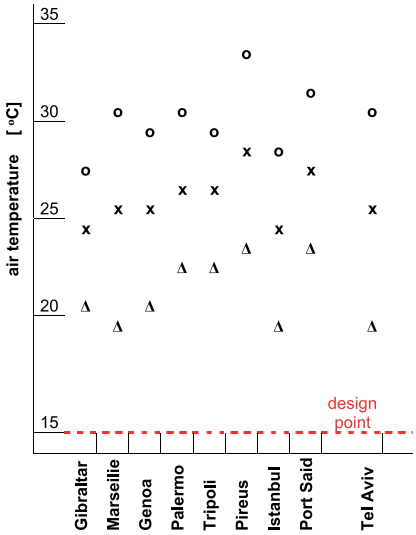

Fig. 5. Air Temperature on the Shore of the Mediterranean Sea in July o- max; x- average; Δ- min

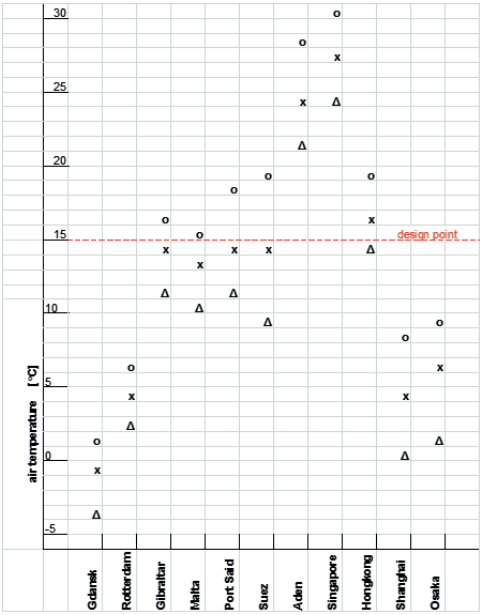

Fig. 6. Air Temperature on the way from the Baltic Sea to Far East Area in January; o- max; x- average; Δ- min

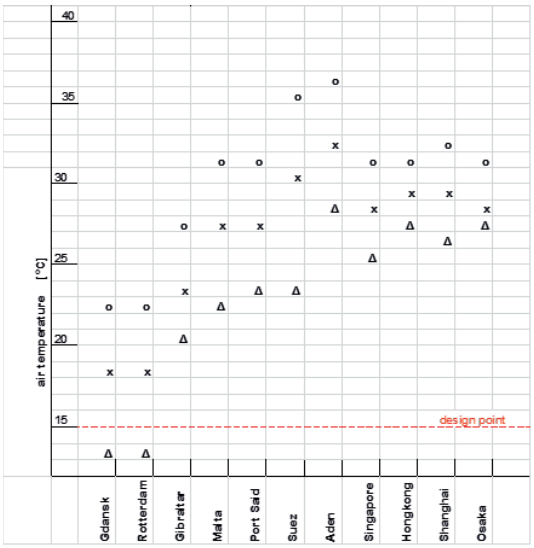

Fig. 7. Air Temperature on the way from the Baltic Sea to far East Area in July o- max; x- average; Δ- min

AIR COOLING TECHNOLOGY FOR SHIP GAS TURBINE POWER AUGMENTATION

The detriment effect of ambient temperature increase on gas turbine output and efficiency poses a significant problem in the ship drive during high demand. In such case, the use of power augmentation can reduce the dependency on ambient temperature. In the ship drive, two cooling technologies can be considered. They are: an evaporative cooling or chilling. Chilling is accomplished mainly by mechanical package chillers. In the ship use, the evaporative cooling seems to prevail over the chilling because of lighter weight and smaller bulk of additional installation.

The basic principle of evaporative cooling consists in latent heat water vaporization. When water evaporates, it cools the air at the gas turbine inlet. The effectiveness of traditional evaporative cooler can be defined as:

$$E = \frac{T_{DB} \quad T_{DB}}{T_{1DB} \quad T_{WB}}$$

where T_1 is inlet temperature, T_2 - exit temperature of evaporative cooler, DB – dry bulb, WB – wet bulb. [7]. The wet bulb temperature can never be attained. A typical value for effectiveness is 85 - 90%. The use of a media type evaporative cooler inherently involves a pressure drop in inlet duct. These drop losses result in a drop in power output and efficiency.

Direct inlet fogging is a method of cooling, where demineralized water is converted into a fog by means of special nozzles operating at 7 - 14 MPa. When compared to other technologies (media evaporative cooling and refrigeration technologies), fogging has seen large–scale application because of low first cost. This technique allows attaining effectiveness close to 100%. That means the relative humidity at the gas turbine inlet will be 100% which gives the lowest temperature possible (as the wet bulb temperature) without refrigeration.

Several weather data sources may provide a sufficient description and give an estimated value of the cooling potential in a specific location. The change of location, the change in the climate needs special treatment to quantify the impact of these effects on the weather data and consequently on the efficiency of gas turbine inlet air cooling system. The Equivalent Cooling Degree Hours (ECDH) calculations are a useful measure when inlet fogging is deployed. The cooling degree hours is a number (0^C - hours) that defines the total amount of cooling that can be derived in a given time period. The ECDH is calculated with a lower limit of Minimum Wet Bulb Temperature (MWBT) varying between 7,2 ^{0}C (450F) and 12,8 ^{0}C (550F) [2]. The MWBT is selected in order to avoid the possibility of inlet icing. The ECDH is calculated as the difference between the coincident dry bulb temperature and the wet bulb temperature multiplied by the number of hours that this difference exists if the wet bulb temperature is above the lower limit of MWBT. At a given location the ECDH number would be multiplied by the gas turbine specific kW/^{0}C cooling number to compute the kW – hours of capacity available by the use of inlet fogging. For example, if the ECDH is 10 000 degree – hours, then a gas turbine such as the LM 2500 which has the specific cooling number of approximately 134,4 kW/^{0}C, see Fig. 1, the kW – hours gained would be 10 000 0C –hrs x 134,4 kW/^{0}C = 1344000 kW – hrs.

There is a relatively large evaporative cooling potential throughout the world. It can be evaluated, based on an analysis of coincident wet bulb and dry bulb information when the climatic data is available. In [2] a detailed climatic analysis has been made of 106 major locations over the world to provide the cooling hours that can be obtained by inlet fogging. The source of data was a database published by Airforce Combat Climatology Centre. A cross check was performed with American Society of Heating and Refrigeration Engineers (ASHRE) data. The ECDH was calculated assuming a lower WBT limit of 12,8 ^{0}C (550F). This number was considered to avoid any possibility of inlet icing.

EVALUATION EXAMPLE OF THE POTENTIAL POWER GAIN FROM INLET FOGGING ON SHIP'S VOYAGE

Table 1 shows cooling hours for some ports on the shore of the Baltic Sea, on the shore of Mediterranean Sea, and on the way from Baltic Sea Area to Far East Area. Any operator of ship gas turbine can evaluate the potential for evaporative cooling per month in the region of this ship's location, based on databases such as those in Table 1. Multiplying the ECDH number by the turbine specific kW/^{0}C cooling number, it is possible to calculate the kW – hours of capacity available by the use of evaporative fogging.

On the way from Baltic Sea Area to Far East Area, there are regions of high humidity (e.g. Madras, Manila, Hong Kong areas). Therefore, it is worth to remark, that the moisture

• holding capacity of air depends on its temperature. Warmer air can hold more moisture then cooler air. This results in the conclusion, that high relative humidity generally occurs time

• coincident with the lowest temperature and the lowest relative humidity occurs with the highest temperature. Therefore, relative humidity is the highest during the cool morning and evening hours and the lowest in the hot afternoon hours. That's because even in the most humid environments, it is possible for an evaporative cooling up to 8 0C during the hotter part of the day. The sites' temperature profile for a full day of hourly data of wet and dry bulb coincident temperatures have to be considered in the analysis. On such basis, evaporative cooling degree hour (ECDH) numbers for each hour of the day can be calculated. These data allow a gas turbine operator to evaluate the potential power gain from inlet fogging.

Tab. 1. Available Monthly and Yearly ECDH in the Baltic Sea Area, the Mediterranean Sea Area, and on the Voyage from Baltic sea Area to Far East Area, Min. WBT = 12,8 ^{0}C

	Jan.	Feb.	Mar.	Apr.	May	Jun.	Jul.	Aug.	Sep.	Oct.	Nov.	Dec.	Ann.
Baltic Sea Area													
Stockholm	0	0	0	22	394	1189	2269	1786	200	10	0	0	5871
Mediterranean Sea area													
Barcelona	4	28	80	485	1361	1933	2391	2337	2015	1365	485	62	12546
Marseille	0	9	98	296	2158	3251	4212	3909	2635	1321	267	35	18192
Naples	24	9	176	728	2167	2513	3050	2941	2185	1535	491	126	15945
Venezia	0	0	14	313	1869	2285	2802	2665	1785	731	44	1	12508
Khania (Crete)	49	55	213	1367	3451	4887	5192	4931	3848	2616	1190	364	28161
Istanbul	0	0	013	364	1776	2995	3413	3270	2696	1402	290	0	16220
Beirut	278	476	1236	2397	2623	2815	3062	3076	3608	3552	2608	988	26717
Tel Aviv	325	434	1436	2708	2689	2679	2846	3125	3272	3280	2659	997	26449
Tripoli	244	620	1710	3030	4602	4993	5087	4954	4274	3582	2103	786	35984
Tunis	222	283	721	1348	2687	3508	4216	3998	3078	2240	1324	541	24166
Voyage from Baltic Sea Area to Far East Area													
Stockholm	0	0	0	22	394	1189	2269	1786	200	10	0	0	5871
Oslo	0	0	0	11	333	1300	2482	2035	165	1	0	0	6328
Amsterdam	0	0	4	93	686	1110	1565	1675	759	201	9	0	6104
Lisbon	110	151	549	992	1855	2744	3542	3543	2990	1745	661	244	19127
Tripoli	244	620	1710	3030	4602	4993	5087	4954	4274	3582	2103	786	35984
Aleksandria	602	730	1336	2609	3061	3043	2916	3122	3266	3051	2412	1313	27462
Madras	2485	2497	3030	3066	4177	4704	3928	3645	2899	2279	1937	2276	36921
Singapore	1595	1498	1708	1402	1439	1485	1546	1632	1377	1428	1040	1162	17313
Manila	2462	2567	3251	3378	3096	2295	2008	1860	1729	1908	2063	2219	28836
Hongkong	1529	1299	1531	1735	1945	2106	2406	2447	2736	3300	3004	2184	26221
Shanghai	2	47	109	894	1991	1669	1889	1938	1911	1804	587	54	12894
Pusan	0	8	8	585	2025	1815	1507	2041	2265	1922	307	10	12494
Osaka	0	7	38	999	2681	2817	2897	3389	2811	2082	533	16	18271

CONTROL SYSTEM OF INLET AIR FOGGING

A typical inlet air fogging system for gas turbine application consists of a series of high – pressure reciprocating pumps providing demineralized water to an array of fogging nozzles installed in the inlet air duct. Each high – pressure pump is connected to a fixed number of fog nozzles representing one discrete capacity of fog cooling, see Fig. 8. The pumps can be turned on or off sequentially to control the amount of cooling water.

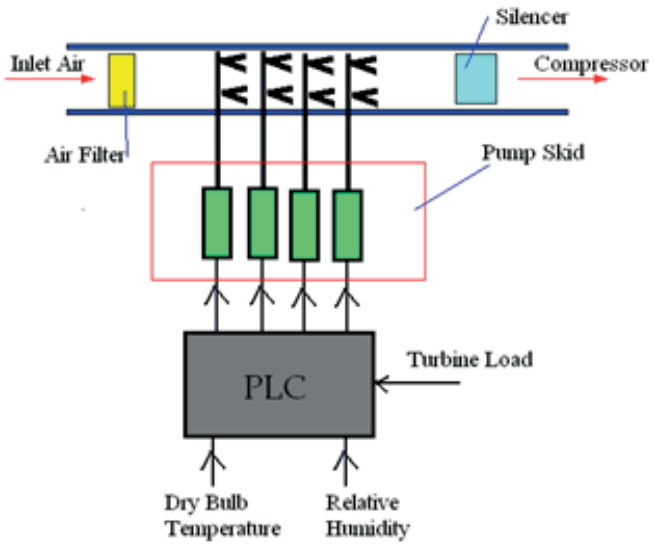

Fig. 8. Gas Turbine Inlet Fogging Control System

Fore chosen pump displacements, it is possible to obtain several cooling stages by the utilization of different pump combinations [7,8]. For example, using four pumps, one rated at 0,5 m^3/h and three at 1 m^3/h, seven cooling stages are possible, see Table 2.

Tab. 2. Seven cooling stages utilizing one pump at 0,5 m^3/h and three at 1 m^3/h, + mean pump unit "on".

Cooling stage	Pump number				Flow m^3/h	Cooling ^0C
	1	2	3	4		
1	+				0,5	3
2		+			1,0	6
3	+	+			1,5	9
4		+	+		2,0	12
5	+	+	+		2,5	15
6		+	+	+	3,0	1□
□	+	+	+	+	3,5	21

In this example, as the day temperature increases, a 9 ^0C drop in temperature may be managed in three cooling increments, see Table 3. Each stage is activated for 30 ^0C cooling. Smaller increments would require more stages.

Tab. 3. Example of Fog Cooling Stage Control (Three Stages of 30 ^0C Each)

Time	Dry Bulb Temperature	Wet Bulb Temperature	Depression	Stage "on"	Cooling	Overcooling
9:00	21 ^0C	20 ^0C	1 ^0C	None		1 ^0C
10:00	24 ^0C	20,5 ^0C	3,5 ^0C	1	3 ^0C	2 ^0C
11:00	27 ^0C	21 ^0C	6 ^0C	2	6 ^0C	2,5 ^0C
12:00	30 ^0C	21 ^0C	9 ^0C	3	9 ^0C	2 ^0C

The sites' temperature profile for a full day of hourly data of wet bulb and dry bulb temperatures, and by the same of wet temperature depression, depends on the region in the world, on the month, and day. Table 4 shows examples of numbers of ECDHs for which certain wet bulb depression ranges are available in several ports in the voyage from Baltic Sea Area to Far East Area. The ranges are selected in groups of 0 - 50 ^0C, 10 - 15 ^0C, 15 - 200 ^0C, and > 20 ^0C. The numbers provide information on the availability of cooling in different regions of the world.

Tab. 4. Availability of ECDH of a Range of WBD (^0C) in the Voyage from Baltic Sea Area to Far East Area Min. WBT = 12,8 ^0C

	0-5	5-10	10-15	15-20	>20
Stockholm	2066	3783	125	0→	0→
Oslo	1385	4461	309	0→	0→
Amsterdam	4558	1600	55	0→	0→
Lisbon	9572	8067	1943	113	0
Tripoli	8311	16585	8366	3148	105
Aleksandria	14453	12240	380	116	2
□adras	14881	17874	3495	205	0
Sin□apore	14181	4068	0	0	0
□anila	20330	8247	13	0	0
□on□kon□	23809	2082	0	0	0
Shan□hai	10938	1906	8	0	0
□□san	11968	550	0	0	0
Osaka	9931	8428	104	0	0

The temperature and humidity sensors are provided to measure ambient relative humidity and dry bulb temperature. These measured parameters are used to compute the ambient wet bulb temperature and the difference between dry bulb and wet bulb temperature (the depression) to calculate and control the amount of evaporative cooling. This is the role of programming algorithms in the Programmable Logic Controller (PLC) mounted on the high - pressure pump skid, see Fig. 8.

To implement inlet fogging, very little modification of the gas turbine, an inlet air system is needed. The most applied location for the high – pressure fog nozzle manifolds is the downstream of the air – filter. This option for installing the inlet fogging allows for moreover fog intercooling. In such, case the control system supplies a greater quantity of water that can be evaporated prior to the compressor inlet. The excess fog is brought into the compressor. This creates a compressor intercooling effect, see the last column in Table 3, which is boosts the gas turbine power output considerably.

Any marine gas turbine operates at a range of loads. Therefore, the gas turbine load should be an input to the PLC, see Fig.8. The PLC algorithms would then adjust the amount of fog injection in proportion to the inlet air mass flow.

ECONOMIC ASSUMPTION OF INLET AIR FOGGING APPLICATION

On one hand, to implement inlet fogging, very little modification of the inlet air system is needed. On the other hand the decision to apply inlet air fogging is an economic one. The following factors should be taken into account in a feasibility study:

- Climate profile of a ships' voyage,
- Cost of the cooling system to be installed,
- Amount of MW-h boost gained over a year by means of inlet air cooling, and what benefit is attained as the result of it,
- Parasitic power used, and the effect of increased inlet pressure drop (which is almost nil), and the cost of the demineralized water,
- Projected O&M costs for the inlet fogging system,
- Potential environmental impact.

CONCLUSION

In ship drive applications, the gas turbine power output drops on hot days. Very often, power demand is high. In such circumstances augmenting gas turbine power output has an important impact on ship's voyage economics.

The dependency of marine gas turbine on the ambient temperature (power output and efficiency drops with ambient temperature increase) makes inlet air fogging an effective gas turbine power compensation. Power augmentation is a result of water direct evaporation. By this means, the wet bulb temperature is attained at the inlet of compressor. Then, further enhancement of gas turbine power can be attained by fog intercooling. Water excess in form of micron size particles enters compressor. This causes reduction of the gas turbine compressor work.

An investigation has been conducted in order to examine the applicability of inlet air fogging in marine gas turbines. Different areas of ship's voyage have been taken into account. The use of inlet air fogging in marine gas turbines must be evaluated based on the gas turbine characteristics, climate profile of ship's voyage, and expectations of gas turbine power augmentation.

REFERENCES

1. Al – Amiri, A. M., Zamzam, M.M., Chaker, M.A., Meher – Homji, C. B., "Application of Intel Fogging for Power Augmentation of Mechanical Drive Turbines in the Oil ana Gas Sector", Proceeding of ASME Turbo Expo 2006: Power for Land, Sea and Air, May 8-11, 2006, Barcelona, Spain, ASME Paper GT 2006 – 91054.
2. Chaker, M.A., Meher – Homji, C. B., "Inlet Fogging of Gas Turbine Engines: Climatic Analysis of Gas Turbine Evaporative Cooling Potential of International Locations", Proceedings of ASME Turbo Expo 2002, June 3-6, 2002, Amsterdam, The Netherlands, ASME Paper 2002 – GT – 30559.
3. Chaker, M.A., Meher – Homji, C. B., "Selection of Climatic Design Points for Gas Turbine Power Augmentation", Proceedings of ASME Turbo Expo 2011, June 6-10, 2011, Vancouver, British Columbia, Canada, ASME Paper GT2011-46463.
4. Domachowski, Z., "An Impact of Ambient Parameters Change on Steam and Gas Turboset Control", Transactions of the Institute of Fluid - Flow Machinery, No 113, 2003.
5. Domachowski, Z., "Counteracting Windpower Fluctuations within a Separate Electric Power Grid", Proceedings of ASME Turbo Expo 2007: Power for Land, Sea and Air, May 14-17, 2007, Montreal, Canada, ASME Paper GT 2007-28218.
6. Domachowski, Z., Dzida, M., "An Impact of Environmental Disturbances on Combined Cycle Power Plant Control", Proceedings of ASME Turbo Expo 2004: Power for Land, Sea and Air, June 14-17, 2004, Vienna, Austria, ASME Paper GT 2004 – 54057,
7. Meher – Homji, C. B.,Mee, T. R., "Gas Turbine Power Augmentation by Fogging of Inlet Air", Proceedings of the 28th Turbomachinery Symposium, Turbomachinery Laboratory, Texas A&M University, September 1999, Houston, USA.
8. Meher – Homji, C. B., Mee, T. R., "Intel Fogging of Gas Turbine Engines, part B: Practical Considerations, Control and O&M Aspects, Proceedings of ASME Turbo Expo 2000, May 8-11, 2000, Munich, Germany, ASME Paper 2000 – GT-308.

CONTACT WITH AUTHOR

Zygfryd Domachowski
Marek Dzida

Gdansk University of Technology
Faculty of Ocean Engineering and Ship Technology
Narutowicza 11/12 St.
80-288 Gdańsk
Poland

POLISH MARITIME RESEARCH 4(88) 2015 Vol. 22; pp. 59-63
10.1515/pomr-2015-0072

THE INFLUENCE OF MANUFACTURING OVERSIZING ON POST-WELDING DISTORTIONS OF THE FILLET WELDED JOINT

Janusz Kozak, Assoc. Prof.
Jakub Kowalski, Ms. C.
Gdańsk Univeristy of Technology, Poland

ABSTRACT

Welding proces is basic joining technique in shipbuilding. Such method generated welding distortions which cause a lot of problems during the manufacturing process. In the literature it is proposed wide spectrum of suggestions for a correct estimation of welding deformation in particular angular deformation in the fillet welded T joint. In the work influence of oversizing of weld on angular distortions of joint is presented basing upon of the results of the laboratory measurements. Values determined on the basis of literature hypotheses are compared with the one obtained from the laboratory test.

Keywords: welding distortion; shipbuilding welding; welding angular distortion

INTRODUCTION

The welding process is nowadays a dominating method used to connect permanently steel structures. It consist in melting edges of the parent material of selected structure elements using a heat source, such as electric arc, plasma beam, laser, etc. Regardless of the applied method, a portion of thermal energy is introduced to the material during welding. This thermal energy initiates various processes of structure distortion, with the resultant changes in dimensions and shapes of the connected elements.

Welded T-joints compose a large portion of all joints in the metal watercraft hull structure. Their total length in a large watercraft unit can reach many kilometres. Fig. 1 shows sample joints of this type applied in the ship structure.

Fig. 1. Typical T-joints in ship structure

In the context of the above considerations, minimising post-welding distortions is of high importance and should be taken into account in both the design and production process. It can considerably simplify and accelerate the production process, as well as decrease the costs and time of possible repairs by reducing the scale of distortions. However, actions oriented on minimising post-welding distortions require information concerning mechanisms of their formation and possible scale of appearance.

A common practice among both designers of welded structures, and welders performing fillet joints in shipyards, is oversizing of welds. At the ship design stage, the weld dimension resulting from strength calculations is most frequently rounded up to an integer millimetre value. At the production stage, in turn, the design dimension is exceeded in fear that the undersized weld will not be accepted by inspection authorities. All this leads to the increase of joint distortion caused by larger amount of introduced heat, with simultaneous increase of total mass of the structure caused by excessive amounts of metal in the weld.

The paper discusses the effect of weld oversizing on the resultant angular post-welding distortions. Results of theoretical calculations making use of two analytical-empirical formulas which can be found in the literature are included, along with their confrontation with the experiment.

EXPERIMENTAL ASSESSMENT OF ANGULAR POST-WELDING DISTORTIONS OF THE HULL FILLET JOINT

To assess the effect of fillet weld oversizing in the welded T-joint on angular distortion of plating plates, a series of successively oversized joints were prepared as specimens for further tests during which process parameters and the formed distortions were recorded. The selected joint structure was a modification of a typical node of ship's structure, and the dimensions of the weld were assumed based on PRS Regulations, part II – Hull [1]. The experiment consisted in assessing the angular distortion of the joint during and after welding the bulb stiffener to the plate of normal strength ship steel, category A, for successively increasing weld dimensions "a" (Fig.1) against the nominal dimension of 4mm required by the Regulations [2].

The idea and dimensions of the examined model and the research rig are shown in Fig. 2, along with the illustration of the way in which the measurements were performed.

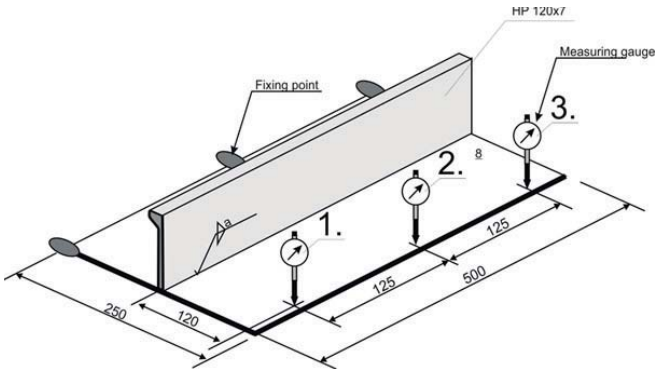

Fig.2. Scheme of the model and the research rig

During welding, the elements were immobilised using tack welds between the plating and the stiffener, while the specimen was fixed to the welding table (Fig.3). The welding process was executed following the welding procedure (WPS) for the welding method 136 – FCAW (Flux-Cored Arc Welding), approved by PRS. The welds were made by a shipbuilding welder with more than dozen-year experience and qualifications certified by the Polish Register of Shipping.

The joint preparation procedure, the weld geometry, the welding sequence, and the process parameters are given in Table I.

All basic process parameters were recorded during welding, including: arc voltage U – [V], welding current I – [A] and time of welding [min]. During laboratory tests the welding wire G464MG3Si was used as a replacement for the wire suggested in WPS: minimum yield strength 460 MPa, minimum elongation 20 %.

The angular distortion was measured using dial gauges, type M2 TOP (Fig.3).

Tab. 1. Welding Procedure Specification (WPS) [3]

Welding Procedure Specification for test joint								
Method of preparation	Oxy cutting &grinding			Material thickness	t=7[mm]			
Joint preparation				Welding sequence				
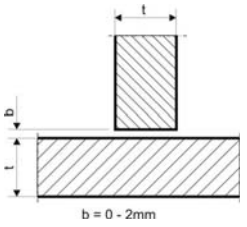				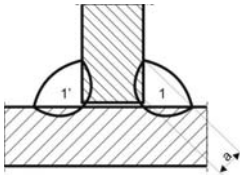				
Process	Run	Size of electrode [mm]	Current [A]	Voltage [V]	Current Polarity	Wire feed speed [m/min]	Weld speed [cm/min]	Heat input [kJ/cm]
PA,PB	1+	F1,2	190-240	23-27	DC(+)	6,5-10,0	16-23	9,1-19,5
Shielding gas			EN ISO 14175:M21		Gas flow rate		18-22 [l/min]	
Filler material			T464ZPMIH5		Preheating temperature		Min. 10^{0}C	

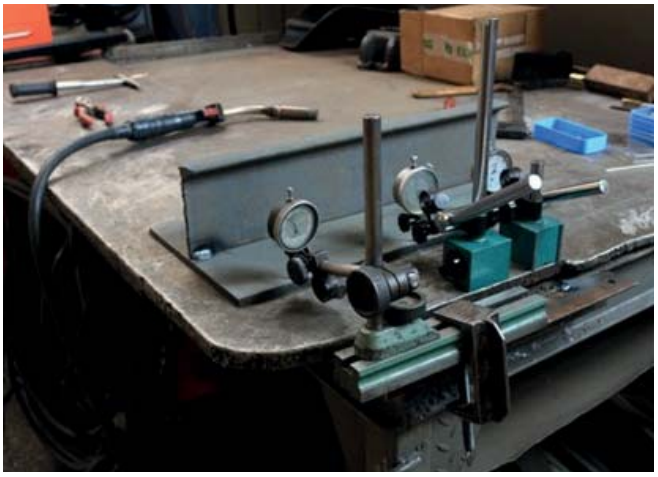

Fig.3. Model on the research rig [3]

After welding the size of the weld was measured, and these real dimensions of the weld were used for further analysis. The results of the performed tests are collated in Table 2.

Tab. 2. Results of performed tests [3]

	weld run No 1				weld run No 1`			
Spec. No	Current	Voltage	speed	gauge 2	Current	Voltage	speed	gauge 2
	I	U	v	δ_2	I	U	v	δ_2
	[A]	[V]	[m/min]	[mm]	[A]	[V]	[m/min]	[mm]
1-1	184	27,5	0,23	1,73	175	27,7	0,23	4,71
1-2	172	26,7	0,27	1,60	173	26,5	0,27	4,90
1-3	185	26,5	0,30	1,97	174	26,8	0,30	4,98
1-4	182	26,7	0,33	1,71	181	27,2	0,33	4,41
1-5	185	26,9	0,29					
2-1	190	27,4	0,22	2,72	187	27,4	0,22	5,60
2-2	189	27,4	0,25	2,68	183	27,4	0,25	5,85
2-3	188	25,7	0,19	2,35	179	26,1	0,19	5,38
2-4	180	25,3	0,20	2,50	165	25,5	0,20	5,41
2-5	165	25,8	0,20	2,31	158	26,0	0,20	4,81
3-1	174	27,5	0,21	2,15	170	27,5	0,21	5,57
3-2	185	29,5	0,25	2,32	190	29,5	0,25	5,51
3-3	188	29,4	0,25	1,89	180	29,2	0,25	5,04
3-4	187	29,2	0,26	1,90	184	29,4	0,26	5,21
3-5	188	28,9	0,26	1,62	183	29,0	0,26	4,71

where:

Spec. No – series and number of specimen in the series (1-4 – means: series one, specimen four). One series collected specimens with the same nominal dimension of the weld: 1 – 4,0 [mm], 2 – 4,5 [mm], 3 – 5,0 [mm],

Speed – v – weld speed [m/min], calculated from the measured time of welding

δ2 – relocation of the welded plate, measured using the dial gauge at the measuring point 2 (Fig. 2) [mm],

weld run – number of weld, as indicated in WPS (Table 1)

Further analyses were performed using the results averaged over the entire series of specimens, which were recorded at the measuring points situated at the midpoint of the weld (points 2). These results were assumed not to be burdened with the joint edge effect – Table 3 – averaged values.

Tab. 3. Recalculated results of performed tests

	weld run No 1			weld run No 1`			
Spec. No	weld size	heat input	angle	weld size	heat input	angle	error
	a	ql	β	a	ql	β	±Δβ
	[mm]	k[J/cm]	[°]	[mm]	[kJ/cm]	[°]	[°]
1-1	4,00	12,95	0,83	4,00	12,41	2,25	0,01
1-2	4,00	10,10	0,76	4,00	10,09	2,34	0,01
1-3	3,50	9,81	0,94	3,50	9,33	2,38	0,01
1-4	3,50	8,75	0,82	3,50	8,86	2,10	0,01
1-5							
2-1	5,50	13,95	1,30	5,50	13,73	2,67	0,01
2-2	4,00	12,53	1,28	4,00	12,14	2,79	0,01
2-3	4,00	14,88	1,12	4,00	14,39	2,57	0,01
2-4	3,50	13,75	1,19	3,50	12,71	2,58	0,01
2-5	4,00	12,85	1,10	4,00	12,40	2,30	0,01
3-1	5,50	13,68	1,03	5,50	13,37	2,66	0,01
3-2	5,50	13,10	1,11	5,50	13,45	2,63	0,01
3-3	4,50	13,27	0,90	4,50	12,61	2,41	0,01
3-4	5,00	12,45	0,91	5,00	12,33	2,49	0,01
3-5	5,00	12,49	0,77	5,00	12,20	2,25	0,01

where:

weld size – measured real dimension of the weld for the given run [mm],

heat input – calculated linear energy of welding for the recorded parameters U, I, and v, [kJ/cm]

β2 –angular distortion calculated at the measuring point 2, [°],

error – accuracy of the distortion angle calculated using the total differential method for the following reading accuracies of the recorded parameters:

dial gauge accuracy: ±0,01 mm,
dial gauge reading accuracy: ±0,005 mm,
measuring accuracy of the dial position with respect to the specimen axis: ±0,5 mm,

The distortion angles at the specimen midpoint as a function of weld thickness are shown in Fig. 4, which additionally includes the regression line in the polynomial form.

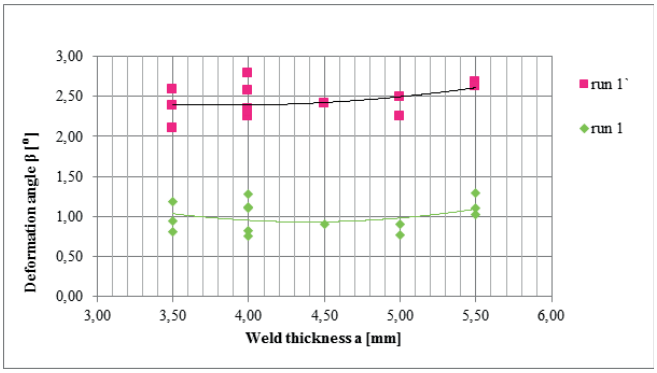

Fig. 4. Angular distortions β vs. weld thickness for both runs

THEORETICAL PREDICTION OF ANGULAR DISTORTION

Theoretical prediction of welding distortion can be performed based on analytical/empirical formulas, or can make use of the finite element method applied to thermal processes taking place during welding [4,5,6,7,8]. Modelling with the aid of the finite element method can be performed using general-purpose codes, such as FEMAP, ANSYS, SYSWELD, or dedicated programmes, such as Simufact. Welding, for instance [9]. The computer methods enable to simulate more precisely the welding process and, consequently, deliver results burdened with smaller errors. On the other hand, they are more difficult to perform than the analytical formulas and require much more detailed knowledge on the process to model it correctly and precisely.

The papers involved in seeking for analytical/empirical formulas to model welding distortions include: the works by Watanabe – Satoh [10], the Masubushi method [11], and the approach proposed by Blodgett [12]. In those methods the joint distortion angle is calculated using process parameters which are easy to obtain at the engineering calculation level. Some of those methods have been verified in relevant experiments [13].

The Watanabe – Satoh method [10] calculates the angular distortion of the fillet joint based on welding voltage and current, weld speed, electric arc efficiency, thickness of the sheet and electrode diameter. The following formula is applied:

$$\Phi = C_1 \left(\frac{I}{h\sqrt{vh}}\right)^{m+1} \cdot exp\left(-C_2 \cdot \frac{I}{h\sqrt{vh}}\right) \quad (1)$$

$$C_1 \propto \left(\frac{\eta V}{D^{0,25}}\right)^{2,5} \quad (2)$$

$$C_2 \propto \frac{\eta V}{D^{2,25}} \quad (3)$$

where:
Φ-specimen distortion angle
I-eletric current [A]
h-plate thickness [cm]
v-weld speed [cm/s]
η-heatign efficiency coefficient [-]
D-electrode diameter [cm]
V-voltage [V]

The coefficients m, C1 and C2 depend on the applied electrode. The heating efficiency coefficient for MIG method based welding ranges between 0,45 – 0,65.

The Blodgett method [12], in turn, takes into account the weld thickness a [mm], which is an important parameter from the point of view of the present analysis. Here, the angular distortion is calculated from the formula:

$$\beta_f = 0{,}053 \frac{b_f a^{1,3}}{{t_f}^2} \ [^0] \tag{4}$$

where:
b_f-plate width [mm]
a-weld thickness [mm]
t_f-thickness of the welded plate (face)[mm]

The method proposed in [14] assumes that when welding the T-joint, its angular distortion is a combined effect of plate deflection initiated by uneven transverse contraction along the plate thickness, and deflection caused by the contraction of the melted weld metal. The mechanism of angular distortion in the T-joint is shown in Fig.5.

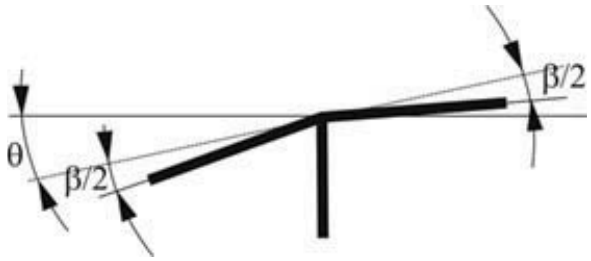

Fig.5. Mechanism of angular distortion in T-joint adopted in the method [14]

When laying the first weld, the face rotates by the angle Θ with respect to the initial position, as a result of weld metal contraction. Moreover, uneven transverse contraction along the face thickness leads to its bending by the angle β1 with respect to the undeformed face plane. The angle Θ only slightly depends on welding parameters and its value can be assumed equal to 0,02÷0,024 rad (1,2÷1,5°). For the case of free deformation of the face the angle β1 is determined, from the diagram in Fig.6, as a function of process energy per weld surface unit. In this case the calculated thickness g0 is assumed equal to the face thickness gp, and the calculated value of linear energy is obtained from the formula:

$$q_{l_0} = q_l \frac{2g_p}{2g_p + g_s} \tag{5}$$

where: g_p- thickness of the face in cm, g_s- thickness of the rib in cm.

The proposed approach [15] assumes that the size of angular distortions depends primarily on the ratio of thickness a of the fillet weld to the plate thickness g (Fig.7). In case of a thin plate, of g = 6 mm for instance, angular distortions are small because the temperature gradients across the plate thickness are small. The largest angular distortions are observed for plate thicknesses of 8 ÷ 10 mm. For larger plate thickness and small a/g ratio, angular distortions are small. The gap between the web and the plate leads to the increase of angular distortions.

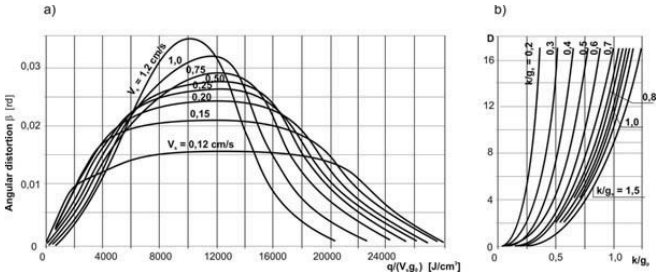

Fig.6. Nomograms: a) for assessing angular distortion β when welding butt welds and T-joints, as functions of welding conditions q, v_s, and calculated plating thickness q_0, b) for assessing the coefficient D [14]

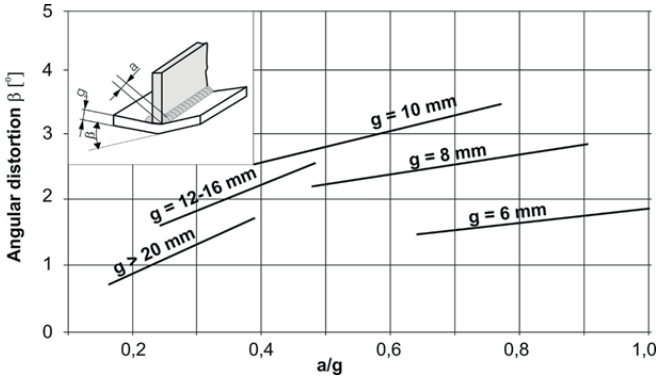

Fig.7. Angular distortions of plates caused by fillet welds [15]

The angular distortions calculated using the above method for the averaged data recorded in the experiments for weld dimensions a=3,75[mm], 4,20[mm] and 5,10[mm] were equal to, respectively: 2,25°, 2,32° and 2,47°.

Tab. 4. Compares experimental results with those calculated based on [15]

Lp.	a_b	β_{exp}	β_{ObBl}
	[mm]	[°]	[°]
1	3,75	2,27	2,25
2	4,2	2,58	2,42
3	5,1	2,49	2,47

The data in Tab. 4 reveal that the nature of weld distortion angle changes calculated using the procedure given in the literature [15] differs from that recorded experimentally. While the theoretically calculated distortion angles are in linear relation with the weld size, the relation recorded experimentally is not linear.

CONCLUSIONS

Predicting welding distortions is an important part of structure design and building. When welding, arbitrary weld oversizing by as little as a few tenth of a millimetre may lead to distortion increase by over ten percent.

For real weld thicknesses a={3,75 mm; 4,20 mm; 5,10 mm}, the angular distortions which were experimentally recorded in successive tests of the examined joint were equal to $\beta \approx \{2{,}27^0; 2{,}58^0; 2{,}49^0\}$. These results reveal that weld oversizing leads to the increase of angular welding distortions. However, this relation is not linear. Correctness of formulas, in particular for larger weld thicknesses ($a \geq 5$ mm), requires further experimental examination. For two-side multi-pass fillet welds, an additional factor which can affect angular distortions and which is not taken into account in the above quoted analytical formulas is the sequence of laying of successive weld metal layers (runs). Future numerical analyses, followed by their further experimental verification, would allow to model the effect of welding sequence and weld oversizing on the size of the resultant angular distortions.

Comparing angular distortions β recorded experimentally with those obtained from calculations reveals that the quoted engineering method slightly underestimates the angular welding distortion, and that the obtained theoretical relation is linear.

The experimental results were recorded on specimens welded in laboratory conditions. Consequently, the behaviour of the full-size structure and the effect of scale in selected calculation methods could not be taken into account and need further examination.

BIBLIOGRAPHY

1. PRS Regulations, Principles for Welding Procedure Qualification Tests, Publication no. 74/p, 2007 (in Polish).
2. PRS Regulations, pt II Hull, 2014 (in Polish).
3. Wierzbicka : Overview and verification of formulas used to estimate angular distortions in a T-joint. Diploma thesis, Gdansk University of Technology, Faculty of Ocean Engineering and Ship Technology, 2014 (in Polish).
4. K. Ferenc, J. Ferenc: Welded structures – Joint design, Wydawnictwo Naukowo-Techniczne, Warsaw 2000 (in Polish).
5. Czajkowski H., Jakubiec M., Lesiński K., Technology of welded structures, Warsaw 1987 (in Polish).
6. Sędek P., Welding stresses and distortions, [in:] Engineer's guidebook, Welding, t. I, ed. J. Pilarczyk, Warsaw 2003, pp. 559 -597 (in Polish).
7. Gourd L.M., Principles of welding technologies, transl. by N. Gawroniak, Warsaw 1997 (in Polish).
8. Predictive formulae for weld distortion – a critical review, Abington Publishing, 1999, ISBN 185573 444 3.
9. http://www.simufact.de/en/solutions/sol_weld.html (05.04.2014).
10. G. Jung, Plasticity-Based Distortion Analysis For Fillet Welded Thin Plate T-Joints, Dissertation, The Ohio State University 2003.
11. Ye Zhou, Analysis of Welding Distortions using Qualitative and Semi-quantitative Techniques, The University of British Columbia, 1998.
12. R.W.O'Brien, Predicting weld distortion in the design of automotive components, Durham theses, Durham University (2007). Available at Durham E-Theses Online: http://etheses.dur.ac.uk/2462/.
13. Kozak, J.Kowalski, Problems of Determination of Welding Angular Distortions of T-fillet Joints in Ship Hull Structures, Polish Maritime Research, ISSN: 1233-2585, 2015, vol.22, No2(86), 79-85
14. Czajkowski H., Jakubiec M., Lesiński K., Technology of welded structures, Warsaw 1987 (in Polish).
15. Engineer's guidebook: welding. T. 1., Wydawnictwa Naukowo-Techniczne, Warsaw 2003 (in Polish).

CONTACT WITH AUTHOR

Janusz Kozak
Jakub Kowalski

Gdansk University of Technology
Faculty of Ocean Engineering and Ship Technology
Naurutowicza 11/12 St.
80-233 Gdansk,
Poland

phone: +48 58 3471735
e-mail: kozak@pg.gda.pl

POLISH MARITIME RESEARCH 4(88) 2015 Vol. 22; pp. 64-69
10.1515/pomr-2015-0073

THERMOGRAPHIC METHOD BASED ACCELERATED FATIGUE LIMIT CALCULATION FOR STEEL X5CRNI18-10 SUBJECTED TO ROTATING BENDING

Adam Lipski, Ph.D.
University of Science and Technology in Bydgoszcz, Poland

ABSTRACT

The article presents an accelerated method for fatigue limit calculation which makes use of constant temperature increase rate observed in the middle time interval of specimen fatigue loading. The examination was performed on specimens prepared from drawn rods made of corrosion resistant austenitic steel X5CrNi18-10 (1.4301) subjected to rotating bending. For comparison purposes, the fatigue limit was also calculated with the aid of the Staircase method, using 30 specimens and assuming the base number of cycles equal to 10·106. Three specimens were used for accelerated examination during which their temperature was measured with the aid of the thermographic camera CEDIP Silver 420M (FLIR SC 5200). The applied loads were gradually increased until specimen damage took place. Based on the analysis of temperature changes during specimen loading, the average rate of temperature increase at successive loading stages was assessed. The obtained results were then approximated using the 2-nd order curve and its minimal value was assumed as corresponding to the fatigue limit. The performed statistic test has revealed that the fatigue limit calculated in the above way does not differ substantially from that determined using the Staircase method.

Keywords: fatigue limit; reversed bending; IR thermography; Staircase method

INTRODUCTION

The nominal stress concept based fatigue analysis is a basic element of fatigue life evaluation of structural elements, including those composing ship structures [1]. An important component of this analysis is construction of the S-N (Wöhler) curve for the examined material or structural element, and the basic parameter of this curve, in turn, is the fatigue limit. It is also an important parameter when determining the fatigue life based on cumulative damage hypotheses [2], or performing multiaxial strength criteria based calculations to assess the normal stress/shear stress relation [3] or the effect of disproportional load [4].

A standard and globally acknowledged method to determine the fatigue limit is the Staircase method (*British Standard Institution* - BS 3518 *Methods of fatigue testing. Part 5: Guide to the application of statistics*; *L'association Francaise de Normalisation* - NF A 03-405 *Essais de Fatigue*, *Japan Society of Mechanical Engineers* (JSME) - JSME S 002-81 *Standard Method of Statistical Fatigue Testing*). This method is used for direct calculation of the average value and standard deviation of the fatigue limit [5][6][7]. However, it requires long-lasting fatigue tests performed on tens of specimens until the base number of cycles, ranging from $2 \cdot 10^6$ (in tests of structural elements) to 100·106 (when testing material properties of non-ferrous metal alloys), is obtained, or the specimen is earlier damaged. For instance, when testing a single steel specimen subjected to periodic tension/compression loads (cycle asymmetry coefficient $R = 1$) at the loading frequency $f = 10$ Hz, which is a standard frequency obtained on hydraulic strength machines, the base number of 10·106 cycles is obtained after about 278 hours. In tests of a single steel specimen subjected to periodic bending at the loading frequency $f = 100$ Hz, being a standard in machines used for rotating bending, obtaining the base number of cycles equal to 10·106 needs 28 hours. For the Staircase method this time is to be multiplied by the number of tested specimens.

In this context, accelerated methods to determine the fatigue limit are sought which will enable both to shorten the time needed to obtain the results, and to reduce the number of specimens needed for tests. In general, the accelerated methods are expected to shorten the fatigue examination and reduce its cost, at the same time ensuring that their quality does not differ substantially from the classical methods. The group of accelerated methods includes the Locati method [8] and the method of programmed fatigue tests [9], which, however, require the information on the slope coefficient of the fatigue curve. To avoid this difficulty, the method is combined with thermographic techniques, among other approaches [10].

Attempts to improve the accuracy in determining the fatigue limit focus on seeking new methods based on physical phenomena related with the fatigue process. Since the specimen or the structural element subjected to static load [11][12][13] or dynamic load is a source of heat generated as a result of internal processes, mainly those related with plastic deformation [14] [15][16], then the methods which base on specimen temperature measurements, in particular contactless thermographic methods, are very useful for modelling the fatigue process [17].

It was Risitano who first used the thermographic method to determine the fatigue limit in 1986 [18]. Then this method was used and/or modified in [19][20][21][22], among other works. A similar idea was used when determining the fatigue limit in the Lock-In method [23][24]. In the above works the fatigue limit was calculated, as a rule, for axial loads, based on the time interval of temperature stabilisation which occurs during phase 2 of fatigue loading (fig. 1 – line A).

However, not all materials reveal the abovementioned temperature stabilisation during fatigue loading, which substantially reduces the scope of application of the already developed thermodynamic methods of accelerated fatigue limit calculation. The method presented in this paper bases on constant rate of temperature increase which is observed during phase 2 of fatigue load (fig. 1 – line B), as illustrated by the case of corrosion resistant austenitic steel X5CrNi18-10 subjected to rotating bending.

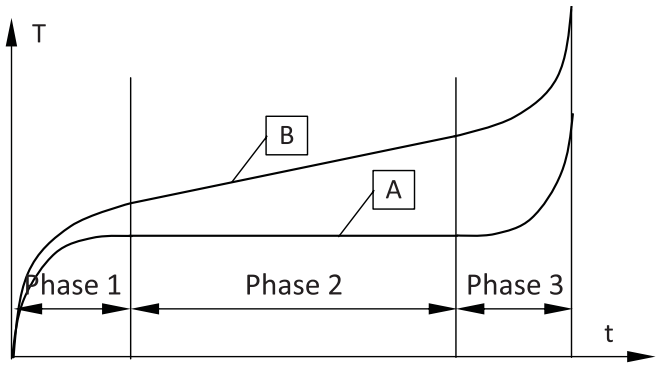

Fig. 1. Changes of temperature T during fatigue test for the material which reveals temperature stabilisation (line A) or constant temperature increase rate (line B) during phase 2

TEST RIG AND SPECIMENS

Test rig. The tests were performed at the Department Laboratory for Research on Materials and Structures (certified by the Polish Centre for Accreditation – PCA AB 372) of the Faculty of Mechanical Engineering at the UTP University of Science and Technology in Bydgoszcz, on the machine for rotating bending fatigue tests (loading frequency 77 Hz).

The basic component of the test rig was the thermographic camera CEDIP Silver 420M (FLIR SC5200) equipped with high-sensitivity matrix InSb cooled by Stirling pump. The basic parameters of the camera were:

- matrix resolution: 320x256 pixels,
- spectral range: 3.6÷5.0 μm,
- sensitivity: below 20 mK (available: 8 mK),
- thermogram recording frequency: up to 140 Hz for the entire matrix (up to 25000 Hz in lower resolution).

The thermographic camera recorded, at the frequency of 25 Hz, the 2D temperature distribution over the surface of the specimen subjected to rotating bending in the test machine. The image from the camera was passed via USB 2.0 interface to the PC computer with relevant software in which it was recorded, in digital form as PTW files, directly on the disc.

The software installed in the PC computer included:

- VirtualCAM, which provided two-way communication between the computer and the thermographic camera via the USB 2.0 interface,
- CIRRUS Front End, being the user's interface to control the CEDIP camera,
- ALTAIR, which enabled collecting, recording and advanced processing of thermographic images.

Specimens for tests. The specimens for the tests were made from drawn rods of corrosion resistant austenitic steel X5CrNi18-10 (1.4301) having the offset yield strength $R_{p0.2}$ = 706 MPa and the tensile strength R_m = 798 MPa. The geometry of the used specimens is shown in fig. 2, and the chemical composition of the specimen material is given in.

Tab. 1. Chemical composition of material for specimens

	C	Mn	Si	P	S	Cr	Ni	N
Acc. to standard PN-EN 10088-1:2014-12	≤0.07%	≤2%	≤1%	≤0.045%	≤0.015%	17÷19.5%	8÷10.5%	≤0.11%
In tested specimens	0.02%	1.53	0.61%	0.07%	0.016%	18.75%	8.22%	-

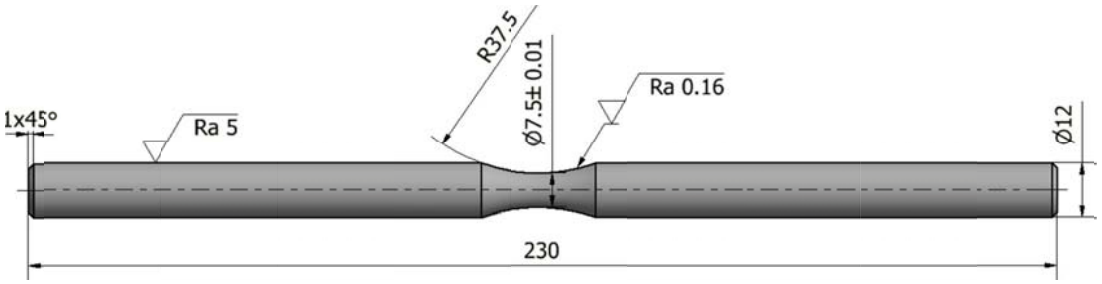

Fig. 2. Geometry of specimens used in tests

DESCRIPTION AND RESULTS OF TESTS

Results of Staircase test. The Staircase method based fatigue limit was calculated after assuming the base number of cycles equal to N_0 = 107. Thirty specimens were used in the tests. The lowest level of stress amplitude S_0 was equal to 260 MPa, while the stress increase was ΔS = 5 MPa. The fatigue limit determined from the Dixon and Mood's relation was equal to Sf = 277 MPa, with standard deviation ss = 23,6 MPa.

Results of accelerated method calculations. Three specimens were used in the accelerated tests. The specimens were loaded starting from the level S_1 = 230 MPa and then gradually increasing the load, with the step ΔS = 10 MPa, until the fatigue scrap was obtained. At each loading level, except the specimen damage level, n_i = 30 000 cycles were performed. collates fatigue lives obtained for successive specimens. Each tested specimen was damaged at a different loading level and, consequently, different total fatigue life was obtained for this specimen.

Tab. 2. Fatigue lives for successive specimens in accelerated tests

		Specimen		
		no. 1	no. 2	no. 3
Fatigue failure level	i	18	17	16
Failure stress, MPa	S_k	400	390	380
Total fatigue life, cycle	N_c	518 400	487 300	457 600

The results of thermographic measurements are shown in fig. 3 and fig. 4. fig. 3 shows temperature changes recorded on the surfaces of successive specimens during the entire test cycle, while fig. 4 presents specimen surface temperature change during the accelerated test, broken down by particular loading levels. We can notice that for all recorded loading levels, the time interval corresponding to the accelerated specimen temperature increase (phase 1 in Fig. 1) is followed by the time interval of stable temperature increase (phase 2 for curve B in Fig.1).

ANALYSIS OF TEST RESULTS

Fig. 5 shows specimen surface temperature increase rates corresponding to particular loading levels. In these diagrams, the results corresponding to the final (destroying) level of loading are omitted, as their values differ substantially from the remaining data. We can notice that the presented results have the minimum which can be related with the fatigue limit. In the vicinity of this minimum other processes connected with material degradation remarkably affect the energy balance of the entire specimen, as a result of which smaller part of it is involved in generating temperature increase. After exceeding the fatigue limit, the temperature increase rate becomes higher, which can be related with much larger plastic deformations.

a)

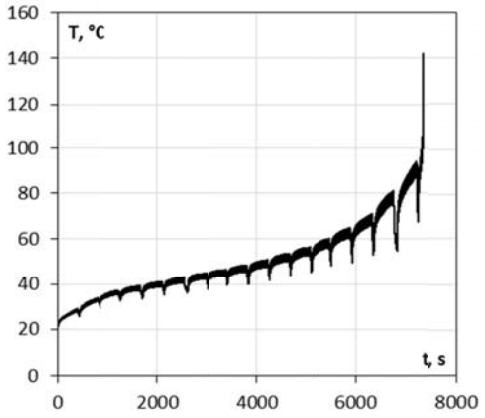

Fig. 3a. Change of temperature T of specimen surface during accelerated test for specimen 1 (a), 2 (b), and 3 (c)

b)

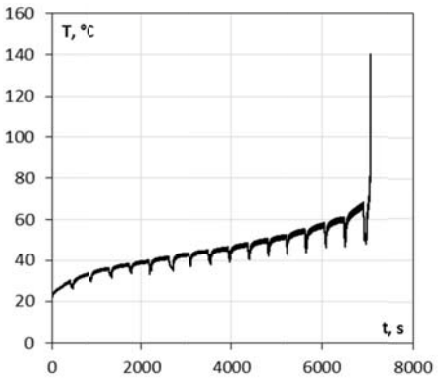

Fig. 3b. Change of temperature T of specimen surface during accelerated test for specimen 1 (a), 2 (b), and 3 (c)

c)

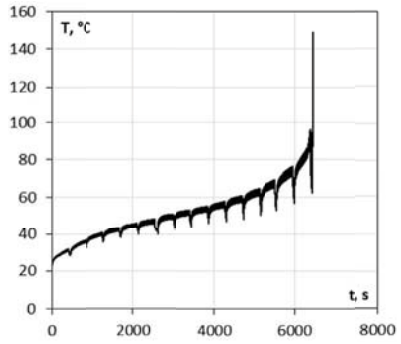

Fig. 3. Change of temperature T of specimen surface during accelerated test for specimen 1 (a), 2 (b), and 3 (c)

a)

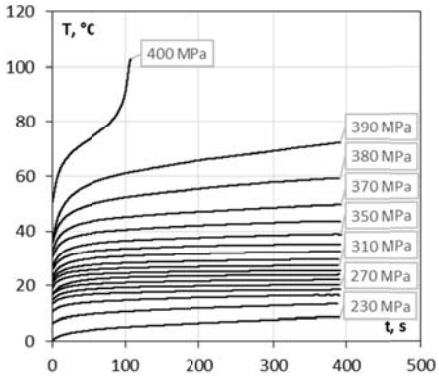

b)

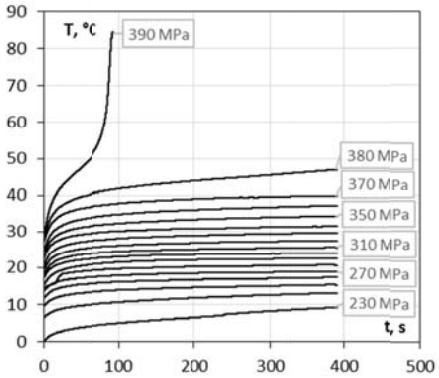

c)

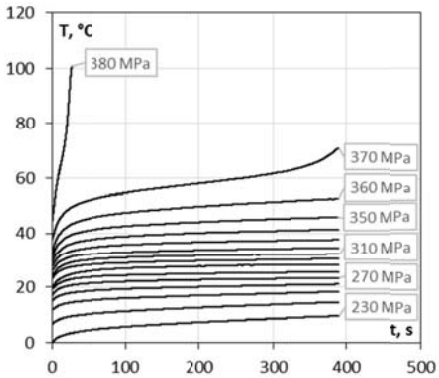

Fig. 4. Change of temperature T of specimen surface during accelerated test for particular loading levels of specimen 1 (a), 2 (b), and 3 (c)

a)

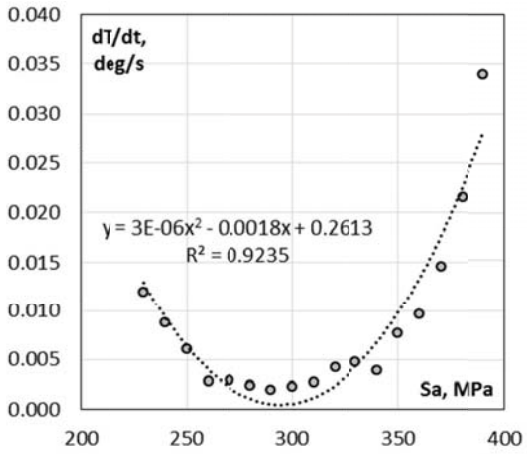

b)

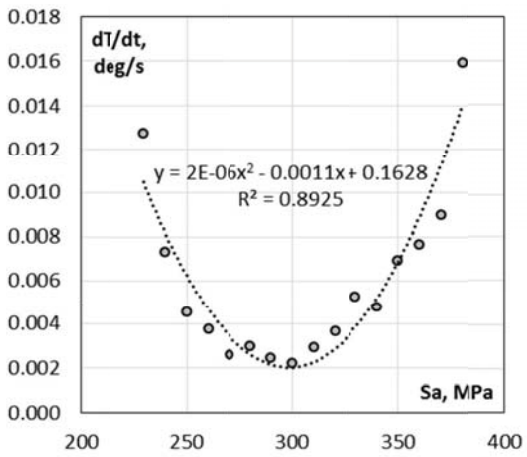

c)

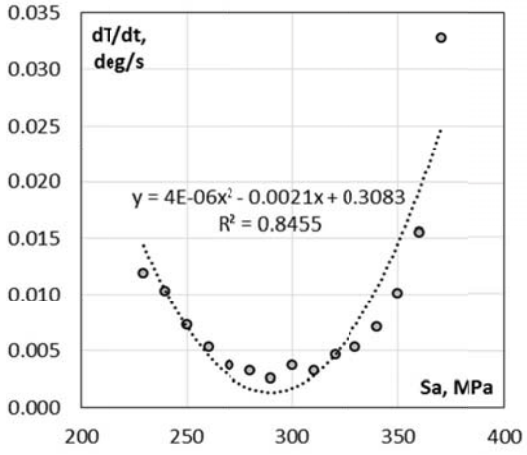

Fig. 5. Change of specimen surface temperature increase rate dT/dt during accelerated test for specimen 1 (a), 2 (b), and 3 (c)

The results of examination were approximated using the 2nd-order function, omitting the value for the last (destroying) loading level. The minimum of the function obtained in the above way was interpreted as the fatigue limit (Tab. 3).

Tab. 3. Fatigue limits for particular specimens in accelerated tests

		Specimen		
		no. 1	no. 2	no. 3
Fatigue limit, MPa	S_{fr}	294.4	298.4	289.9
		294.2±4.8		

Although each examined specimen was damaged at different loading level and reached different total fatigue life, the fatigue limits determined in the above way do not differ substantially from each other.

The results of examination of these three specimens have made the basis for determining the average value of the fatigue limit for the accelerated method S_{fr} = 294.2 MPa and the standard deviation for the test series s_{sr} = 4.2 MPa. Due to small number of results, the unbiased estimator of standard deviation obtained as $\hat{\sigma} = s_{sr} / c_4$ = 4.8 MPa, where the value of the coefficient c_4 = 0.8862 for $n = 3$ specimens, was assumed as the measure of standard deviation.

The level of coincidence between the fatigue limit values obtained from the accelerated method and from the Staircase method was checked using the statistical test for the average value of the population at the assumed significance level α=0.05 and $n = 3$. After adopting the value m0 = 277.0 MPa obtained from the Staircase method as the hypothetical fatigue limit and assuming the normal distribution of the fatigue limit N(277.0; 23.6), the zero hypothesis was formulated about equality of the fatigue limit obtained using the accelerated method m = 294.2 MPa in the form

$$H_0: \quad m = m_0 \tag{1}$$

against the alternative hypothesis

$$H_1: \quad m > m_0. \tag{2}$$

The value of the test statistics is

$$t = \frac{m - m_0}{s} \cdot \sqrt{n} = 1.26 \tag{3}$$

The critical value for the right-hand critical area $t_\alpha = 1.64$ Since the inequality

$$t < t_\alpha \tag{4}$$

holds, there is no reason to reject the zero hypothesis H_0 about equality of the fatigue limits assessed using the accelerated thermographic method and the Staircase method.

CONCLUSIONS

The presented accelerated thermographic method makes it possible to shorten fatigue tests and limit the number of examined specimens, which substantially reduces examination costs, at the same time ensuring that the obtained results do not differ statistically from those obtained using the long-lasting Staircase method.

Based on the tests performed for steel X5CrNi18-10, reported in the paper, and steel C45, we can conclude that, compared to other presently used thermographic methods, the here proposed method enables to calculate faster the fatigue limit for cases of rotating bending of steels which reveal linear temperature increase and not stabilisation at a given level during fatigue loading, i.e. have the time-temperature characteristics close to line B in Fig. 1.

ACKNOWLEDGEMENTS

The publication financed by The Polish National Centre for Research and Development in the framework of the INNOTECH – IN-TECH program identified as the project No. INNOTECH-K3/IN3/32/227826/NCBR/14.

BIBLIOGRAPHY

1. Kozak, J., Górski, Z.: Fatigue strength determination of ship structural joints. Part I. Polish Maritime Research, No. 2(69), Vol. 18, 28–36 (2011).
2. Szala, G.: Comments on linear summation hypothesis of fatigue failures. Polish Maritime Research, No. 3(83), Vol. 21, 77–85 (2014).
3. Skibicki, D.: Experimental verification of fatigue loading nonproportionality model. Journal of Theoretical and Applied Mechanics, 45, 2, 337–348 (2007).
4. Skibicki, D.: Multiaxial fatigue life and strength criteria for non-proportional loading. Materials Testing, 48, 3, 99–102 (2006).
5. Dixon, W.J.: The Up-and-Down Method for Small Samples. Journal of the American Statistical Association, 60, 312, 967–978 (1965).
6. Dixon, W.J., Mood, A.M.: A Method for Obtaining and Analyzing Sensitivity Data. Journal of the American Statistical Association, 43, 241, 109–126 (1948).
7. Collins, J.A.: Failure of materials in mechanical design - analysis, prediction, prevention. John Wiley & Sons, New York (1993).
8. Radaj, D.: Design and analysis of fatigue resistant welded structures. Abington, Woodhead Publishing (1990).
9. Szala, J.: Application of programmed fatigue tests to evaluating fatigue limit. Mechanika Teoretyczna i Stosowana, 3, 26, 523–539 (1988) - in Polish.
10. Lipski, A.: Determination of Fatigue Limit by Locati Method using S-N Curve Determined by Means of Thermographic Method. Solid State Phenomena, 223, 362–373 (2014).

11. Lipski, A.: Impact of the Strain Rate during Tension Test on 46Cr1 Steel Temperature Change. Key Engineering Materials, 598, 133–140 (2014).

12. Lipski, A., Borooński, D.: Use of Thermography for the Analysis of Strength Properties of Mini-Specimens. Materials Science Forum, 726, 156–161 (2012).

13. Lipski, A., Lis, Z.: Temperature Changes Induced by the Portevin-Le Châtelier (PLC) Effect during Tensile Test Based on the Example of CuZn37 Brass. Solid State Phenomena, 224, 238–243 (2014).

14. Kaleta, J., Błotny, R., Harig, H.: Energy Stored In A Specimen Under Fatigue Limit Loading Conditions. Journal Of Testing And Evaluation, 19, 4, 326-333 (1991).

15. Audenino, A.: Correlation between thermography and internal damping in metals. International Journal of Fatigue, 25, 4, 343–351 (2003).

16. Doudard, C., Calloch, S., Hild, F., Roux, S.: Identification of heat source fields from infrared thermography: Determination of "self-heating" in a dual-phase steel by using a dog bone sample. Mechanics of Materials, 42, 1, 55–62 (2010).

17. Lipski, A., Skibicki, D.: Variations of the Specimen Temperature Depending on the Pattern of the Multiaxial Load – Preliminary Research. Materials Science Forum, 726, 162–168 (2012).

18. La Rosa, G., Risitano, A.: Thermographic methodology for rapid determination of the fatigue limit of materials and mechanical components. International Journal of Fatigue. 22, 1, 65–73 (2000).

19. Luong, M.P.: Infrared thermographic scanning of fatigue in metals. Nuclear Engineering and Design, 158, 2-3, 363–376 (1995).

20. Luong, M.P.: Fatigue limit evaluation of metals using an infrared thermographic technique. Mechanics of Materials, 28, 1, 155–163 (1998).

21. Cura, F., Curti, G., Sesana, R.: A new iteration method for the thermographic determination of fatigue limit in steels. International Journal of Fatigue, 27, 4, 453–459 (2005).

22. Galietti, U., Palumbo, D., De Finis, R., Ancona, F.: Fatigue limit evaluation of martensitic steels with thermal methods. The 12th International Conference of Quantitative Infrared Thermography, QIRT, Bordeaux (2014).

23. Li, X.D., Zhang, H., Wu, D.L., Liu, X., Liu, J.Y.: Adopting lock-in infrared thermography technique for rapid determination of fatigue limit of aluminum alloy riveted component and affection to determined result caused by initial stress. International Journal of Fatigue, 36, 1, 18–23 (2012).

24. Kordatos, E.Z., Dassios, K.G., Aggelis, D.G., Matikas, T.E.: Rapid evaluation of the fatigue limit in composites using infrared lock-in thermography and acoustic emission. Mechanics Research Communications, 54, 14–20 (2013).

CONTACT WITH THE AUTHOR

Adam Lipski

UTP University of Science and Technology
Faculty of Mechanical Engineering
Department Laboratory
for Research on Materials and Structures
7 Kaliskiego Street
85-796 Bydgoszcz
Poland

e-mail: Adam.Lipski@utp.edu.pl

POLISH MARITIME RESEARCH 4(88) 2015 Vol. 22; pp. 70-75
10.1515/pomr-2015-0074

NONLINEAR VIBRATION SIGNAL TRACKING OF LARGE OFFSHORE BRIDGE STAYED CABLE BASED ON PARTICLE FILTER

Qingwei Ye, Ph. D.
Zhimin Feng, Prof.
Debin Yuan, Ms. C.
Ningbo University, Zhejiang, China

ABSTRACT

The stayed cables are key stress components of large offshore bridge. The fault detection of stayed cable is very important for safe of large offshore bridge. A particle filter model and algorithm of nonlinear vibration signal are used in this paper. Firstly, the particle filter model of stayed cable of large offshore bridge is created. Nonlinear dynamic model of the stayed-cable and beam coupling system is dispersed in temporal dimension by using the finite difference method. The discrete nonlinear vibration equations of any cable element are worked out. Secondly, a state equation of particle filter is fitted by least square algorithm from the discrete nonlinear vibration equations. So the particle filter algorithm can use the accurate state equations. Finally, the particle filter algorithm is used to filter the vibration signal of bridge stayed cable. According to the particle filter, the de-noised vibration signal can be tracked and be predicted for a short time accurately. Many experiments are done at some actual bridges. The simulation experiments and the actual experiments on the bridge stayed cables are all indicating that the particle filter algorithm in this paper has good performance and works stably.

Keywords: nonlinear vibration of stayed cables; large offshore bridge; particle filter; signal tracking

INTRODUCTION

Particle filter is known as sequential Monte Carlo method (SMC) in statistics. It is a sophisticated model estimation technique based on large rand simulations [8]. Particle filters are usually used to estimate nonlinear models, but typically where the state space of the latent variables is continuous rather than discrete. It is an advance filter tool compare with Kalman filter. They are often an alternative to the Extended Kalman filter (EKF) or unscented Kalman filter (UKF) with the advantage that, with sufficient samples, they approach the Bayesian optimal estimate, so they can be made more accurate than either the EKF or UKF. Particle filters have important applications in signal processing, econometrics and in other fields [3,8].

As the main bearing member, stayed cables are the key stress components of cable-stayed bridge. Cable vibration signal can reflect the change of the external excitation and cable force timely [6,7]. For its light quality, flexibility of structure and low damping, stayed cables produce large amplitude vibration easily under external excitation. It really poses an extraordinary threat to the safety and durability of the cables [10,11,12]. Feature extraction of the cable vibration signal not only can reflect the bridge's running state, but also is the basis of follow-up parameters measurement. It has great significance in application engineering. Taking the sag influence and geometrical non-linearity into consideration, cable vibration is the mutual coupling of deck vibration and cable natural vibration, showing nonlinear vibration characteristics [1,5]. In order to solve the problem that nonlinear vibration equation is hard to solve and the nonlinear signal is difficult to process, the commonest numeric integration algorithms, such as Runge-Kutta, have worse anti-noise ability and high distortion under strong noise environment. Due to lacking of effective signal filtering methods, there is a great limitation in the field of dynamic signal analysis.

Based on cable-beam coupling nonlinear vibration theory, the article uses finite difference method to build discrete nonlinear vibration model. Then particle filter theory is applied in the filtering of the forecast signal, building a new method to solve nonlinear model problem. The simulation results and cable vibration signal tests show that particle filter theory combined with discrete nonlinear vibration model represses the noise effectively and extracts cable vibration signal accurately. It provides a stable and reliable signal tracking and forecasting method.

PARTICLE FILTER PRINCIPLE

Particle filter theory [3,8] is also called sequential Monte-Carlo theory, condensation algorithm, boot strap filter algorithm and sampling importance resample, etc. By the means of looking for a group of random samples, spreading in state space, the theory replaces integration by sample mean through approximating the posterior probability density function. Particle filter is the estimation process getting state minimum variance. These samples are called particles. It realizes recursion Bayes estimation via nonparametric Monte-Carlo method. PF theory estimates target state through the constantly change of particle weight in the state-space model.

The state equation and observation equation for common discrete system can be expressed as follows:

$$x_{k+1} = f_k(x_k, v_k) \quad y_{k+1} = h_k(x_k, n_k) \tag{1}$$

Where x_k is the system state vector at k moment. y_k is the observation output. And the v_k is the system noise. The n_k is the observation noise. The $f(\cdot)$ and h(·) make up the system state equation and observed equation. $X_k = [x_0, x_1, ..., x_k]$ and $Y_k = [y_0, y_1, ..., y_k]$ are defined to be the accumulation state and accumulation observation by k moment.

If the initial probability density function is known as $p(x_0 \mid y_0) = p(x_0)$ the state prediction equation is as follows. [3]

$$p(x_k \mid x_{k-1}) = \int p(x_k \mid x_{k-1}) p(x_{k-1} \mid y_{1:k-1}) dx_{k-1} \tag{2}$$

The status update equation can be expressed as

$$p(x_k \mid y_{1:k}) = p(y_k \mid x_k) p(x_k \mid y_{1:k-1}) / p(y_k \mid y_{1:k-1}) \tag{3}$$

Among the formula $p(y_k \mid y_{1:k-1}) = \int p(y_k \mid x_k) p(x_k \mid y_{1:k-1}) dx_k$

The above formula is the basic idea of optimal Bayesian estimation. Particle filter is sequential Monte-Carlo simulation method based on Bayes principle. If importance density function $q(x_{0:k} \mid y_{1:k})$ is expressed in even product form as follows.

$$q(x_{0:k} \mid y_{1:k}) = q(x_0) \prod_{j=1}^{k} q(x_j \mid x_{0:j-1}, y_{1:j}) \tag{4}$$

And suppose state matching Markov process, under given state, weighted recursive formula can be expressed as follows:

$$w_k = \frac{p(y_{1:k} \mid x_{0:k}) p(x_{0:k})}{q(x_k \mid x_{0:k-1}, y_{1:k}) q(x_{0:k-1} \mid y_{1:k})} = w_{k-1} \frac{p(y_k \mid x_k) p(x_k \mid x_{k-1})}{q(x_k \mid x_{0:k-1}, y_{1:k})} \tag{5}$$

The simplest way to get important probability density function is making it equal to prior probability density:

$$q(x_k \mid x_{0:k-1}, y_{1:k}) = p(x \mid x_{k-1}) \tag{6}$$

If assuming that a group of random sample are got at k-1 moment: $x_{k-1}^i \sim p(x_{k-1} \mid Y_{k-1})$ (i=1…N, N is particle count), it can be obtained that:

$$p(x_{k-1} \mid y_{1:k-1}) \approx \sum_{i=1}^{N} w_{k-1}^i \delta(x_{k-1} - x_{k-1}^i) \tag{7}$$

Updated probability density function is expressed as degeneracy problem in particle filter.

$$p(x_k \mid y_{1:k}) \approx \sum_{i=1}^{N} w_k^i \delta(x_k - x_k^i) = \frac{p(y_k \mid x_k) \sum_{i=1}^{N} w_{k-1}^i p(x_k \mid x_{k-1}^i)}{p(y_k \mid y_{1:k-1})} \tag{8}$$

Where, N_{eff} is used to evaluate degradation level of a sample.

$$N_{eff} = 1 / \sum_{j=1}^{N} (w^j)^2 \tag{9}$$

Among the formula w^j is defined as normalized weight.

NONLINEAR VIBRATION MODEL PROCESSING ALGORITHM BASED ON PARTICLE FILTER

Due to non-parametric feature, particle filter overcome the shortage that random variable must obey Gaussian distribution in non-linear filter. It can express a much wider range of distribution than traditional models, and has strong ability to adapt to non-linear feature of variable parameters. Here, we try to apply particle filter theory in the processing of discrete nonlinear stayed cable vibration model. Based on the discrete nonlinear vibration equation, the system state equation and observation equation needed by particle filter are built. Finally, a new method, processing non-linear vibration model, is formed.

Taking the initial sag, geometric non-linearity and beam excitation into consideration, response of cable is non-linear vibration response.

Based on the assumptions as follows,

1) ignoring static deflection of beam

2) gravitational sag curve is parabola

3)cable vibration is the plane problem without regard to the vibration along the cable axial direction

4) cable is flexible and not concerned with flexural rigidity and shearing rigidity. The article analyses cable vibration system and builds cable-beam coupling model of cable-stayed bridge [2,9].

Tagata [9] points out that the basic mode plays a major role in tightening string-end vibration. According to oscillatory differential equation [2] under beam-end excitation, combining with model boundary conditions, introducing viscous damping ratio ζ_c, Galerkin method is used to get cable non-linear vibration equation of beam vertical excitation. In Fig.1, where d_1 is defined as span sag, l_c is the length of cable. v_b and v_c are the beam lateral displacement and cable lateral deflection.

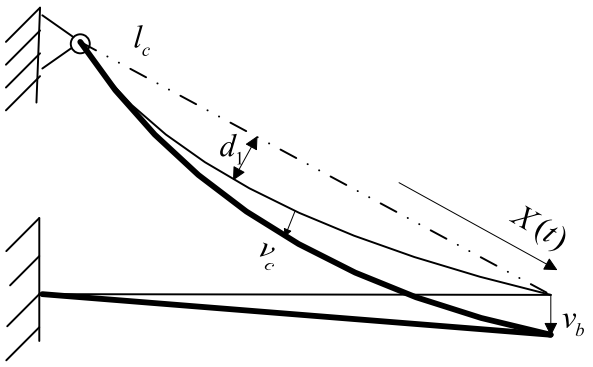

Fig. 1. Stayed cable model

$$\ddot{x}(t)+b\dot{x}(t)+c_1x(t)+c_2cos(w_bt)x(t)+dx^2(t)+ex^3(t)+fcos(w_bt)=0 \quad (10)$$

$a = \pi / l_c$, $b_1 = d_1 / l_c$. The coefficients in the formula can be expressed as:

$$f=E_cA_c\frac{32b_1}{m_cl_c^2\pi},\quad b=2\xi_cw_c,\quad c_1=w_c^2,\quad d=\frac{E_cA_ca^2b_1}{m_cl_c}[\frac{64al_c}{3\pi^2}+16/\pi],\quad c_2=\phi\chi$$

$$\phi=\frac{E_cA_ca^2}{m_cl_c}[1-16b_1^2(\frac{1}{6}-\frac{1}{\pi^2})]-\frac{32ab_1^2}{m_cl_c^2\pi},\qquad e=\frac{E_cA_c}{m_cl_c}[\frac{3}{8}a^4l_c-a^4b_1^2l_c(1-\frac{3}{2\pi^2})-\frac{10a^3b_1^2}{\pi}]$$

Where x(t) is the displacement function of stayed cable. w_c is first natural frequency considering the sag influence and the initial equilibrium position. w_b is cable oscillation frequency. Z is the vibration amplitude component along cable direction. E_cA_c is the tensile rigidity of cable. m_c is expressed as quality of unit length. c_2 and f indicate parameter vibration term and forced vibration term, reflecting non-linear feature of equation above.

In order to solve the non-linear equation above, traditional methods, such as Runge-Kutta, Adams multistep method, are often used. But interrelated solution models are too complex and the traditional methods have poor anti-noise capacity, and further, there is no subsequent filter algorithm matching with them. Based on finite difference theory, differentiation is replaced by central difference, as follows

$$\dot{x}(k)=\frac{x(k+1)-x(k-1)}{2h}\qquad \ddot{x}(k)=\frac{x(k+1)-2x(k)+x(k-1)}{h^2} \quad (11)$$

Where represents the k-th sample of x(t). h is the quantifying step size. The less of h, the less of error, the difference value is more close to the differential value. The precision of $\dot{x}$ and $\ddot{x}$ can be ensured when sampling rate is big enough and h is small enough.

Eq.(11) is substituted in Eq.(10), discrete nonlinear vibration model on any cable position can be expressed as the next:

$$Ax(k+2)+B_1x(k+1)+B_2\cos(w_bh(k+1))x(k+1)+ \quad (12)$$
$$Cx(k)+Dx^2(k+1)+Ex^3(k+1)+f\cos(w_bh(k+1))=0$$

Where $A = 1/h^2$, $B_1 = c_1 - 2/h^2$, $B_2 = c_2$, $C = 1/h^2 - b/2h$, $D = d$, $E = e$.

Knowing from the above formulas, if the cable model parameters (A,B1,B2,C,D,E,f) are known, based on the observation value of vibration signal at k moment and k+1 moment, we can forecast vibration signal value at next moment effectively.

According to the discrete non-linear vibration model above, to estimate model parameters, Eq. (12) can be expressed in matrix operational form.

$$Q_k\vec{r}=\vec{u}_{k+1} \quad (13)$$

Where:

$$Q_k=\begin{bmatrix} x_{k+1} & g_{k+1}*x_{k+1} & x_k & x^2{}_{k+1} & x^3{}_{k+1} & g_{k+1} \\ x_{k+2} & g_{k+2}*x_{k+2} & x_{k+1} & x^2{}_{k+2} & x^3{}_{k+2} & g_{k+2} \\ \vdots & \vdots & \vdots & \vdots & \vdots & \vdots \\ x_{k+N} & g_{k+N}*x_{k+N} & x_{k+N-1} & x^2{}_{k+N} & x^3{}_{k+N} & g_{k+N} \end{bmatrix}$$

is defined as observation signal matrix. Constant matrix $\vec{r}=\left[-B_1/A\ \ -B_2/A\ \ -C/A\ \ -D/A\ \ -E/A\ \ -f/A\right]^T$ is defined as model parameters matrix. $\vec{u}_{k+1}=[x_{k+2}\ \ x_{k+3}\ \ x_{k+4}\ \ x_{k+5}..x_{k+N+1}]^T$ is defined as forecast signal matrix. $x_k = x(k)$ is value of x(k) at k moment. $g_k = \cos w_b h(k-1)$ is a discrete cosine function. Random positive integer N represents expanding columns number.

Least-squares estimation(LSE) is used to get parameter matrix $\vec{r}$ .For nonlinear vibration signals, forecast signal matrix $\vec{u}_k$ and observation signal matrix Q_k can be built based on Eq. (13). Then the article uses LSE to get the estimate value $\hat{\vec{r}}$ of parameter matrix $\vec{r}$.

$$\hat{\vec{r}}=(Q_k{}^TQ_k)^{-1}Q_k{}^T\vec{u}_k \quad (14)$$

Knowing $\vec{r}$ from observation signal values, state equation of nonlinear stayed cable vibration model can be built from eq.(13). Adding observation noise $\vec{w}_k$ to state signal, observation equation can be got.The state equation and observation equation can be expressed as follows:

$$\begin{cases}\vec{u}_{k+1}=Q_k\hat{\vec{r}}+\vec{v}_k\\ \vec{y}_{k+1}=\vec{u}_{k+1}+\vec{w}_k\end{cases} \quad (15)$$

Where, observation signal matrix Q_k is seen as generalized state input at k moment. Forecast signal matrix $\vec{u}_{k+1}$ is regard as generalized state output at k+1 moment. $\vec{y}_{k+1}$ is defined as system observation output at k+1 moment. $\vec{v}_k$ is state noise. $\vec{w}_k$ is the observation noise.

The state equation and observation equation upon can be seen as state equation and observation equation needed by particle filter. Following particle filter algorithm, based on signal observation values by this moment, we can predict the signal values in the follow-up moments. By calculating the weight of every particle and resample, the error between predicted value and truth value is being reduced during the filter process. The noise suppression purpose can be achieved effectively.

According to the theory of discrete nonlinear model and particle filter upon, discrete nonlinear model processing method based on PF theory can be constructed as follows.

There is cable vibration signal from i moment to j moment. $X_{i\sim j}=[x_i,x_{i+1},\cdots,x_j],\ j>i$ is defined as i-th of vibration signal, with the length of L = j - i + 1. With PF theory and nonlinear vibration model, we can predict and track the signal of next moments.

(a) In the first place, for any observation signal $X_{k\sim k+N}$ with length of L=N+1, forecast signal matrix $\vec{u}_{k+1}$ and observation signal matrix Q_k is built from eq.(13). Then following eq.(14), parameter matrix estimate value can be obtained by using Least-squares estimation method, as follows:

$$\hat{\vec{r}} = LSE(X_{k\boxtimes k+N}) = (Q_k{}^T Q_k)^{-1} Q_k{}^T \vec{u}_k \qquad (16)$$

(b) After knowing parameter matrix estimate value $\hat{\vec{r}}$ based on discrete nonlinear model and eq.(15), the state equation and observation equation needed by particle filter is built easily.

(c) Particle filter designed on the basis of Eq.(15) processes k-th vibration signal $X_{k\sim(k+N)}$, filtering out the environment noise, and get follow-up output signal values $\hat{y}_{k+N+1}$.

The resample method is defined as follows: calculating the weight of every particle: $q=\exp\{-(\hat{x}_k-\hat{y}_k)^2/2Q\}$.Where, $\hat{x}_k$ is represent observation value of x_k, which is obtained from nonlinear model immediately. $\hat{y}_k$ is defined as particle filter value of x_k, in which the noise is restrained effectively. Finally, we decide filter signal value based on normalized weight coefficients.

(d) After particle filter at k moment, predicted signal value $\hat{y}_{k+N+1}$ is equal to observation value x_{k+N+1} at k+N+1 moment. Using x_{k+N+1} to update vibration signal segment $X_{k+1\sim(k+N+1)}$. The steps upon are repeated to update observation signal matrix Q_{k+1} and forecast signal matrix $\vec{u}_{k+2}$. Loop forecast can get cable vibration signal of any length we need.

According to the process method of discrete nonlinear vibration model upon, we can draw the follows conclusions easily: In system state equation, generalized state inputs contains nonlinear terms. And there is obvious non-linear relation between state output, observation output and input. Particle filter can process the non-linear relation effectively. Combine with discrete non-linear cable model, particle filter can predict signal of any period time theoretically. It provides a convenience to anticipate stayed-cable performance in advance.

SIMULATION EXPERIMENT

In order to check the effect of particle filter theory applied on discrete non-linear vibration model, one stayed cable of a cable-stayed bridge was taken into research. According to article [12],the parameters are set as follows: $A_c = 71.97 \times 10^{-4}\ m^2$, $\theta = 56.4^0$, $l_c = 129.2$ m, the axial tensile force of cable H = 33000 kN, quality of unit length $m_c = 58.8$ kg/m, modulus of elasticity $E_c = 200$ GPa the effect of viscous damping ratios is taking into account, $\zeta_c = 0.002$. It can be proved easily that the nonlinear system including square term and cubic term can produce resonance only when $w_b = w_c$ or $w_b = 2w_c$ .For the sake of simplifying the simulation process, the article do the experimental study only under the situation $w_b = 2w_c$.

According to finite difference theory, smaller the time discrete step h is, higher precision of the discrete nonlinear model shown by Eq(12) is. Setting h=0.001s, under different noise environment, the article extracts the vibration signal from discrete nonlinear system and compares the signal accuracy with classical Runge-Kutta method (under no noise environment).

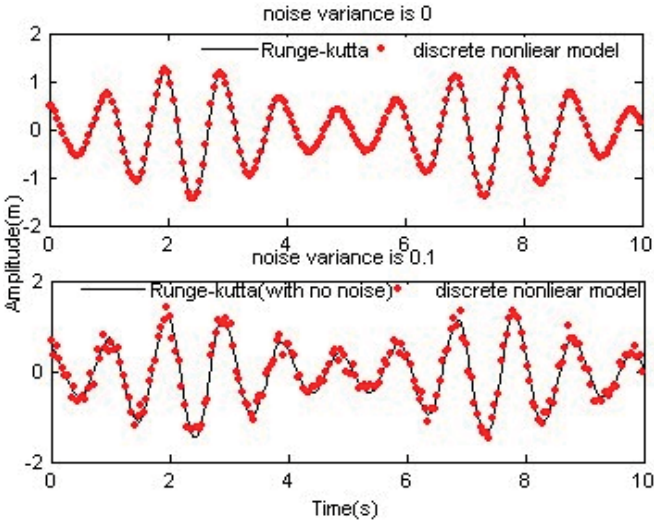

Fig. 2. The extracting efficiency based on discrete model

As we can see in Fig.2, with no noise or low noise, discrete nonlinear model built can be used to extract extremely high accurate signal. The degree of coupling between Vibration signal curve forecast by Runge-kutta theory and discrete nonlinear model is very high. Under the situation that the noise variance is equal to 0.1, due to noise accumulation, the vibration signal, extracted by nonlinear model, compared with no noise signal (extracted by Runge-Kutta under no noise environment), happen serious distortion. SNR depress to 12.09 dB.

Combined with Fig.1 example, the signal with noise (extracted by discrete nonlinear model under noise environment) from 1s to 3s is assume as observation signal. System noise v_k variance is 0.001. Observation noise variance u_k is equal to 0.1 and 0.05. Particles number is 500. Observation signal length N is equal to 2000.

For convenient viewing, the signal between 3s-5s is forecasted by particle filter theory as Fig.3 and Fig.4. Signal points with noise have large swing around pure signal. SNR is fall to 14.67 dB and 12.09 dB. After being processed by particle filter, the signal obtained from nonlinear model shows satisfactory agreement with pure signal. SNR is up to 29.61 dB and 26.65 dB. Predictive signal is highly accurate. The conclusion shows the application of particle filter can reduce effect of noise effectively and keep signal accuracy. Signal after being filtered is of great practical value in engineering.

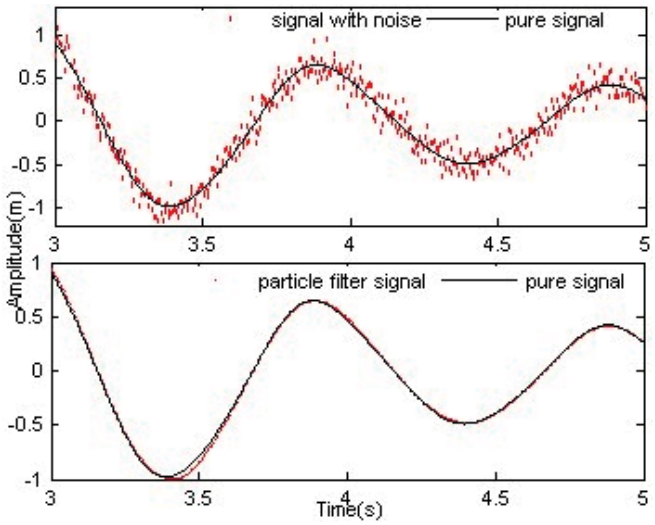

Fig. 3. The simulation analysis comparison at VAR(uk) = 0.05

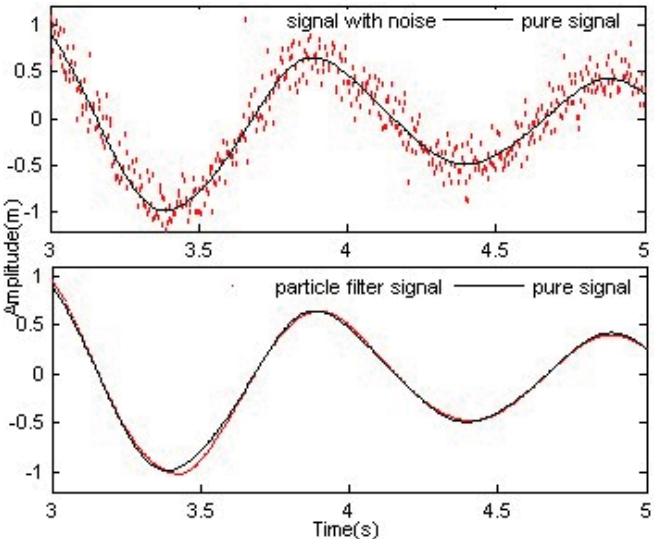

Fig. 4. The simulation analysis comparison VAR(uk) = 0.1

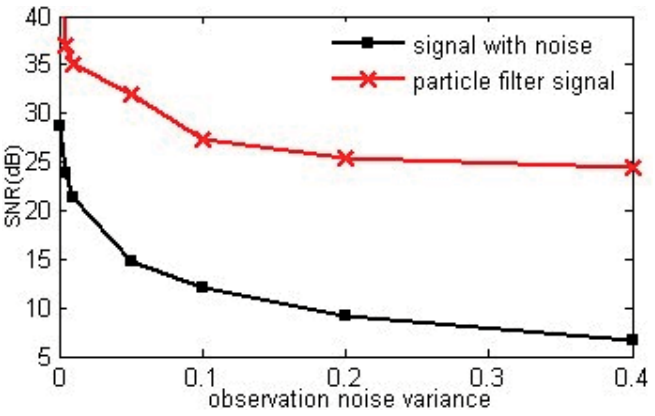

Fig. 5. The relation curve between noise variance and SNR

As presented in Fig5, with different observation noise variance, signal with noise (obtained from nonlinear model immediately) and practical filter signal (which with noise being filtered) have different performance. The relation curve of SNR and observation noise variance is shown as follows.

THE APPLICATION IN CABLE-STAYED BRIDGE

In the following test, it uses the predicted algorithm based on particle filter theory on the cable-stayed bridge. We use WS - ZHT2 vibration equipment and double sensors to collect the vibration signal. The sensors are installed as shown in Fig.6.

It tests acceleration response through the environmental stimulation (disturbed by strong winds and others). Signal collection scheme adopts double multi-input and single output pulse incentive; one sensor to collect vibration response signal, the other sensor to collect environmental stimulation signal. 4000 points for sampling points, sampling frequency is set as 100 Hz. Based on particle filter and nonlinear model method, a signal segment for 5 s time length is seen as known signal point, to predict cable signal point ranged from 5 s-40 s. Then it is compared with the signal date collected by the sensors. The effect is presented as Fig.7.

Fig. 6. The picture of bridge and experimental devices

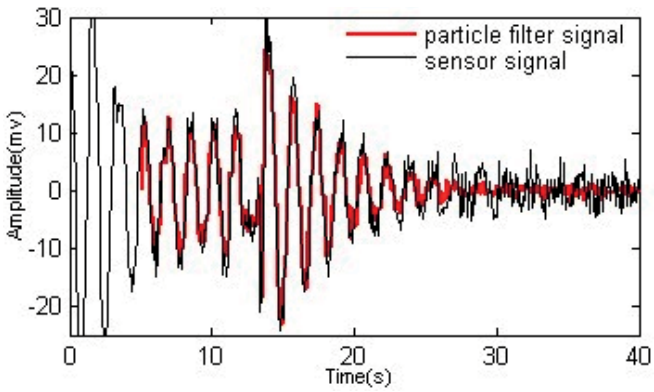

Fig.7. The particle filter effect of cable-stayed bridge data

The cable vibration signal filtered by particle filter, among the time from 25 s-40 s, is compared with real cable signal. Vibration amplitude caused by environment noise is effectively restricted and mean decay to 32% of original. Among the

whole particle filter period from 5 s to 40 s, the amplitude of filtered signal present attenuation characteristics. As we can see from the signal features, particle filter theory combined with nonlinear model has well anti-noise ability and can improve signal precision effectively.

CONCLUSIONS

Based on finite difference theory, this article builds a discrete nonlinear cable vibration model and combines particle filter theory with it. The new cable signal processing method finally reaches the goal that noise impetus is weakened and accurate cable vibration signal is distilled. The particle filter algorithm has good applicability to cable-stayed nonlinear model based on finite difference theory. The difficult to solve the cable nonlinear model, due to vibration model parameter nonlinearity, is solved effectively. The effective combination of particle filter with discrete model can overcome the high-distortion caused by noise accumulation and ensure accuracy of the prediction. Vibration signal after filter processing fully satisfy the need of engineering application, showing good potential in applications.

ACKNOWLEDGEMENT

This work has been financially supported by National Natural Sciences Funds of China (No. 61071198), Nature Science Funds of Zhejiang Province (No. LY13F010015) and Nature Science Funds of Ningbo (No. 2012A610019). This work is sponsored by K.C.Wong Magna Fund in Ningbo University.

REFERENCES

1. Chen Shuisheng, Sun Bingnan, "Numerical Study on Non-linear Parametric Vibration of Coupled Cables and Bird Gedecks", Chinese Journal of Civil Engineering, Vol.36, No.4, pp.70-75, 2003.

2. Gattulli V, Morandini M, Paolone A, "Parametric Analytical Model for Non-Linear Dynamics in Cable-Stayed Beam", Earthquake Engineering and Structural Dynamic, Vol.31, pp.1281-1300, 2002.

3. [3] Guillaume Thirel, Peter Salamon, Peter Burek and Milan Kalas. Assimilation of MODIS Snow Cover Area Data in a Distributed Hydrological Model Using the Particle Filter. Remote Sensing, Vol.5, No.11, pp.5825-5850, 2013.

4. Han Gao and Jingwen Li . "Detection and Tracking of a Moving Target Using SAR Images with the Particle Filter-Based Track-Before-Detect Algorithm". Sensors, Vol.14, No.6, pp. 10829-10845, 2014.

5. Hong weiming, Gao lili, "Vibration Analysis of Non-linear Coupling System of cable-stayed beam", Journal of Vibration Engineering, Vol.21, No.2, pp.115-119, 2008.

6. K.B.Waghulde, Dr. Bimlesh Kumar, "Vibration Analysis of Cantilever Smart Structure by using Piezoelectric Smart Material", International Journal on Smart Sensing and Intelligent Systems, Vol.4, No.3, pp.354-375, 2011.

7. Matsumoto M, Shiraishi N, Shirato H, "Rain-Wind Induced Vibration of Cables of Cable-Stayed Bridge". Journal of Wind Engineering and Industrial Aerodynamics, Vol.41, pp.2011-2022, 1992.

8. Olivier Brun, Vincent Teuliere, Jean-Marie Garcia, "Parallel Particle Filtering", Journal of Parallel and Distributed Computing, Vol.62, pp.1186-1202, 2002.

9. Tagata G. Harmonically Forced, "Finite Amplitude Vibration of a String", Journal of Sound and Vibration, Vol.51, No.4, pp.483-492, 1977.

10. Wang Zhigang, Sun Bingnan, "Parametric Vibration of Cable-Stayed Bridge", Chinese Journal of Civil Engineering, Vol.35, No.5, pp.28-33, 2002.

11. Ye Qingwei, Wang Tongqing, "Optimization modal analysis with PSO based on spectrum segmentation", Chinese Journal of Scientific Instrument, Vol.20, No.8, pp.1584-1590, 2009.

12. Zhao Yueyu, Lv Jiangen, "Non-linear Parametric Vibration of Cables in Cable-arch Composite Structures", Chinese Journal of Civil Engineering, Vol.39, No.12, pp.67-77, 2006.

CONTACT WITH AUTHOR

Qingwei Ye

Box 54,
Ningbo University
315211 Zhejiang
China

tel.: +85-13805877051
rmail: personalfree@163.com

POLISH MARITIME RESEARCH 4(88) 2015 Vol. 22; pp. 76-83
10.1515/pomr-2015-0075

EFFECTS OF VARIOUS FACTORS ON THE VIV-INDUCED FATIGUE DAMAGE IN THE CABLE OF SUBMERGED FLOATING TUNNEL

Gang Luo[a]
Jianxun Chen [a]
Xiaojun Zhou [b]
[a)]Chang'an University,China
[b)]Southwest Jiaotong University, China

ABSTRACT

According to the modal superposition method, the vortex vibration procedure of submerged floating tunnel cable was compiled using Matlab, based on the calculated results, the fatigue damage was predicted. The effects of various factors, such as cable density, cable length, and pretension and velocity distribution on vortex induced fatigue damage in the cable were studied. The results show that velocity distribution has more effect on the cable fatigue damage than cable length, cable density and pre-tension. Secondly, cable length has also relatively effect on the cable damage fatigue, cable density and pretension has limited in a certain range.

Keywords: submerged floating tunnel cable; vortex induced vibration; fatigue damage; factor analysis

INTRODUCTION

Submerged floating tunnel suspends in the certain depth underwater by the balance between gravity, buoyancy and the support system, and maintains the stability of the suspension by the tunnel support system [8]. When the buoyancy floating tunnel suffers is greater than its gravity, the anchor cable will be used to connect it with underwater foundation to balance the remaining buoyancy. As a support structure of the floating tunnel, the stability of anchor cable in the environment of the waves and the flow directly affects the stability of the floating tunnel, while the anchor cable will generate alternating dynamic stress in the vortex-induced vibration, and fatigue damage will occur in the long-term effect, potentially causing fracture damage, even the entire tunnel devastating disaster. Therefore, to the structural design, safety and durability evaluation of submerged floating tunnel, it has important theoretical significance and practical value to deeply study the fatigue damage and structure broken of the anchor cable of floating tunnel under the vortex-induced vibration, as well as the analysis about the durability of floating tunnel anchor cable.

The vortex-induced fatigue damage of flexible structure is one of the main factors of structural failure, so the main purpose of the experimental and theoretical study of vortex-induced vibration is to predict structure vortex-induced fatigue damage. The flexible structure vortex-induced damage prediction are different because of the different methods of vortex-induced vibration analysis.Vikestad [13] proposed a simplified method to forecast riser vortex induced fatigue damage under uniform flow in his doctoral thesis, in which ,stress range was substituted by the riser vortex-induced response the biggest displacement .While it does not consider the long-term structure of the vortex-induced vibration of alternating stress distribution ,which will lead to forecasting structure too large. Meling et al [7] used the orthogonal empirical function method to simplify the measured flow rate dates, and then get the velocity distribution of riser

design, thus predict the riser vortex-induced vibration. Trim et al [9] reduced the vortex induced vibration fatigue damage through the installation of suppression devices in experimental research. J.K Vandiver [11] developed an experience coefficient modal analysis method based on the forced vibration test to calculate riser vortex induced vibration fatigue damage under different velocity distribution .J R Chaplin [2] compared Riser vortex-induced vibration test data with different numerical computation structure, and drew some meaningful conclusions.

This paper compiles the program to forecast the Vortex-induced vibration fatigue damage of floating tunnel based on the theory of vortex-induced vibration and modal superposition method. First, it introduces the related knowledge of vortex-induced vibration and modal superposition method, and then verifies the algorithm of this chapter by JR Chaplin experiments.

VORTEX-INDUCED VIBRATION AND MODAL SUPERPOSITION METHOD

VORTEX-INDUCED VIBRATION EQUATION

Fig. 1 shows the structure model of floating tunnel supported by the anchor cables in the water and simplified form of anchor. The anchor cable usually consists of wire or strand, which can be simplified for a simply supported beam, so we can make the assumptions as follow, e.g. in the early work [6].

1) It is assumed that the anchor cable tension does not change along the anchor cable length, because the anchor cable pre-tension is much larger than the gravity of the structure

2) The anchor cable's geometry, sectional form, and the mass distribution does not change along the Anchor length

3) The flows is Constant shear flow which consistent with Z-axis positive direction in Fig. 1; the vibration of anchor cable is only considered in the plane XOY

4) When the anchor has a certain angle with the flow direction, then flow can be decomposed along the perpendicular to the anchor and the direction parallel to the anchor cable, and only the impact of perpendicular to the anchor cable velocity to structure will be considered.

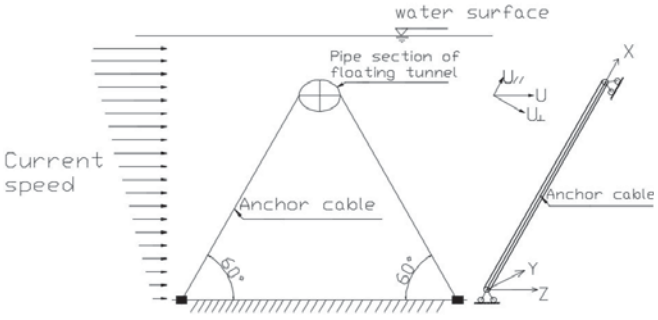

Fig.1. SFT model and cable simple form

Considering the large pre-tension suffered by the anchor cable, the anchor can be simplified as a hinged linear beam, and its vibration equation is:

$$EI\frac{\partial^4 Y(X,t)}{\partial X^4}-\frac{\partial}{\partial X}[(T-mgX)\frac{\partial Y(X,t)}{\partial X}]+m\frac{\partial^2 Y(X,t)}{\partial t^2}+R(X)\frac{\partial Y(X,t)}{\partial t}=P(X,t) \tag{1}$$

E - the elastic modulus of anchor cable, *I* - cross sectional moment of inertia,
Y(X,t) - Lateral displacement, *T* - pre-tension of anchor cable,
m - the mass per unit length of anchor cable, *R(X)* - System damping,
P(X,t) - Excitation force per unit length.

In order to simplify the analysis process, the formula (1) is nondimensionalized in the longitudinal direction .we make x=X/L, and assume $Y(x,t)=\sum_r Y_r(x)\phi_r(t)$, where $Y_r(x)=\sin(r\pi x/L)$ $\phi_r(t)=A_r\sin(\omega_r t)$

Equation (1) can be simplified as follow,

$$EI\frac{\partial^4\phi_r(x,t)}{\partial x^4}-\frac{\partial}{\partial x}[(\frac{T}{L^2}-\frac{mg}{L})\frac{\partial\phi_r(x,t)}{\partial x}]+$$
$$+m\frac{\partial^2\phi_r(x,t)}{\partial t^2}+R_r(x)\frac{\partial\phi_r(x,t)}{\partial t}=p_r(x,t) \tag{2}$$

MODAL SUPERPOSITION METHOD

The vibration equation of linear damping elastic continuum simply supported beam system can be simplified as,

$$M_r\ddot{\varphi}_r(t)+R_r\dot{\varphi}_r(t)+K_r\varphi_r(t)=p_r(t) \tag{3}$$

Where M_r , R_r , K_r and $p_r(t)$ are modal mass, modal damping , modal stiffness and modal excitation force, which are calculated as follow

$$M_r=\int_0^L Y_r^2(X)\,mdX \qquad R_r=\int_0^L Y_r^2(X)\,R(X)\,dX$$

$$K_r=-\int_0^L TY_r''(X)Y_r(X)\,dX \qquad p_r(t)=\int_0^L Y_r(X)\,P(X,t)\,dX$$

To r-order modal force, it is considered that the lift only works to structure in the incentive area and lift phase is non-inverting with structure modal speed. So $p_r(t)=\int_{L^r}|Y_r(X)|P(X,t)dX$. Based on the centrifugal force model by Blevins [1],

$$P(X,t)=0.5r_wDU^2(X)C_L(X,w_r)\sin(w_rt) \quad (4)$$

$C_L(X,\omega_r)$ is r-order modal corresponding lift coefficient of anchor cable at the X position ;making r-order Modal velocity as $\dot{\phi}_r(t)=A_r\omega_r\cos(\omega_r t)$,r-order modal excitation power can be expressed as the product of excitation force and modal velocity. r-order modal power dissipation power can be expressed as the product of the damping force and modal speed. when the system is in the steady-state response,the excitation power equals dissipation power. Excitation power Π_{in}^r and dissipation power Π_{out}^r can be express as follows

$$\Pi_{in}^r=\int_{L^r}\frac{1}{2}\rho_w DU^2(X)C_L(X,\omega_r)A_r\sin(\omega_r t)\cos(\omega_r t)|Y_r(X)|dX \quad (5)$$

$$\Pi_{out}^r=\int_L R(X)Y_r^2(X)A_r^2\cos^2(\omega_r t)dX \quad (6)$$

For periodic excitation force, the power is averaged in the period to simplify the calculation

$$E_{in}^r=\frac{1}{T}\int_0^T\Pi_{in}^r dt=\frac{1}{4}\int_{L^r}\rho_w DU^2(X)C_L(X,\omega_r)A_r\omega_r|Y_r(X)|dX \quad (7)$$

$$E_{out}^r=\frac{1}{T}\int_0^T\Pi_{out}^r dt=\frac{1}{2}\int_L R(X)Y_r^2(X)A_r^2\omega_r^2 dX \quad (8)$$

By $E_{in}^r=E_{out}^r$

$$\frac{A_r}{D}=\frac{\frac{1}{2}\int_{L^r}\rho_w U^2(X)C_L(X,\omega_r)|Y_r(X)|dX}{\int_{L-L^r}R_h(X)Y_r^2(X)\omega_r dX+\int_0^L R_s(X)Y_r^2(X)\omega_r dX} \quad (9)$$

Where $C_L(X,\omega_r)$ is the function of dimensionless displacement. Different A_r/D are got by calculated based on different lift model, which need iterative solution. Based on Blevins model [4], $C_L(z)=a+b(\frac{A_r}{D})+c(\frac{A_r}{D})^2$, a=0.35, b=0.6, c=-0.93.

The damping model uses the model proposed by Vengugopal Madan [12] in 1996.The damping constant $R_h(X)$ denotes unit force per unit velocity and unit length, which is different in the low reduced speed area and the high reduced speed area.

- the low reduced speed area

$$R_h(X)=\frac{\omega\pi\rho_w D^2}{2}[\frac{2\sqrt{2}}{\sqrt{Re_w}}+C_{K1}(\frac{A}{D})^2]+C_{K2}\rho_w DU(X) \quad (12)$$

- the high reduced speed area

$$R_h(X)=C_{K3}\rho_w U^2(X)/\omega \quad (13)$$

Where Empirical parameters C_{K1}, C_{K2} and C_{K3} are Respectively be got as ,0.25, 0.18 and 0.2.$Re_w=\omega D^2/\upsilon$ ω is Natural frequency, υ is the Kinematic viscosity of the fluid. As for the other symbols, ditto.

FATIGUE DAMAGE ANALYSIS

There are two types of prediction of fatigue life of marine structures, one is based on fatigue cumulative damage theory and the other is based on the theory of fatigue crack growth. In this paper, fatigue cumulative damage analysis method is adopted which based on the S-N curve and Miner guidelines, the method is simple and the results are reliable. It is assumed that the anchor rope vortex-excited alternating stress meets the random process that the mean is zero in the narrowband smooth, and its peak satisfies the Rayleigh distribution. In the modal analysis process, it is assumed that when the r-order modal drives, the number of Stress amplitude which anchor cable corresponding to in T is $N_L=f_rT$, T=365×24×3600s. According to the total damage in a year by the Multi-modal vortex-induced vibration in Modal superposition method, D can be expressed as [5]

$$D=\sum_r D_r=\sum_r\frac{f_rT}{C}(2\sqrt{2}\sigma_{rms})^b\Gamma(\frac{b}{2}+1)$$

σ_{rms} is the alternating stresses rms stress.

ALGORITHM VERIFICATION

TEST PROFILE

Chaplin [2] designed a sophisticated test program, which is conducted in the towing tank of the Delft Hydraulics Laboratory of the University of Southampton in the United Kingdom. The length of the pool is 230 m, width is 5 m, and depth is 6.5 m, the upper end of the riser is fixed to the mounting platform locomotives. The test apparatus shows in Fig. 2, riser parameters shows in Tab.1.

Tab.1. Test riser parameters

Density	Diameter (m)	Length (m)	Quality (kg/m)	Tension (N)	Stiffness/EI (Nm^2)	Sspeed(m/s)
3006	0.028	13.12	1.85	380-1900	29.9	0.1-1.0

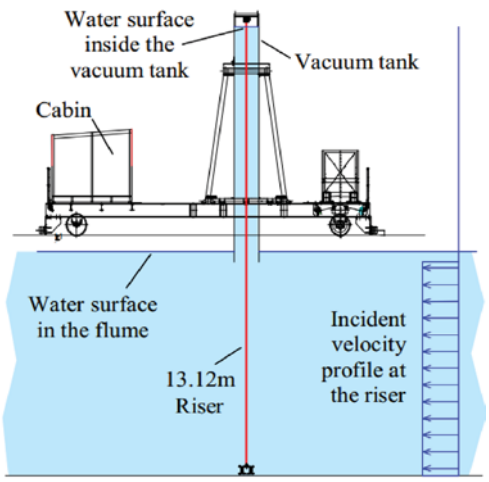

Fig.2. Computational mode[6]

In order to simulate the riser multi-modal vortex-induced vibration under the ladder flow effect in the Test design process, the part of the riser above the pool water surface is placed in the vacuum pipe container which is dragged with the riser model and full of water. So we can simulate the flow of role. The length of the part riser above the pool water surface is 7.22 m, and the flow rate of the water is 0 m/s, and the speed of flow in the pond is uniform .Both sides of riser are hinged, initial pre-tension is applied on the top, the tension adjustment range is 380 N-1900 N.

RESULT ANALYSIS

Selecting two conditions shown in Fig. 3 (a) and (b), it is found that the calculated result is closer to Chaplin test results and Pan Zhiyuan algorithm results, but the result of SHEAR7 calculation results is too large. In two different conditions, the current calculation dimensionless amplitude and main modes are well agreed with the experimental results, which verify the feasibility of the proposed algorithm in this paper.

THE ANALYSIS OF ANCHOR CABLE VORTEX-INDUCED FATIGUE IMPACT

In order to figure out the impact on the anchor cable Vortex-excited fatigue damage lead by the related factors ,this section analyzes the impact on the anchor rope vortex-excited fatigue damage by anchor cable density, the anchor cable length , pre-tension and the flow conditions.

According to the actual marine environment, the annual average flow rate conditions of Qiongzhou Strait are selected. The flow rate is linear shear flow along the depth, the flow rate of the upper of anchor is 1.6 m / s, the flow rate of the bottom of anchor that consolidated with the foundation is 0.2 m/s. According to the S-N curve parameters of the API-X 'curve fatigue analysis, we adopt C = 3.74, b = 2.5e13.

Tab.2. Cable parameters

Sectional diameter (m)	Quality (kg/m)	Density (kg/m^3)	Tension (KN)	Length (m)	Structural damp
0.25	385.1	7850	800	100	0.003

IMPACT LEADING BY DENSITY

This paper adopt three kinds of density, they respectively are ρ_1= 1960 kg/m^3, ρ_2= 3925 kg/m^3, and ρ_3= 7850 kg/m^3, and the anchor cable is simplified to simply supported beam. Tab. 3 shows the anchor rope modal frequency and immeasurable modal amplitude on the condition of three different qualities.

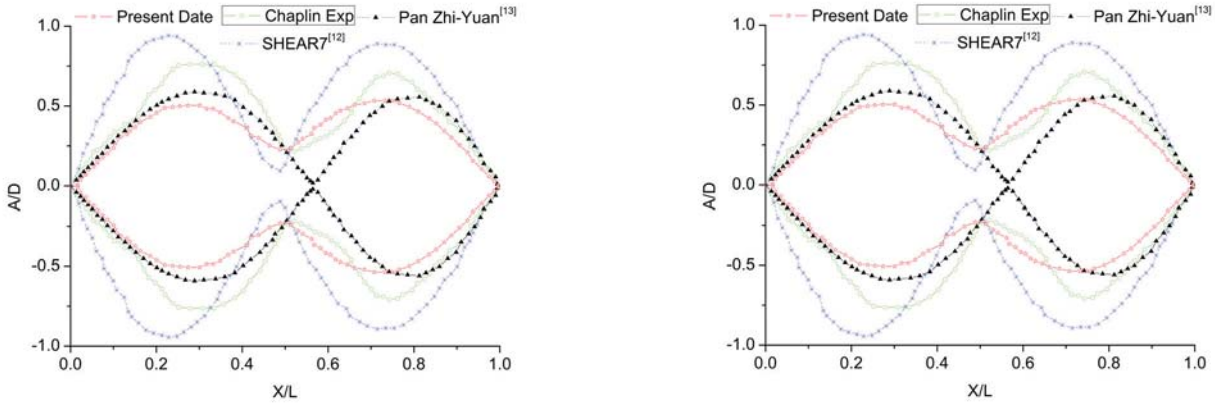

(a) T=405 N,U=0.16 m/s *(b) T=506 N, U=0.4 m/s*

Fig.3. Dimensionless amplitude envelope diagram

Tab.3. Excitation frequency and dimensionless amplitude (modal participation factor)

Incentive mode	2	3	4	5
O_1	0.80/0.34	1.14/0.31		
O_2		0.88/0.56		
O_3		0.65/0.2	0.89/0.28	1.19/0.12

Note: before"/" is excitation frequency and after is the dimensionless amplitude corresponding to the frequency

From Tab.3, Corresponded to the different densities, the main modes and modal participation coefficients are different. As the density increases, the modes (Dominant modal) order that maximum dimensionless vibration corresponding to increases.

From Fig. 4 the peaks of the stress corresponding to different density are different along the anchor rope longitudinal distribution; the number of peak corresponds to the modal number that contributes mostly to the total stress of the anchor cable. In addition, the maximum amplitude of dimensionless vibration modes number is not necessarily the mode that contributes most stress. For example, when ρ1=1960 kg/m3, the second order have the largest non-dimensional vibration amplitude, however, the third mode contributes mostly to the stress, the stress distribution shows three peaks.

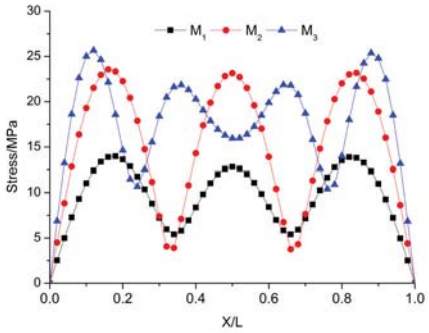

Fig.4. Stress distribution

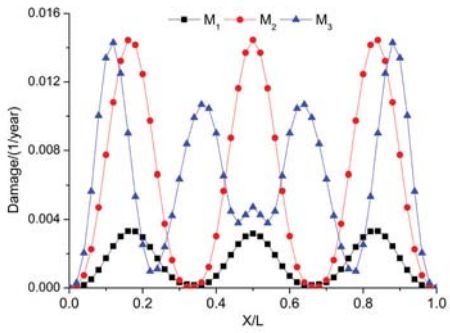

Fig.5. Fatigue damage distribution

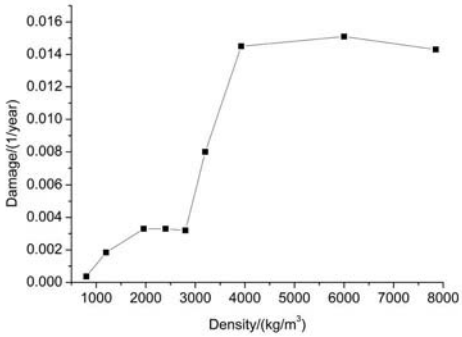

Fig.6. max damage vs density

As is shown in the Fig. 5, the damage is similar with the stress distribution law along the anchor cable vertical distribution, Stress is one of the key factors that affecting the fatigue damage. With the increase of density, fatigue damage is increasing. Thus, in engineering practice, high-strength, low-density material can be adopted so that the fatigue damage of anchor cable can be reduced. Fig. 6 shows the relationship between the anchor cable longitudinal maximum damage and anchor density. As is shown in Fig. 6, the anchor cable damage increases with the density.

IMPACT LEADING BY PRE-TENSION

Taking the anchor cable length L=300 m, other parameters are shown in Tab.2, Comparative anchor cable pre-tension are respectively F_1=800 *KN*, F_2=1600 *KN*, F_3=2400 *KN*. Tab. 4 shows the different anchor cable excitation frequency under different tension and the corresponding dimensionless modal amplitude.

Tab.4-1. F_1=800 KN Excitation frequency and dimensionless amplitude

Incentive mode	10	11	12	13	14
Frequency	0.744	0.798	0.871	0.961	1.03
A_r/D	0.1283	0.239	0.267	0.371	0.427

Tab.4-2. F_2=1600 KN Excitation frequency and dimensionless amplitude

Incentive mode	9	10	11	12
Frequency	0.811	0.885	0.955	1.031
A_r/D	0.249	0.263	0.407	0.425

Tab.4-2. F_3=2400 KN Excitation frequency and dimensionless amplitude

Incentive mode	7	8	9	10	11
Frequency	0.752	0.822	0.907	0.996	1.088
A_r/D	0.242	0.252	0.295	0.334	0.359

From Tab. 4, with the increase of pre-tension of anchor cable, the anchor cable dominant mode number decreases gradually, the dimensionless amplitude of anchor cable

corresponding to major incentive modal have little difference, the form of Anchor cables vortex-induced vibration is a multi-modal vortex-induced resonance.

Fig. 7 and 8 show the longitudinal rms stress under different pre-tension and fatigue damage distribution of anchor.

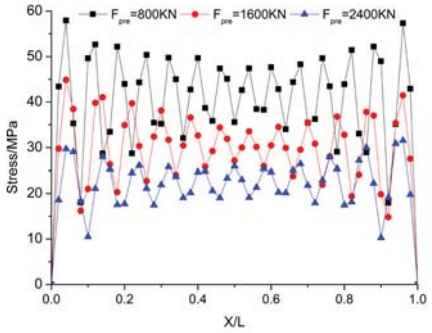

Fig.7 Stress distribution

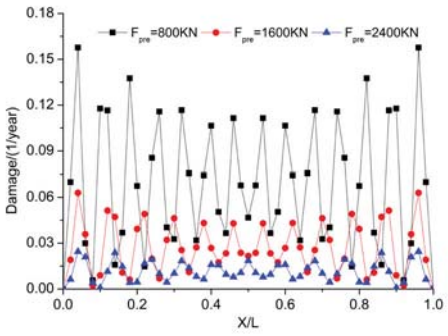

Fig.8 Fatigue damage distribution

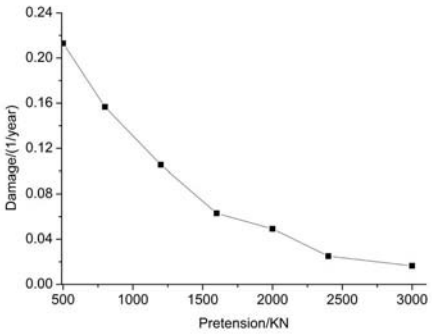

Fig.9. Maximum damage & pre-tension

From Fig. 7, the anchor cables vortex induced vibration stress decreases with anchor pre-tension increasing. Fig. 8 shows that the distribution of the fatigue damage of anchor in vortex-induced is similar with stress distribution, with the increasing of the pre-tension, the different vertical position fatigue damage of the anchor cable decreases, the maximum damage is also reduces. Fig. 9 shows the relationship between the maximum damage of anchor and pre-tension. Fig. 9 shows that: under the premise that in a small pre-tension, the increasing of the pre-tension leads to the increase of anchor frequency, the increasing of frequency leads decreasing of dimensionless modal amplitude that incentive mode corresponds to , the stress that the anchor cable corresponds to and the maximum fatigue damage also reduced.

THE IMPACT OF ANCHOR CABLE LENGTH

Selecting the anchor cable parameters and flow parameters showed in Tab. 2, comparing the anchor cable vortex-induced response and the fatigue damage distribution under the condition that the cable length is 100 m, 200 m, and 300 m. Tab. 5 shows the excitation frequencies of the different length of anchor cable and the corresponding dimensionless mode.

Tab.5-1. L=100 m Excitation frequency and dimensionless amplitude

Incentive mode	3	4	5
Frequency	0.654	0.892	1.186
A_r/D	0.198	0.279	0.121

Tab.5-2. L=200 m Excitation frequency and dimensionless amplitude

Incentive mode	6	7	8	9
Frequency	0.676	0.776	0.866	1.011
A_r/D	0.142	0.251	0.217	0.414

Tab.5-3. L=300 m Excitation frequency and dimensionless amplitude

Incentive mode	10	11	12	13	14
Frequency	0.744	0.798	0.871	0.961	1.03
A_r/D	0.128	0.239	0.267	0.371	0.427

From Tab. 5, with the increase of length of anchor cable, the anchor cables vortex induced impact excitation mode order increased gradually. Dominant modes also increase. Fig. 10 and 11, respectively, show the anchor longitudinal rms stress and fatigue damage distribution on the condition of different lengths of anchor cable.

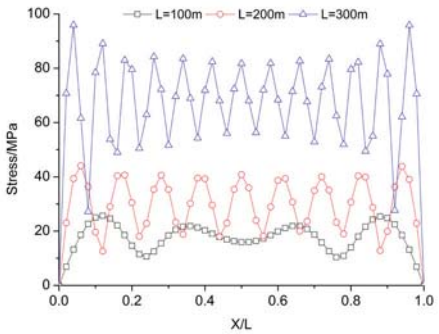

Fig.10 Stress distribution

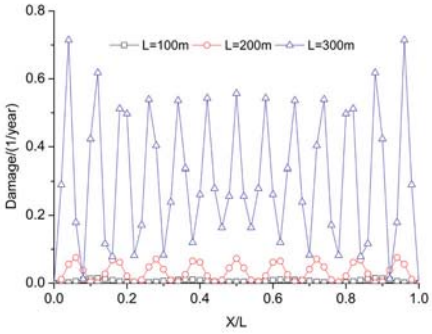

Fig.11. Fatigue damage distribution

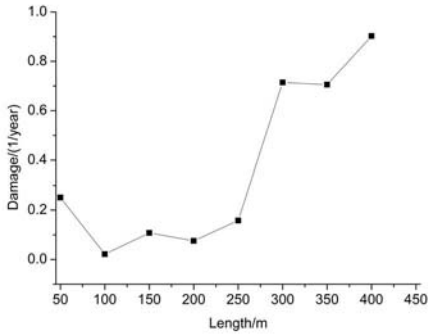

Fig.12. Maximum damage & the cable length

As is shown from Fig. 10 and Fig. 11, with the increase of the length of anchor, the rms stress and damage of anchor longitudinal different positions increase. Fig. 12 shows the relationship between maximum damage and the length of anchor .From Fig.12, in general, Anchor maximum damage increases with the Anchor length increasing, the local gain is not very obvious.

THE IMPACT OF FLOW RATE DISTRIBUTION

This section discusses the impact that shear slope affects anchor cable VIV only under the shear flow condition. It is assumed that the length of anchor cable is 200 m; other parameters of anchor are shown in Tab. 2, and it is assumed that the maximum velocity of the upper of the anchor U_{max} = 1.6m / s, and remains unchanged, Shear rate $\beta=(U_{max}-U_{min})/L$, respectively are β_1= 0.007 (see Tab. 5-2), β_2 = 0.004, and β_3=0.001, the analysis of Anchor vortex-induced response and fatigue damage. Tab. 6 shows the vortex-induced excitation frequencies under different shear rates and dimensionless modal amplitude.

Tab.6-1. β_1=0.004 Excitation frequency and dimensionless amplitude

Incentive mode	4	8	9	10
Frequency	0.796	0.843	0.943	1.034
A_r/D	0.308	0.335	0.454	0.456

Tab.6-2.β_1=0.001 Excitation frequency and dimensionless amplitude

Incentive mode	5	6	9	10	11	12
Frequency	1.039	1.31	1.046	1.064	1.124	1.383
A_r/D	0.697	0.188	0.664	0.704	0.371	0.197

As is shown from Tab. 6, the vortex-induced vibration mode order of anchor cable increases with the decrease of shear rate. Fig. 13 and Fig. 14 give anchor longitudinal rms stress and fatigue damage distribution on the condition of different shear flow rate respectively.

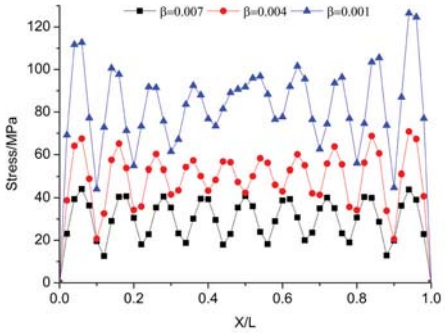

Fig.13. Stress distribution

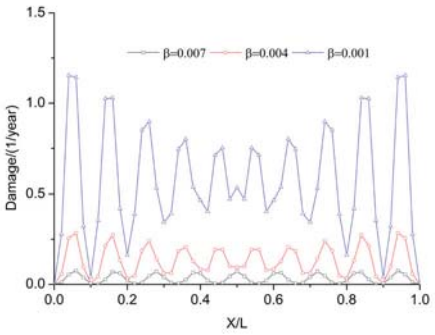

Fig.14. Fatigue damage distribution

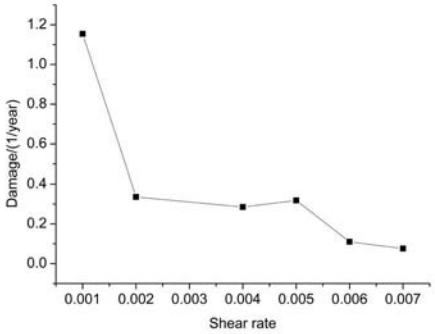

Fig.15. Maximum damage & the velocity shear rate

As is shown from Fig. 11 and Fig. 12, the longitudinal rms stress distribution and the distribution of the fatigue damage of Anchor decreases with the increase of shear rate relatively, with large amplitude from this, it is can be found that the fatigue damage of anchors in vortex-induced is large in uniform flow, is relatively small in shear flow. As is shown from Fig. 15, as the shear rate decreases, the anchor maximum damage is significantly reduced.

CONCLUSIONS

1) With the increase of density of the anchor cable, floating tunnel longitudinal rms stress and fatigue damage reduces, but the damage area changes relatively less.

2) The length of cable affects the anchor cable vortex-induced vibration fatigue damage obviously, as the length increases, the Anchor Cable vortex induced fatigue damage increases, and the range of increasing is large.

3) The impact on the cable fatigue damage from pre-tension is limited, and it is favorable for decreasing the anchor cables vortex induced fatigue damage to increase appropriately the pre-tension; But it should be noted that, with the increasing of the pre-tension, the stress and damage of Anchor also increases correspondingly.

4) The impact on the anchor rope vortex induced fatigue damage from the shear rate of shear flow is very obvious; a weak change from shear rate change will lead to a obvious changes of the anchor rope fatigue damage. Increasing shear rate can significantly reduce the anchor rope fatigue damage.

REFERENCE

1. Blevins, R.D., Flow-induced vibration, Van Nostrand Reinhold, New York, USA, 1990.

2. Chaplin, J.R., Bearman, P.W., Huera, H.F.J., and Pattenden, R.J., *Laboratory measurements of vortex-induced vibrations of a vertical tension riser in stepped current*, Journal of Fluids and Structures, Vol. 21, pp.3-24, 2005.

3. Dong, M.S., Ge, F., Hui, L. *et al*., *Research progress in submerged floating tunnels (in chinese)*, China Journal of Highway and Transport. Vol. 20, no. 4, pp. 101-107, 2007.

4. Gopalkrishnan, R., Vortex induced forces on oscillating bluff cylinders, MIT: Cambridge, MA, USA, 1993.

5. Hu, Y.R., Li, D.Q., and Chen, B.Z., ship and ocean engineering structure fatigue reliability analysis. Beijing, Beihang University Press, 2010.

6. Mai, J.T., Luo, Z.X., and Guan, B.S., *Vortex-induced dynamic response of tension legd for submerged floating tunnel under current effect*, JOURNAL OF SOUTHWEST JIAOTONG UNINERSITY, 2004, Vol. 39, no. 5, pp. 600-604.

7. Meling, T.S., Eik, K.J., and Nygaard, E., An assessment of EOF current scatter diagrams with respect to riser VIV fatigue damage, Proceedings of the 21th OMAE, Paper No. OMAE2002-28062, Oslo, Norway, 2002.

8. Pan, Z.Y., Cui, W.C., and Liu, Y.Z., *The prediction of vortex-induced vibration (VIV) of a slender tensioned riser in a stepped current*, JOURNAL OF SHANGHAI JIANTONG UNIVERSITY, Vol. 40, no. 6, pp. 1064-1068.

9. Trim, A.D., Braaten H., Lie, H., and Tognarelli, M.A., *Experimental investigation of vortex-induced vibration of long marine risers*, Journal of Fluids and Structures, Vol. 21, no. 4, pp. 335-361, 2005.

10. Vandiver, J.K. and Li, L., SHEAR7 program theory manual. Cambridge, MA, Department of Ocean Engineering, MIT, USA, 1999

11. Vandiver, J.K., Research challenges in the vortex-induced vibration prediction of marine risers, Proceedings of the OTC, Paper No. OTC 8098, Houston, USA, 1998.

12. Vengugopal, Madan, *Damping and response prediction of a flexible cylinder in a current*, Ph.D.Thesis submitted to Dept. of Ocean Eng. MIT. 1996.

13. Vikestad, K., (1998) *Multi-frequency response of a cylinder subjected to vortex shedding and support motions.* Ph.D. dissertation, Department of Marine Structures Faculty of Marine Technology, Norwegian University of Science and Technology

CONTACT WITH THE AUTHOR

Gang Luo
Jianxun Chen

School of Highway,
Chang'an University,Xi'an
Shaanxi 710064
CHINA

tel.:+00862982332897, fax: +00862982332897

Xiaojun Zhou

School of Civil Engineering
Southwest Jiaotong University
Chengdu 610031
CHINA

POLISH MARITIME RESEARCH 4(88) 2015 Vol. 22; pp. 84-92
10.1515/pomr-2015-0076

TRUSS HARBOR CRANES MODAL DESIGN ELEMENTS RESEARCH

Mariusz Żółtowski, Ph. D.
Michał Liss, Ms. C.
Bogdan Żółtowski, Prof.
Josef Melcer*, Prof.
University of Science and Technology, Poland
*) University of Zilina, Slovakia

ABSTRACT

Dockside cranes must meet the relevant strength requirements that provide usefulness and not endanger the safety of their use. The vibration effect on structural safety hazard results from the impact of horizontal forces caused by the transport of goods for loading and transverse forces caused by wind, which can be dangerous for correct functioning. In addition, there are often serious effects of climate-related impacts of the environment, material fatigue, which actuates the degradation state of the object. Dynamic loads may therefor cause random effects that devastate the structures or lead to their catastrophic destruction.
Recognizing the need to improve the testing methods of crane structures in order to assess their condition and assess their safety factors - this paper attempts to develop a methodology for testing the degradation of the selected portion of a construction crane - using experimental modal analysis, realized in simulation tests in the Inventor environment as well as at test stand research.

Keywords: construction vibrations; state of degradation; modal analysis; stabilization diagram

INTRODUCTION

Dock crane operational loads (lifts) are most often random, making it difficult for an indirect assessment of changes in their dynamic state of condition for their safe use. Today, there is a tendency to shorten the time for determining the destruction status of the tested structure by giving up some difficult experimental studies in favor of computer simulations. Experimental studies are used to verify the simulation models by comparing the results of computer simulation and physical experiment. To determine the variation of loads, the dynamic models as a system of rigid bodies are used, in which operating conditions of work of these structures are simulated [4,7,9,14].

In the method of measurement for determining the variable load, waveforms of acceleration or deformation at selected points of the structure are recorded, that are a response of the system to operational loads. Direct measurement of operational loads is very difficult and expensive, and often almost impossible. Often the determination of operational loads is carried out indirectly by means of computer simulation of a structure model, in which values are taken of the measured waveform of model answers at points corresponding to the measuring sensors on the structure [1,2,3,5].

The dynamics of truss design elements has been described and verified in part in research of this work using techniques of modal analysis. Modal analysis is widely used in the study of damage caused by vibration, structural modification, update of the analytical model, control of the state and is also used to monitor vibration in aerospace structures and mechanics of civil engineering [6,15,17,22]. Often already used in various applications, modal analysis is a technique for the study of dynamic properties of some elements, using modal model parameters, consisting of modal frequencies, damping and vibration shapes [17,25].

This paper presents the dynamical properties of structural elements of port crane test procedure, taking into account the simulation tests and their verification at test stand. The analysis results of simulation studies using theoretical modal analysis in Inventor computational environment for the selected truss fragment, which is an equivalent to the components used in the construction of port cranes, had been verified at test stand using this experimental modal analysis [5,17,23].

VIBRATION IN CONSTRUCTION DISCRIPTION

One of the basic criteria used in the design of modern crane construction is its dynamic properties. They have a direct impact on the vibration level, emitted noise, fatigue strength and stability of the structure. Analysis of dynamic properties, in most cases encountered in practice is made on the basis of the behavior of the construction model [8,10,17], as studies of real objects is not always possible. Model design

can be created in the process of transformation of analytical formalism used to describe the dynamics of the system, or on the basis of experiment results performed on the real object [11,16,21]. In the latter case the obtained function test object (of any structure), which is a function approximating the results (measurement). This function has important practical significance, because it can be useful to optimize the test procedure (test conditions, the number of parameters, number of ii repetitions). It also has cognitive significance because it can be transformed into a functional model of the object by means of adequate logical reasoning, using deductive methods. Such a model should reliably (adequately) reflect the construction answers (stress, displacement) treated by any dynamic load. The dynamic load is a load which value, direction, turn or touchdown place change over time [12,18,23]

The study pointed out such major problems occurring at the design stage of construction, as:

- determination of static and dynamic loads acting on individual nodes and elements of design,
- determine the stress distribution in selected areas of computed design,
- selection of the most loaded elements and to estimate their strength and durability (operational reliability).

Particular attention was paid to determine the course of the nature of the change and the value of extreme dynamic loads in the proposed structure. This approach was deemed important because of the accuracy of the designation of the status of the load depends the correctness of the design calculations, and as a result the reliable operation, as well as operational advantages (durability, running costs) and the cost of fabrication.

The basic step in analyzing the dynamics of an object is usually the determination of frequency vibrations of structural elements (i.e. the spectrum of vibration test pieces or set). Typically it is observed that random vibrations with these frequencies in the structure are subject to rapid dampening. But there is always the risk of a build-up of vibration, when external impacts (deterministic or random) in their structure may also include forcing frequencies close to the natural frequency of the structure.

The most dangerous states of dynamic loads associated with the extreme values of the stresses arise in the area of resonant vibration, the lowest frequencies of own construction. Such conditions may occur, for example: during a high-speed (displacement) in the environment of construction of climate impacts, wind, temperature, or passing vehicles. Usually occurring at the change in load structure nodes are transient processes of a fading amplitude [14,19].

With this in mind to determine the structure of dynamic loads, methods of their physical and mathematical modeling were applied - Fig.1. Methods of physical modeling were used for the test structural models at laboratory stands and during specially prepared polygon tests. Laboratory tests allow for a significant reduction in the duration of the experiment in relation to polygon testing. It is also easier to keep the repeatability of test conditions [3.22].

To describe the dynamics of construction, structural models were used, which were built in accordance with the finite element method. However, models constructed this way, in particular for the purpose of dynamic analysis, gave approximate results which use is very limited. They require some fine tuning on the basis of knowledge of the properties measured on the real object [17].

Fig.1. View of port crane and recording results of the dynamic state of using vibration

The model allowed determination of structural modal model which is a set of natural frequencies, damping factors and their corresponding vibration shapes – by use of suitable coordinate transformation model. Modal model can be further identified on a real object on the basis of identification experiment [6.22].

Use of the information contained in the vibration image (described by estimators determined vibration) of the desired fragment or the whole building structure is the concern of structural vibration diagnostics. In this area was the main issues of the presented study have been located [3.23].

In this study the vibration signal is the basis for the study of destruction specific port construction and many ancillary procedures for solving the task at excelling in the field of vibration engineering construction. In this paper information in the field of vibration will be recalled many times further in the text, particularly in the description and acquisition of signals, determining the vibration estimators and statistical processing of results for the destruction of selected studies of mechanical structures or parts (elements) of building structures [23].

System vibrations arising from violations of the equilibrium position of an object under the influence of: the elastic forces, the forces of gravity or friction, which are free vibrations have been studied for system with one degree of freedom. It is assumed here that violation of the equilibrium position is characterized by initial conditions: the initial position x_0 and initial velocity v_0. He the simplest model of an examined the technical system was considered - a system which has one degree of freedom (one mass m) and has linear characteristics of elasticity (k) and damping (c) - Fig.2, and a harmonic driving force F (t) works on it. The equation of motion is expressed as the formula:

$$m\ddot{x} + c\dot{x} + kx = F(t) \quad (1)$$

It shows that the systems' with one degree of freedom own vibration with are completely determined by the vibration frequency. The amplitude of the vibration depends on the

initial conditions, and the own frequency and the oscillation period of them are independent.

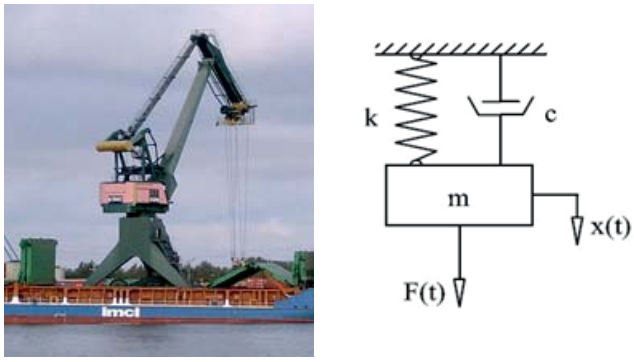

Fig.2. View of the crane, as an object of the modeled system with one degree of freedom

The parameters appearing in the description (1) of the model $\ddot{x}$, $\dot{x}$, x - are the process parameters of the vibration (a, v, x), which argues that the vibration describe the state of the structure well.

In the low frequency range, the structures can be modeled by discrete systems with several degrees of freedom, and often with one degree of freedom. Therefore, it is assumed that, in practice, the system shown in Figure 2 may also be a model of [6,22]:

- a construction machine of mass m on shock absorbers (k, c) attached to the foundation of high molecular weight.
- working machine (vehicle) of mass m on shock absorbers (k, c) moving on the ideally flat way,
- high building construction (cranes, chimneys, towers) exposed to the wind force.

In the first approach, these research objects can modeled by a system with one degree of freedom, and its properties looked up by mathematical description and analysis of the equations describing it, examine them in the way of measuring the parameters of vibration ($\ddot{x}$, $\dot{x}$, x), which as a result of solutions describe a mathematical model interchangeably describe the same property, but from the side of the measuring system vibrations. In industrial practice, vibrations are commonly measured, avoiding complicated theoretical considerations [17,22].

During operation of the afore mentioned structures, due to the existence of a number of external factors (environments enforcement, forces of other structures) and internal (aging, wear and tear, elements co-functioning) followed by disorders of equilibrium states, which propagate in the elastic center - material which is used to build the structure in question. These disorders are dynamic and keep the conditions of equilibrium between the state of inertia, elasticity, damping and extortion. As a result, this causes the dissipation of energy of waves, the diffraction, dampening, and overlap. The existence of the sources and the spread of disorder causes the vibration of structural elements and the surrounding environment [22]. These phenomena have been mapped in the vibrational interaction model presented further.

As a result of the existence of the input and execution states representing transformation processes taking place in the structure, a number of symptoms (signs) is formed giving a measure contained in the processes starting from the structure. These processes are also the basis for building a model of signal generation, determining the method of construction, operation and description of changes in the destruction of the object [6.17]. Features of the transition vibration signals model for structures subject to random distortions are based on assumptions:

- condition of the structure is determined uniquely by the characteristic signal $\varphi_i(t,\theta)$, generated separately with each forcing. This signal changes over dynamic time (short) "t" and the evolution in their spare time (long) „θ„.
- characteristic signal is comprised of a determined process φ_o and random n, and its intensity change condition is characterized by destruction of the structure.
- the transformed characteristic signal which is a mapping of internal interactions - the degradation of structure - is perceived as y(t,θ) and in the simplest case is the response of the test structure element of the characteristics h(t,θ) to force x(t,θ). Considering the vastness of space (dimensions) the "r" of the construction of such a signal can be written as:

$$y(\theta,r) = \sum_{i=1}^{\infty} \varphi_i(t,\theta,r) * h(t,\theta,r) * \delta(t - iT) \quad (2)$$

- output processes from the construction (selectively) influence back upon the processes of destruction and continually on the state of the building (element) by the positive disruptive feedback, distorting the original signal $\varphi_i(t,\theta)$.
- for a fixed value of operational time θ_i = const all building objects are treated as linear and stationary systems, which properties are described by the impulse response h(t,θ,r) or their transforms: Laplace operator H(p,θ,r) or Fourier spectrum H(jω,θ,r).

The described sequence of the assumptions leading to signal generation model are shown in a block diagram form in Figure 3.

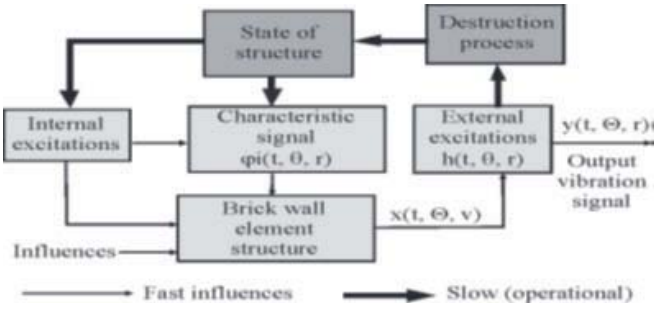

Fig. 3. Block diagram of the signal pass through the construction test piece

The modeling assumes that the vibration signal output from any point of receipt may be expressed by the formula [6.22]:

$$y_k(\Theta,r) = \sum_{i-1}^{k} a(k)h_i(t,\Theta,r) * [u_i(t,\Theta,r) + n_i(t,\Theta,r)] \quad (3)$$

where:

- impulse transition function h(*) taking into account the destruction properties of the material,
- a(k) gives different summation weight related to the place of receipt "r"

Presented in the form of equation (3) the method how to interpret the output signal y(t,θ,r) is true in the general case of excitations of objects of timed period work, but not always so simple as in figure 4, which shows the formation of random excitations from the effects of wind on high buildings, chimneys, towers and recording responses in the form of a complex vibration signal.

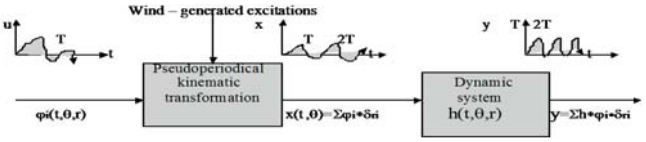

Fig. 4. Schematics of the characteristic signal transformation φi(*) for the output signal y(*) as a generation model of the signal in buildings by environmental forcing[6]

The modeling also takes into account the fact that the received signal output anywhere in the design is a weighted sum of the answers to all elementary events φi (t,θ,r), always occurring in the same sequence at specific points on the pulse of the dynamic transfer function h(t,θ,r). These effects add up and are further transformed along different axes of reference, with the change of signal reception "r" is also connected with the change of the transmittance.

The designed vibration signal transition thru the test piece of the structure model has been described by the FRF function - marked out in experimental modal analysis, as the ratio of excitation of vibration force at the input to the amplitude of the vibration acceleration on the output. The inversion of FRF function is transmittance H(f), defined as the ratio of response to force [6.23].

The indicated properties of the created vibration processes thru researched structures transition model have been used further to assess changes in the degree of degradation of the structure part, by examining the transition vibratory signals through the various structures of the modeled components or units of the structure.

IDENTIFICATION OF CONSTRUCTION STATE

The aim of the dynamics study of a complex system of lifting structure is to assess the dynamic loads, reflecting the state of degradation and predict the correct behavior time of the system. With the increase of load, increased requirements for durability and reliability, as well as in many cases the need for non-deconstructional assessment of degradation, the importance of analyzing structural dynamics increases [6.23]. Changes in the degradation of the construction of buildings reported by a vibration signal reflect in fluctuating levels of vibration or a change in transmittance, or FRF from the point of extortion to the collection point.

Quality tests of degradation the state is carried out using the methods of identifying, using the assessment of changes, respectively, resonance frequency, amplitude and attenuation coefficients in those frequencies.

For complex systems, often nonlinear, for the purpose of identifying the degradation of construction - modal analysis is used. As a result of its implementation, the modal model based on stabilize diagram is obtained, which is an ordered set of own rates, the corresponding coefficients of damping and own vibration shapes. Based on the knowledge of modal model the object response can be predicted for any disorder in both time and frequency domains [17,25].

Modal model parameters allow the decoupling of equations describing vibrations of the system, and their values are determined from the relation [17,23]:

$$m_r = \frac{1}{2j\varpi_r R_{ir}} \quad k_r = \varpi_{nr}^2 m_r \quad c_r = 2m_r \varpi_{rn} \delta_m \tag{4}$$

These values describe the properties associated with r - the own frequency and changes of the own frequency depend directly proportional to the amount of change of stiffness or mass, and also depend on the place of failure increase in the structure [17,22,23].

In practice, the following types of modal analysis are distinguished[17]:

- theoretical, which requires the solution of its own issue for the adopted structural model of the object;

The theoretical modal analysis is defined as an own matrix problem, depending on the mass matrix, rigidity and damping. Theoretical modal analysis requires addressing the own issue for the adopted structural model of the tested structure [13,21]. Designated collections of own frequencies, the damping factors for own frequencies and forms of own vibrations allow the simulation of structural behavior at any extortion, selection of controls, construction modifications and other.

The analysis of own frequencies and own vectors is obtained from the equations of motion (after skipping the matrix containing the damping parts and the vector of external loads). Then, the equation of motion vibrations is as follows:

$$B\ddot{q} + K\ q = 0 \tag{5}$$

In reference to a system with one degree of freedom, the solution has the form of a function:

$$q(t) = \vec{q}\sin\ \varpi t + (\varphi) \tag{6}$$

where $\vec{q}$: - amplitude vector of own vibrations

After inserting the above equation, and the second derivative into the equation of motion, the following is obtained:

$$(-\varpi^2 B + K)\vec{q}\sin(\varpi t + \varphi) = 0 \tag{7}$$

The above equation must be fulfilled for any time t - then this gives a system of algebraic equations:

$$(K-\varpi^2 B)\vec{q}=0$$
$$\begin{aligned}
&(k_{11}-\omega^2 m_{11})q_1+(k_{12}-\omega^2 m_{12})q_2+\cdots+(k_{1n}-\omega^2 m_{1n})q_n=0\\
&(k_{21}-\omega^2 m_{21})q_1+(k_{22}-\omega^2 m_{22})q_2+\cdots+(k_{2n}-\omega^2 m_{2n})q_n=0\\
&\cdots\quad\cdots\quad\cdots\quad\cdots\quad\cdots\\
&(k_{41}-\omega^2 m_{41})q_1+(k_{42}-\omega^2 m_{42})q_2+\cdots+(k_{nn}-\omega^2 m_{nn})q_n=0
\end{aligned} \tag{8}$$

It created a homogeneous system of linear algebraic equations, which has a nonzero solution only if:

$$\det(K-\varpi^2 B)=0 \tag{9}$$

Multiple roots may appear among roots and a vector formed by a set of frequencies in order of increasing values is called the frequency vector. The first frequency is called the fundamental frequency [21].

$$\varpi=[\varpi_1,\varpi_2\ldots\varpi_n,] \tag{10}$$

Theoretical modal analysis is used mainly in the design process, when there is no option of studies on the given object.

- experimental requiring controlled identification experiment, during which oscillation of the object is forced; the force and the response in one or a plurality of points arranged on the examined object is measured;

Identification experiment in experimental modal analysis (Fig. 5) involves forcing the vibration of an object with a modal hammer and simultaneously measuring the exciting force and system response, usually in the form of the spectrum of vibration acceleration.

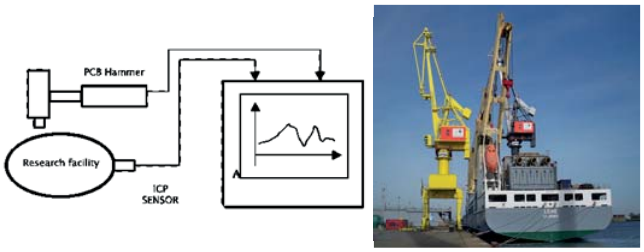

Fig. 5. The essence of research in experimental modal analysis

The modal model (natural vibration frequencies, vibration and damping forms) is obtained from the stabilization diagram and software presented vibration form animation. These data allow to determine the characteristic frequencies of vibration which are subject to fluctuations during the degradation state while in use and that indicates the progress of the processes of destruction of the structure.

- operational, based on operational experiment, in which measurements are made only for system response in a number of measurement points, while the movement of the subject is due to the actual operating extortion.

It is used to identify objects of large-scale spatial dimensions and large masses, and is based on the measurement of the response to the operating force, as a result of external forces (picture 6), or kinematic extortion and the process of destruction of building elements [22,25].

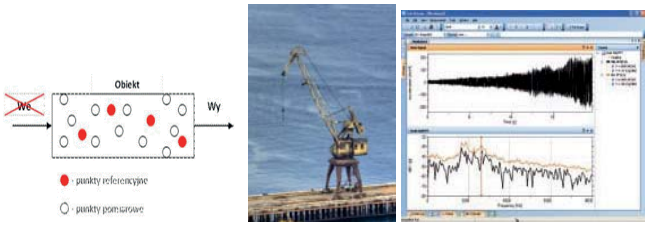

Fig. 6. The essence of operational modal analysis

Operational modal analysis:

- allows for modal analysis of large-sized objects, for which the laboratory tests would be difficult to implement.
- modulates objects correctly as extortions correspond to the actual loads due to their time span, spatial distribution, amplitudes and boundary conditions.

In practical use so far, operational modal analysis was used to diagnose trusses (masts, antennas, cranes), the diagnosis of turbine set and to diagnose the quality of bridge structures. In most of these applications, it is assumed that as a result of damage, locally structural rigidity changes, which causes changes parameters of the modal model. By tracking changes of vibration forms, an area can be specified in which there is significant destruction [17].

THE ANALITICAL TOOL IN THE AUTODESK INVENTOR ENVIRONMENT

Modal studies aim to determine dynamic properties of truss elements commonly used in the construction of harbor cranes to indicate possible opportunities to diagnose and even modify these properties through structural changes, which would ensure high durability of these objects.

To perform a modal analysis of truss design, a three-dimensional model of its selected fragment was created. Truss structures consist of appropriate types of profiles or separable/inseparable connected links profiles. Selected truss fragment of harbor cranes model was done (in the Inventor software), which has been joint with geometric relations, according to the nature of the interaction between these elements. Such created system was analyzed by the module "Stress Analysis". This analytical module is equipped with a possibility of using the finite element method in order to improve theoretical modal analysis. Preparations preceding calculation step include:

- defining how to support the test piece,
- conversion of the bonds resulting from the assembly and method of assembling the various elements to determine the number of vibration forms.

Depending on the type of connection present between the elements of the construction bonds they have been replaced by so-called contact bond for static connections and spring-type contacts for flexing connections. Contact bond is related to bonding material equivalent to combined elements such as.: welds. In contrast, the spring-type contact

bond allows you to enter between adjacent surfaces a no elastic mass element of stiffness ratio which is determined by the user. When modeling, the phenomenon of damping in the case of flexing connections is omitted, with the result that the model is greatly simplified. Fig. 7 shows the actual and modeled portion of the construction crane model tested using theoretical modal analysis.

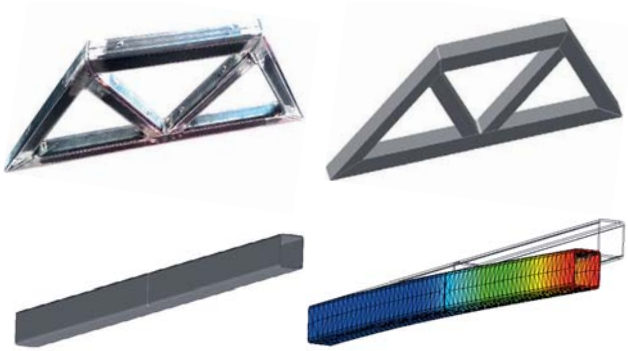

Fig. 7. Actual and theoretical model of the tested truss element

The fragment of the construction crane created in such a way in the Inventor environment was subjected to simulation calculations, which generate a report containing information about the task analyzed and simulation results are presented in a graphical form. The results are presented in the form of layering maps, graphically depicting forms of free vibration of a tested segment, along with an array containing frequency values corresponding to the measured vibration forms. The program also allows to carry out animation of obtained deformations that occur during the free vibration of each of the observed forms.

RESEARCH RESULTS

In the framework of the implementation of theoretical calculations using the method of modal analysis, characteristic vibration frequencies were generated for a given segment of a lifting structure, which are summarized in Tab.1. During the simulation, the number of designated natural frequencies was limited to 20.

Tab. 1. Frequency of own vibrations generated using theoretical modal analysis

F1	F2	F3	F4	F5	F6	F7	F8	F9	F10
[Hz]	[Hz]	[Hz]	[Hz]	[Hz]	[Hz]	[Hz]	[Hz]	[Hz]	[Hz]
71,29	289,40	345,10	350,83	792,55	904,46	995,99	1063,37	1063,84	1168,01
F11	F12	F13	F14	F15	F16	F17	F18	F19	F20
[Hz]	[Hz]	[Hz]	[Hz]	[Hz]	[Hz]	[Hz]	[Hz]	[Hz]	[Hz]
1273,96	1373,37	1577,62	1702,82	1814,78	1847,73	1930,23	2076,51	2290,80	2357,98

Frequency and forms of own vibrations resulting from simulation allow to identify the most dynamically vulnerable areas of a given construction segment. This knowledge can be used to modify the test structure to improve its rigidity in sensitive areas. This information also can be used to determine the current technical condition of the structure and in the case of knowledge of previous states it is possible to develop and implement appropriate diagnostic procedures. A few examples of the form of vibrations have been graphically presented below.

Figure 8 presents the first embodiment of a vibration form at a frequency of 71.29 [Hz]. Vibration at low frequencies reflecting the focus maximum energy of destruction should be of particular interest to engineers. They usually have a very significant impact on the durability of the whole construction. In the case of the analyzed object that was left-restrained, the embodiment of these vibration has bending characteristics.

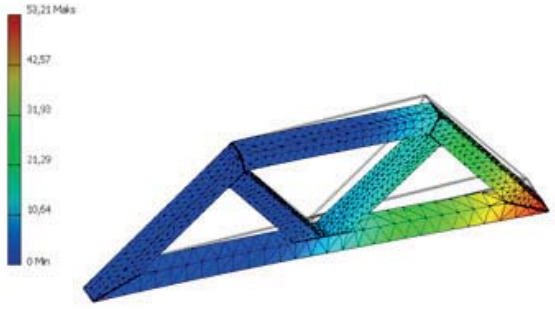

Fig. 8. The bending vibrations of the truss welded at a frequency of 71.29 [Hz]

Truss structures in theory are treated mostly as a type of thin-walled structures. In these constructions, in addition to the bending stresses occur much more dangerous stresses derived from a constrained torsion, also called sometimes a bimoment. Therefore, in the case of such structures, own vibrations of torsion or torsion - flexural nature are more important. Usually such forms of vibration of this nature occur in slightly higher frequencies - fig.9.

The first form of vibrations of a torsion - flexural nature occurs at a frequency of 1000 [Hz]. This form can be triggered by both the normal stress of which constrained twisting may appear, as well as touching, which can be induced by transverse forces (shear) or torque.

The free twisting of steel profiles can be defined as a certain deformation, by which the distance of the two sections before and after the deformation is the same. This would mean that the elongation of individual fibers and longitudinal stresses are zero.

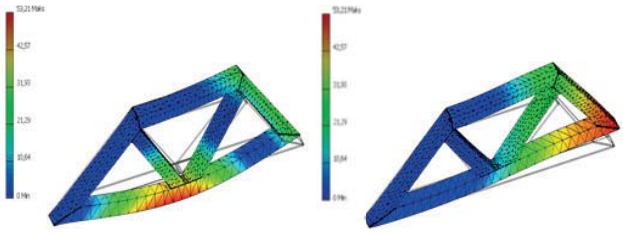

Fig. 9. Examples of two following forms of own vibrations of the truss structure of a flexural frequencies sequentially 289.40 [Hz] and 345.10 [Hz]

The situation is different in the case of a constrained torsion, wherein the distance between the cross-sections before and after deformation is different, and the longitudinal fibers change their original length - figure 10. In the analyzed example, it was not observed among 20 normal own vibration forms, such ones representing torsion or torsion - flexural form similar to the definition of non-constrained twisting.

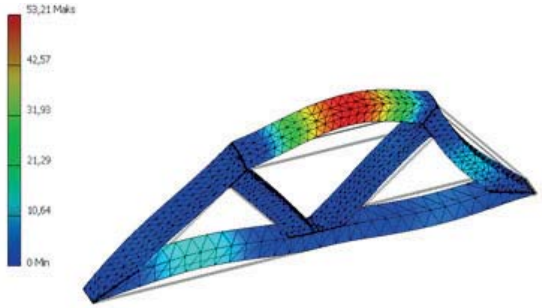

Fig. 10. The first embodiment of a torsion – flexural vibration form at a frequency of 995.99 [Hz]

The precise analysis of natural own vibration forms provides very thorough knowledge of the dynamic state of technical objects, which requires a combination of knowledge from several other fields of technical sciences - particularly the principles of diagnosing the machinery state [22].

The need to verify the results of simulation studies on a real piece of truss model (Figure 8) justifies the need to identify the best way of suspension of truss during the modal experiment, to limit the number of degrees of freedom. The completed studies looked at four different approaches to suspend an object of research in experimental modal analysis, the essence of which represents Fig.5. The adopted solutions analyzed in the active experiment [22,25] are:

a) object suspended on the fishing line,
b) the object suspended on luggage cords (fig. 11)
c) the object suspended on chains,
d) object suspended on chains with rubber elements.

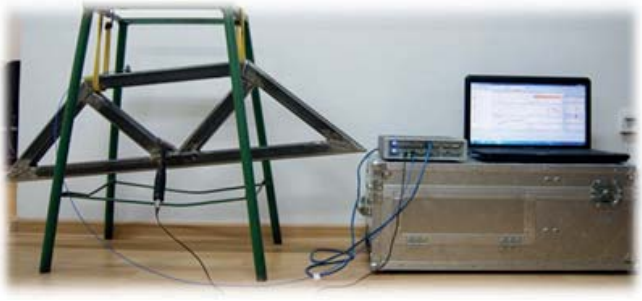

Fig. 11. Schematic view of a truss suspended on luggage cords

The test results were evaluated using the AutoMAC coefficient [17] and analysis of the various own vibration forms, enabling selection of the best modal parameters of individual types of suspension. The results of the tested methods of suspension are summarized in Table 2.

Tab. 2. Summary of modal parameters for the test cases of the suspended test object

	Modal parameters							
	Solution A		Solution B		Solution C		Solution D	
	Frequency	Damp. factor	Frequency	Damp. factor.	Frequency	Damp. factor	Frequency	Damp. factor
	[Hz]	[%]	[Hz]	[%]	[Hz]	[%]	[Hz]	[%]
Form 1	279.463	0,00	281.230	0,02	280.402	0,03	280.222	0,10
Form 2	752.122	0,03	747.881	0,26	740.045	0,10	756.716	0,59
Form 3	1405.607	0,05	1406.599	0,29	1022.556	0,04	1405.092	0,14

The results were compared with results of simulation studies derived from modal analysis done in Autodesk Inventor software. Tab. 3 summarizes the results with the percentage of showing the difference in the results obtained in simulation and experiments. Based on these results it can be concluded, that the impact of the suspension on the method of measurement results obtained in most of the analyzed cases does not have so much significance.

Tab. 3. Summary of results and Autodesk Inventor software results

	Modal parameters								
	Solution A		Solution B		Solution C		Solution D		Inventor
	Frequency	Difference	Frequency	Difference	Frequency	Difference	Frequency	Difference	Frequency
	[Hz]	[%]	[Hz]	[%]	[Hz]	[%]	[Hz]	[%]	[Hz]
Form 1	279,46	0,14	281,23	0,49	280,40	0,19	280,22	0,13	279,86
Form 2	752,12	0,06	747,88	0,50	740,05	1,54	756,72	0,68	751,64
Form 3	1405,61	1,05	1406,60	0,98	1022,56	28,02	1405,09	1,09	1420,55

All received and selected modal parameters describe the analyzed object at good degree. The only exception is the solution C, which makes it impossible to enforce all forms of vibrations. In further studies of this work, carrying out research using experimental modal analysis, research object was suspended on the fishing line.

Experimental verification obtained in simulations for the indicated model frequencies and form shapes was realized in the idea shown in Figure 12.

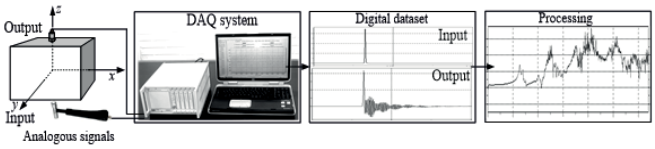

Fig. 12. The idea of determining the parameters of the dynamic crane construction

For the measurement waveforms of extortion and system response times of the studies system and defining the function of the FRF, LMS TEST.XPRESS companies measurement equipment was used. This software enables you to easily perform a modal analysis of structural elements, such as any building structures. The program has an easy and pleasant user-friendly interface - figure 13.

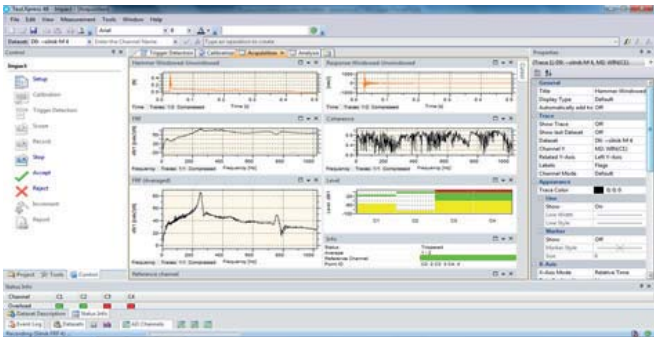

Fig. 13. The main dialog window during tests

In the model test of a truss fragment (Fig. 8) extortion and answers and programmatically determined FRF transition functions, as well as diagrams of stability were recorded. The acquired own vibration frequencies and these forms of vibrations were compared with the results of the theoretical modal analysis. Figure 14 shows an example of the results of the research function of the FRF, and Fig. 15 – a sample diagram of stabilization.

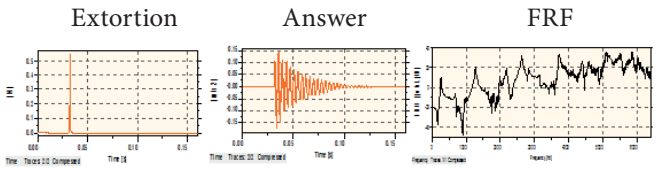

Fig.14. Timing of extortion, responses and FRF functions for the modeled construction crane fragment

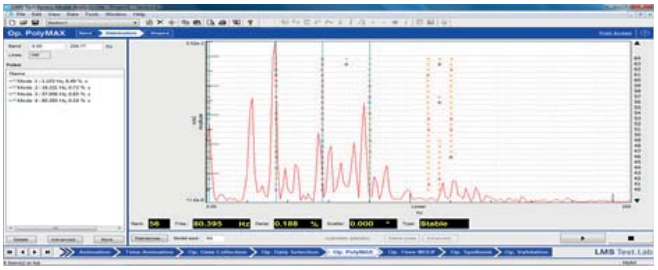

Fig. 15. Stability diagram for the modeled construction crane fragment

The results of theoretical modeling in simulation model and their researchs tand verification of the model of the truss, gives evidence to the research methodology of complex objects vibration modal analysis methods and form the beginning and preparation for a wider variety of real objects.

FINAL CONCLUSIONS

The search for methods of non-destructive testing of different port structures indicate the possibility of using modal analysis in the assessment of their degradation, which, for example, for a lifting structure are presented in this paper. With different varieties available for forms of modal analysis, theoretical and operational modal analysis was used here in the study of destruction.

The results of preliminary studies point to the fact that it is possible to distinguish between material properties of a lifting structure, which has an impact on the ability to distinguish their mechanical properties. The study also confirmed the usefulness of Inventor software to recognize degradation using theoretical modal analysis performed on structural elements of modeled port cranes.

With the presented considerations and the results obtained, the following summary comments can be offered:

- resonance frequency for the modeled lifting element was generated,
- it was agreed that a change in working conditions for the lifting element causes an increase in the frequency of own vibration, which proves the usefulness of this method for the assessment of degradation in the quality of construction,
- the importance of a particular character of vibration form of the sensitivity debit lattice structure was highlighted.

The research results point to the fact that it is possible to distinguish between ownership of degradation in the crane structures, which affects the ability to assess threats and their mechanical properties. Stand and operational testing of equipment confirmed the usefulness of the LMS devices and the use of Inventor software to implement modal analysis at the actual building construction.

The practically verified susceptibility of modal analysis for the degree of degradation of a fragment of crane structures shows to the satisfaction of practical application, the differences between the functional and damaged structure. Thus, it becomes possible to determine the risks of building structures (port) on the basis of the study of the own vibration frequencies values and their form using modal analysis.

BIBLIOGRAPHY

1. Batel M.: Operational modal analysis – another way of doing modal testing. Sound and Vibration, August 2002.

2. Bishop R., Johnson D.: The mechanics of vibration. Cambridge University, Press, 1980.

3. Brandt S.: Data analysis (in Polish). Wydawnictwo Naukowe PWN (Scientific Publishing House), Warszawa 1999.

4. Brown D., Allemang R.: Multiple Input Experimental Modal Analysis. Fall Technical Meeting, Society of Experimental Stress Analysis, Salt Lake City, UT, November 1983.

5. Brunarski L.: Non-destructive methods for concrete testing (in Polish). Arkady, Warszawa 1996.

6. Cempel C.: Vibroacoustical Condition Monitoring, Ellis Ltd., Chichester, ¬New York, 1991.

7. Dzida M., Olszewski W.: Comparing combined gas tubrine/steam turbine and marine low speed piston engine/steam turbine systems in naval applications. Polish Maritime Research, No.4 (71), Vol.18, 2011.

8. Formenti D., Richardson M.: Parameter estimation from frequency response measurements using rational fraction polynomials (twenty years of progress). Proceedings of International Modal Analysis Conference XX, February 4-7, 2002, Los Angeles, CA.

9. Girtler J., Korczewski Z., Mańczak J.: Operational problems of large power diesel engines combusting biofuels, considered together with assessment of their operation. Polish Maritime Research, No 2 (65), Vol. 17, 2010.

10. Ibrahim S., Mikulcik E.A.: Method for the direct identification of vibration parameters from the free response. Shock and Vibration Bulletin, Vol. 47, Part 4, 1977.

11. Peeters B., Ventura C.: Comparative study of modal analysis techniques for bridge dynamic characteristics. Submitted to Mechanical Systems and Signal Processing, 2001.

12. Pickrel C.R.: Airplane ground vibration testing – nominal modal model correlation. Sound and Vibration, November 2002.

13. Richardson M.: Is it a mode shape or an operating deflection shape? Sound and Vibration, February 1997.

14. Richardson M.: Structural dynamics measurements. Research Studies Press, Ltd. Baldock, Hertfordshire, England, December 2000.

15. Rudnicki J.: The evaluation of the vibration measurement usability of electronic indicator LEMAG „PREMET C". Journal of Polish CIMAC, Vol. 7 No. 2, Gdańsk, 2012.

16. Shih C., Tsuei Y., Allemang, R., Brown D.: Complex mode indication function and its applications to spatial domain parameter estimation. Proceedings of International Modal Analysis Conference VII, January 1989.

17. Uhl T.: Computer-aided identification of mechanical structure models (in Polish). WNT (Scientific Technical Publishers), Warszawa 1997.

18. Williams R., Crowley J., Vold H.: The multivariate mode indicators function in modal analysis. Proceedings of International Modal Analysis Conference III, January 1985.

19. Vold H., Schwarz B., Richardson M.: Display operating deflection shapes from non-stationary data. Sound and Vibration, June 2000.

20. Vold H., Kundrat J., Rocklin G.A.: Multi-input modal estimation algorithm for mini-computers. S.A.E. paper No. 820194, 1982.

21. Żółtowski B.: The investigations aid in exploitation. Liptowski Mikulesz. XI International Technical degradation Conference. ISSN 1642-347X-1, Słovakia, 2012.

22. Żółtowski B., Cempel C.: Engineering of diagnostics machines. PTDT, ITE – PIB, Radom, ISBN 83-7204-414-7, 2004 s.1109.

23. Żółtowski M.: Modal analysis in the testing of building materials ITE-PIB , Radom 2011.

24. Żółtowski M., Żółtowski B., Castaneda L.: Study of the state Francis Turbine. Polish Maritime Research No. 2/2013, pp 32-38.

25. Żółtowski M.: Investigations of harbour brick structures by using operational modal analysis. Polish Maritime Research No 1/2014, pp 32-38.

CONTACT WITH AUTHOR

Mariusz Żółtowski

University of Science and Technology
Kordeckiego 20 St.
85-950 Bydgoszcz
Poland

e-mail: mariusz.zoltowski@utp.edu.pl

Josef Melcer

Katedra stavebnej mechaniky
Stavebna Fakulta
University of Zilina
Univerzitná 8215/1
010 26 Žilina
Slovakia

e-mail: melcer@fstav.uniza.sk